

THE THREE-DIMENSIONAL CIRCUMSTELLAR ENVIRONMENT OF SN 1987A

BEN E. K. SUGERMAN^{1,2}, ARLIN P. S. CROTTS^{2,3}, WILLIAM E. KUNKEL⁴, STEPHEN R. HEATHCOTE⁵, AND STEPHEN S. LAWRENCE⁶

Draft version November 12, 2018

ABSTRACT

Surrounding SN 1987A is a three-ring nebula attributed to interacting stellar winds, yet no model has successfully reproduced this system. Fortunately, the progenitor’s mass-loss history can be reconstructed using light echoes, in which scattered light from the supernova traces the three-dimensional morphology of its circumstellar dust. In this paper, we construct and analyze the most complete map to date of the progenitor’s circumstellar environment, using ground and space-based imaging from the past 16 years. PSF-matched difference-imaging analyses of data from 1988 through 1997 reveal material between 1 and 28 ly from the SN. Previously-known structures, such as an inner hourglass, Napoleon’s Hat, and a contact discontinuity, are probed in greater spatial detail than before. Previously-unknown features are also discovered, such as a southern counterpart to Napoleon’s Hat. Careful analyses of these echoes allows the reconstruction of the probable circumstellar environment, revealing a richly-structured bipolar nebula. An outer, double-lobed “Peanut,” which is believed to be the contact discontinuity between red supergiant and main sequence winds, is a prolate shell extending 28 ly along the poles and 11 ly near the equator. Napoleon’s Hat, previously believed to be an independent structure, is the waist of this Peanut, which is pinched to a radius of 6 ly. Interior to this is a cylindrical hourglass, 1 ly in radius and 4 ly long, which connects to the Peanut by a thick equatorial disk. The nebulae are inclined 41° south and 8° east of the line of sight, slightly elliptical in cross section, and marginally offset west of the SN. From the hourglass to the large, bipolar lobes, echo fluxes suggest that the gas density drops from 1–3 cm⁻³ to $\gtrsim 0.03$ cm⁻³, while the maximum dust-grain size increases from $\sim 0.2\mu\text{m}$ to $2\mu\text{m}$, and the silicate:carbonaceous dust ratio decreases. The nebulae have a total mass of $\sim 1.7M_{\odot}$. The geometry of the three rings is studied, suggesting the northern and southern rings are located 1.3 and 1.0 ly from the SN, while the equatorial ring is elliptical ($b/a \lesssim 0.98$), and spatially offset in the same direction as the hourglass.

Subject headings: circumstellar matter — dust — scattering — stars: mass loss — supernovae:individual (SN 1987A) — techniques: image processing

1. INTRODUCTION

Supernova (SN) 1987A in the Large Magellanic Cloud (LMC) is the nearest SN in 400 years; the only SN for which the progenitor star has been identified and studied; and the only SN whose evolution is resolved and observed at all wavebands. Located approximately 50 kpc away, this system is just marginally resolved by most ground-based telescopes, even with adaptive optics and high-resolution cameras. Matters are further complicated by bright, neighboring stars, which severely crowd the innermost field of interest for ground- (and even some space-) based imaging and spectroscopy. Nature has a terrible sense of irony in placing the first nearby SN since the inventions of the modern telescope and detector at the far extreme of their observing limits.

The progenitor has been identified as Sk -69° 202 (Sanduleak 1969), a B3 I supergiant (Walborn et al. 1989). From its spectral type and distance, one infers a luminosity of $\sim 10^5 L_{\odot}$, a surface temperature 15000–18000 K, and a radius around 43 R_{\odot} , which imply that the star exploded as a blue supergiant (or BSG; Woosley et al. 1987). This small

radius is confirmed by the underluminous light curve of the SN (Arnett 1987) and the extremely-short time delay between detection of the neutrino burst and optical brightening of the SN (Shigeyama et al. 1987; Arnett 1988).

Sk -69° 202, has a highly-structured circumstellar environment (CSE), evidenced in large part by the famous three-ring nebula (shown in Fig. 1). This material was flash-ionized by the SN light pulse, and is observed today through recombination cooling. The kinematics of the inner, equatorial ring (ER) show it to be a planar ring, expanding at ~ 10.3 km s⁻¹ rather than a limb-brightened ellipsoid (Crotts & Heathcote 1991). Assuming the ER is circular, its observed geometry implies it is inclined at $\sim 43^{\circ}$ (Plait et al. 1995; Burrows et al. 1995), with the northern edge closest to earth. The morphology of the outer rings (ORs) is poorly understood, in part because the south OR (SOR) is distorted from the elliptical shapes of the ER and north OR (NOR).

While SN 1987A exploded as a BSG, the presence of circumstellar material, as well as significant CNO processing within that gas, indicates that the star first passed through a RSG phase (Fransson et al. 1989). To form the three rings, many authors have looked to interacting stellar winds (ISW) between the RSG and BSG outflows. In this model (Kwok 1982; Balick, Preston & Icke 1987), an equatorial overdensity in a previously-expelled slow, dense RSG wind focuses a fast, tenuous BSG wind into a polar trajectory, the interaction from which produces a bipolar peanut-shaped nebula, or wind-blown bubble (Woosley 1988; Woosley, Pinto & Weaver 1988; Arnett et al. 1989; Chevalier & Emmering 1989; Fransson et al. 1989; Luo & McCray 1991b; Wang & Mazzali 1992). Here, the ER

¹ Space Telescope Science Institute, 3700 San Martin Drive, Baltimore, MD 21218; sugerman@stsci.edu

² Department of Astronomy, Columbia University, New York, NY 10027; arlin@astro.columbia.edu

³ Guest Observer, Cerro-Tololo Inter-American Observatory

⁴ Las Campanas Observatory, Carnegie Observatories, Casilla 601, La Serena, Chile; kunkel@ociw.edu

⁵ Southern Observatory for Astronomical Research, Casilla 603, La Serena, Chile; sheathcote@noao.edu

⁶ Department of Physics, Hofstra University, Hempstead, NY 11549; Stephen.Lawrence@hofstra.edu

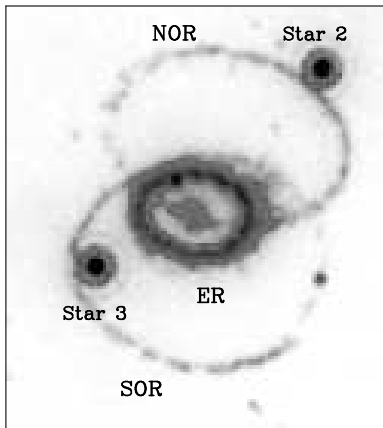


FIG. 1.— *HST* Wide Field and Planetary Camera 2 (WFPC2) negative image of a $4''.5 \times 5''.0$ field surrounding SN 1987A, taken in F656N. North is up, east is left. The ER (central ring) surrounds the ejecta from the SN (center), and is flanked by the north and south ORs (NOR and SOR, respectively). The companion stars 2 and 3, using the classification of Walker & Suntzeff (1990), are positionally coincident along the line of sight. To increase the display range, the ER is displayed with a separate color stretch.

is the overdense waist of the bipolar nebula, and the ORs lie at some point along its outer edges. Such a structure of dust has been traced out by scattered-light echoes as reported in Crotts, Kunkel & Heathcote (1995, hereafter CKH95), supporting this general model.

Blondin & Lundqvist (1993) first modeled the ring nebula within a full 2-D, time-dependent hydrodynamic realization of the ISW model, assuming reasonable values for the mass-loss rates and expansion velocities of the stellar winds in both RSG and BSG stages, as well as an *ad hoc* asymmetry function for the RSG wind. Martin & Arnett (1995) also performed this exercise with a simple cooling law, creating synthetic images from their model (using an assumed opacity and ionizing UV flux) which reproduce the ring geometry only if one identifies the ORs with limb-brightening along peanut-shaped bubbles rather than discrete rings. Rather than rely on *ad-hoc* asymmetry functions, Collins *et al.* (1999) incorporated the wind-compressed disk theory (or WCD, Bjorkman & Cassinelli 1993), in which winds leaving a rapidly rotating star converge at the equator as they orbit the star, to provide the equatorial RSG overdensity. They find good agreement with the ER geometry but require that the star rotate at 30% of the breakup rotation rate. To spin the envelope this quickly, they invoke a binary merger in which a companion spun up the envelope, then joined the primary core (Livio & Soker 1988). None of these models have provided a satisfactory explanation of the ORs, leading some to consider in more detail the influence of a binary companion (Podsiadlowski, Fabian, & Stevens 1991; Lloyd, O’Brien, & Kahn 1995).

These are only a few examples of a much larger body of work, and despite these extensive efforts, many of the critical details of the final evolution of the progenitor and of the CSE surrounding the SN remain speculative. Within the generally-accepted framework of the ISW formation hypothesis lie a large number of variant models, invoking magnetohydrodynamics, binary companions, multiple evolutionary tracks, diverse mass-loss histories and dichotomous final states. Unfortunately, no model has accurately reproduced this system (Sugerman *et al.* 2005).

Thus far, formation models have assumed as sufficient conditions a set of “reasonable” (i.e., typical of nearby LMC supergiants) values for the mass, radius, temperature and composition of Sk $-69^\circ 202$, \dot{M} and v_{exp} for the RSG ($1-2 \times 10^{-5} M_\odot \text{ yr}^{-1}$, $5-20 \text{ km s}^{-1}$) and BSG ($10^{-6}-10^{-7} M_\odot \text{ yr}^{-1}$, $300-600 \text{ km s}^{-1}$) winds, and have used as the primary constraints the few physical conditions of the ER of which we are certain: the radius ($0''.81$; Burrows *et al.* 1995), and the expansion velocity (10.3 km s^{-1} ; Crotts & Heathcote 1991). Results matching only a handful of observed conditions can only be regarded as suggestive and preliminary. However, up to this point, only a handful of constraints exist. Our understanding of the circumstellar history of SN 1987A is limited by a lack of observed constraints, not theoretical models.

The SN provides us with two independent, yet equally useful means to reconstruct the mass-loss history. First, we are now observing a unique period in the formation of SNR 1987A as the high-velocity SN debris overtakes the slowly expanding ER (Sonneborn *et al.* 1998b; Sugerman *et al.* 2002). While this interaction will eventually destroy the circumstellar nebula, it provides the opportunity to explore the CSE by detailing the material directly through shock-heating. Furthermore, the increasing X-ray and UV flux from this interaction will reionize unseen portions of the nebular structure, revealing many of them for the first time (Luo, McCray, & Slavin 1994).

Second, light echoes from the SN have illuminated a significant volume of the CSE, and can be used to constrain the three-dimensional (3-D) structure, density, and composition of the stellar outflows. Three general structures have been previously reported.

Close circumstellar material: The inner few light years surrounding SN 1987A have been studied between days 750–1469 (after the SN; 1987 Feb. 24.23) by CKH95. Echoes detected within $3''$ of the SN were mostly found to lie on an hourglass-shaped bipolar nebula, inclined $43^\circ \pm 5^\circ$ south, and rotated $3^\circ \pm 5^\circ$ east of the line of sight, while a smaller set were also identified as roughly coplanar with the ER but at larger radii.

Napoleon’s Hat: Napoleon’s Hat (NH) was originally identified by Wampler *et al.* (1990a) as an arc-like feature (also described as an archer’s bow by Crotts & Kunkel 1991) looping roughly $6''$ north of the SN. It has been variously interpreted as a disk coplanar to the ER (Wang & Wampler 1992), a truncated double cone (Podsiadlowski, Fabian, & Stevens 1991), or a parabolic bow shock at the terminal edge of a region evacuated by the main-sequence (MS) progenitor (Wang, Dyson, & Kahn 1993).

Large radius contact discontinuity: Recognizing that red giants and supergiants typically have slow, dense stellar winds, Chevalier & Emmering (1989) proposed that the interface between the RSG wind and surrounding medium (homogenized and rarified by a prolonged MS wind) would be a “snowplow” discontinuity (Castor, McCray, & Weaver 1975). As these are dense and cold, the interface should be both long-lived and have a significant dust component. Chevalier & Emmering (1989) predicted that a stellar-wind bubble in pressure equilibrium with the surrounding medium should occur at a radius of roughly 16 ly for reasonable RSG wind parameters. This corresponds closely to echoes reported by Bond *et al.* (1989,1990), Couch & Malin (1989), and Crotts & Kunkel (1989,1991) roughly $9''$ from the SN, which are interpreted as the contact discontinuity (CD) be-

tween the RSG/MS winds.

Until now, most modeling efforts have focused on the last $\sim 20,000$ years of evolution (roughly the kinematic timescale of the rings and evolutionary timescale of the BSG stage) while, in large part, avoiding the previous 0.3–1 Myr of the RSG phase, during which the NH and CD features formed. Observations of the full circumstellar environment provide a unique opportunity to detail the products of the progenitor’s mass-loss. A more complete set of boundary conditions is necessary to properly investigate the SN system, and to distinguish viable models from unrealistic scenarios.

Using the technique of PSF-matched difference imaging on 16 years of optical imaging data, we report an observational effort, at the highest sensitivity and resolution to date, to understand more fully the entire circumstellar environment (CSE) of SN 1987A, and to recreate a more thorough history of the progenitor’s mass-loss. This paper describes the detection and analysis of light echoes within $30''$ of the SN as observed in ground-based and *HST* imaging. This work is also summarized in Sugerman et al. (2005), followed by a detailed analysis of how our results constrain formation models and the progenitor’s evolution.

The theory and application of light echoes are presented in §2, including a dust-scattering model which is used to constrain the density and composition of echoing material. The data are described in §3, followed by the data-reduction pipeline (§4). The light echoes, their three-dimensional positions, and the tools necessary to analyze them, are presented in §5. These data are used to build geometric models of material within ~ 30 ly of the SN, the details of which are explained in §6–8. A complete picture of the CSE, including constraints on the density, chemical composition, and mass of all circumstellar material, is made in §9. It is our hope that the results presented here will serve as a significantly-improved set of constraints for hydrodynamic models of the CSE formation, for stellar-evolution models of the progenitor, and for addressing the general question of asymmetric and bipolar stellar outflows.

2. LIGHT ECHOES: THEORY AND MODEL

When a light pulse is scattered by dust into the line of sight, an observable echo is produced, provided the pulse is sufficiently luminous and the dust sufficiently dense. An echo observed a given time after the pulse must lie on the locus of points equidistant in total light travel from the source and observer, that is, an ellipsoid with known foci. This simple geometry, shown in Figure 2, directly yields the three-dimensional (3-D) position of an echo, uncertain only by the assumed distance to the source. A complete discussion of light echoes, including single-scattering models and the observability of echoes around a wide variety of cataclysmic and other variable stars, can be found in Sugerman (2003). For completeness, we briefly summarize the salient points below.

2.1. Light Echo Surface Brightness

Consider the geometry shown in Figure 2, in which a source at distance D from the observer emits a pulse of light of duration τ . This light scatters off dust located at position r from the source, and reaches the observer a time t after the arrival of the unscattered light pulse. Since D is generally much greater than r , the echo depth z along the line-of-sight can be approximated by the parabola (Couderc 1939)

$$z = \frac{\rho^2}{2ct} - \frac{ct}{2} \quad (1)$$

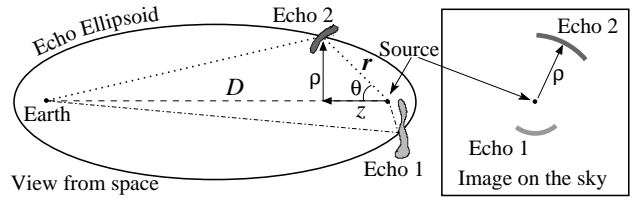


FIG. 2.— Cartoon schematic of a scattered-light echo. Echoes lie on the locus of points equidistant in light travel from the source and observer—i.e., an ellipsoid—and appear as arcs or rings on the plane of the sky, with a one-to-one mapping between their 2-D image positions (right) and their 3-D locations in space (left). Note that the distances are not to scale: D is much larger than z , such that the segments from Earth to the scattering dust are nearly parallel to the line of sight.

where $\rho = r \sin \theta$ is the distance of the echo from the line-of-sight in the plane of the sky, and θ is the scattering angle (provided $D \gg r$).

Treating the dust as a thin planar sheet of thickness Δz , and adopting cylindrical coordinates, the surface brightness of an echo at a given wavelength λ is given by

$$B_{SC}(\lambda, t) = F(\lambda) n_H(r) \frac{c \Delta z}{4\pi r \rho \Delta \rho} S(\lambda, \mu). \quad (2)$$

To facilitate computations, we adopt units of years and light-years, making $c = 1$. We define the integrated scattering function

$$S(\lambda, \mu) = \int Q_{SC}(\lambda, a) \sigma_g \Phi(\mu, \lambda, a) f(a) da \quad (3)$$

where a is the dust-grain radius, $\sigma_g = \pi a^2$ is the physical cross section of a grain, and Q_{SC} is a grain’s scattering efficiency. The number density of grains at position r with radii between $(a, a + da)$ is given by

$$n_d(r, a) da = n_H(r) f(a) da \quad (4)$$

where n_H is the number density of H nuclei, and $f(a)$ is the grain-size distribution function. The total flux from the light pulse incident on the dust is $F(\lambda) = \int F(\lambda, t') dt'$. We adopt the Henyey & Greenstein (1941) phase function Φ . Since the light pulse and dust have finite widths, the observed radial size $\Delta \rho$ of the echo yields an estimate of its line-of-sight depth

$$\Delta z = \frac{\rho}{t} \sqrt{\Delta \rho^2 - \left(\frac{\rho}{2t} + \frac{t}{2\rho} \right)^2} \tau^2. \quad (5)$$

Both the observed flux $F(\lambda)$ and area element $\rho \Delta \rho$ diminish as D^{-2} , thus equation (2) for surface brightness is distance independent, as expected. If the echo and source are close, they should suffer roughly the same extinction. This work is restricted to single-scattering events, and the reader is referred to Chevalier (1986) for a discussion of multiple-scatterings, which are only of significance when the optical depth of the scattering material $\gtrsim 0.3$.

2.2. Dust Properties

Mathis, Rumpl, & Nordsieck (1977) found that a mixture of carbonaceous and silicate grains following a density distribution given by $f(a) \propto a^{-3.5}$ adequately modeled Galactic starlight extinction. Weingartner & Draine (2001, hereafter WD01) and Li & Draine (2001) have calculated dust scattering and absorption properties for graphite and “astronomical silicate,”⁷ from which WD01 have constructed a new density

⁷ Tabulated values of dust properties are available at [http://www.astro.princeton.edu/~sim\\$draine/dust/dust.diel.htm](http://www.astro.princeton.edu/~sim$draine/dust/dust.diel.htm)

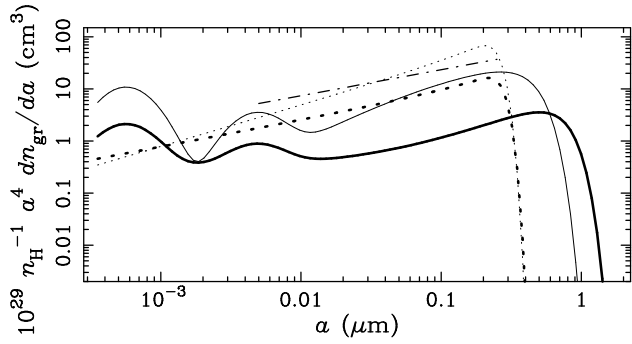


FIG. 3.— Dust grain density distributions for carbonaceous (solid lines) and silicate (dotted lines) dust from WD01. Thick lines are for the LMC model with $R_V = 2.6$, $b_C = 1 \times 10^{-5}$, and thin lines are for the Galactic model with $R_V = 3.1$, $b_C = 6 \times 10^{-5}$. For clarity, and to allow the reader to estimate the mass present in each size range, data are plotted in units of $a^4 dn_{gr}/da$. The dot-dashed line shows the corresponding density distribution from Mathis et al. (1977).

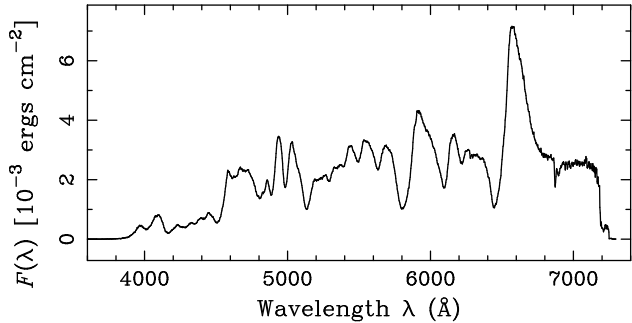


FIG. 4.— Time-integrated spectrum of SN 1987A from 59 days before to 42 days after maximum light.

distribution $f(a)$ to fit observed interstellar extinction. We refer the reader to their paper for the actual functional form. We adopt their LMC dust model for $R_V = 2.6$, and $b_C = 1 \times 10^{-5}$, which is shown by thick curves in Figure 3. For comparison, their preferred Galactic dust model (case A, $R_V = 3.1$, $b_C = 6 \times 10^{-5}$) is also shown. The reddening ratio is defined as $R_V = A_V/E(B-V)$ (Cardelli, Clayton & Mathis 1989), and b_C is the total C abundance per H nucleus.

2.3. The Light Pulse from SN 1987A

Using the early optical light curves from Hamuy et al. (1988), SN 1987A reached maximum light in V and R roughly 87 days after its discovery on 1987 Feb 24. The light-curve duration τ is measured as the effective width $\tau = \int F(\lambda, t) dt / F(\lambda, t_{\max})$. A homogenous time series of spectra from the first thousand days are publically available from the SUSPECT supernova archive⁸. We integrated these spectra over the first 420 days, and found an effective width of 100 days in the wavelength ranges of interest. Integrating again over just this width, centered at maximum light, we generated the time-integrated flux $F(\lambda)$ that will enter equation (2), shown in Figure 4. Note that at these early times, spectral coverage ended at 7300Å, and there is no empirical spectrum available in the wavelength range of our redder filter (§3.2).

Referring again to Figure 2, since $D \gg r$, the trajectory from source to dust to earth is very similar to the direct source-earth path. Under the assumptions that the ISM is homoge-

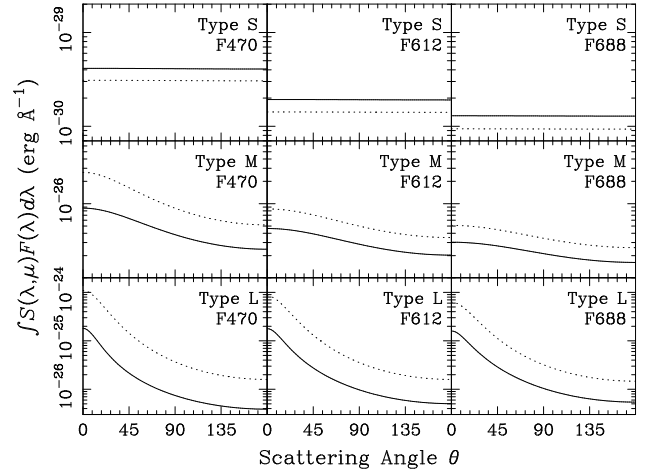


FIG. 5.— The average integrated scattering function $S(\lambda, \mu)$, integrated over the total spectrum $F(\lambda)$ of SN 1987A (Fig. 4) and filter profiles (Fig. 7). Line style designates composition: solid lines show carbonaceous dust, and dotted lines show silicates. Columns are calculated for a given filter, and rows are calculated for LMC dust with grain-size range types L, M, and S, as noted at upper right in each panel. This integral gives the energy scattered toward the observer in unit time by a unit volume of gas with unit density located unit distance from the source.

nous near the SN, and that extinction is small within the echoing dust (implicit in the single-scattering approximation), flux from the SN and surrounding light echoes should be reddened by the same amount along the optical path between the LMC to the observer. This assumption allows the direct comparison of the observed echo fluxes to the dust-scattering model, without the additional uncertainty of extinction corrections (§4.6). The spectrum in Figure 4 is therefore not extinction-corrected⁹.

2.4. The Light Echo Model

To calculate the total echo surface brightness received in a given bandpass, equation (2) must be integrated in wavelength over the filter response function $T(\lambda)$. The integrated scattering function $S(\lambda, \mu)$ must also be integrated over grain sizes, using equation (3) and the dust-density models from WD01. Removing the geometric factors and gas density from equation (2), we model echo surface brightness by computing

$$I = \iint T(\lambda) F(\lambda) Q_{sc}(\lambda, a) \sigma_g \Phi(\mu, \lambda, a) f(a) da d\lambda. \quad (6)$$

which is integrated numerically using Simpson’s Rule (Press et al. 1992). This gives the energy scattered toward the observer in unit time for unit volume of gas with unit density at unit distance from the source, and therefore it need only be scaled to the appropriate physical values to yield the predicted surface brightness.

Figure 5 shows this integral for the three filters F470, F612 and F688 (Fig. 7). Results are given separately for carbonaceous and silicate dust. Since the range of dust-grain sizes in the CSE are unknown, we integrate over three size intervals, denoted “S” (small, $a = 3.5 \times 10^{-4} - 0.01 \mu\text{m}$), “M” (medium, $a = 3.5 \times 10^{-4} - 0.1 \mu\text{m}$), and “L” (large, $a = 3.5 \times 10^{-4} - 2.0 \mu\text{m}$). The type-L dust includes the full range of grain sizes in $f(a)$ from Weingartner & Draine (2001).

⁹ Spectra of SN 1987A in the SUSPECT archive were dereddened assuming $E(B-V) = 0.16$ and $R_V = 3.1$, which we have removed to reproduce the observed values.

⁸ [http://bruford.nhn.ou.edu/\\$\sim\\$sim\\$suspect/index.html](http://bruford.nhn.ou.edu/\simsim$suspect/index.html)

Scattering for grains with $a < 0.1\lambda/2\pi$ occurs within the Rayleigh limit, for which $S \propto \lambda^{-4}$. These small grains have a small scattering efficiency and scatter isotropically, while distributions including large grains predominantly forward scatter. It should be noted that while $S \propto \lambda^{-4}$ for Rayleigh scattering, the largest color shift possible for the integrated SN spectrum (Fig. 4) in our continuum filters is $S \propto \lambda^{-3}$, as can be easily calculated from the type-S dust in Figure 5.

To apply this scattering model, colors of echoes are compared to the model values in Figure 5 to constrain the grain-size distribution, and the relative populations of carbonaceous and silicate grains. Dust (or gas) density is calculated from the scaling between the model and observed surface brightness, using the geometric factors ρ and $\Delta\rho$, measured from the data, with $\tau=100$ days, as determined above.

Distinguishing between type S and L dust can be accomplished a few ways. First, as noted above, small grains scatter less flux than larger ones, thereby requiring a higher gas density for a given observed surface brightness. Since greater density dust has stronger extinction, practical constraints exist for upper limits to gas density. If a single structure is probed at many scattering angles, and one assumes the density of that structure is constant, the variation of surface brightness with θ can also constrain the grain sizes. Dust composition can be constrained by comparing colors of observed and modeled echoes, although carbonaceous and silicate dust have nearly identical scattering properties at these optical wavelengths. A better probe of chemical composition are UV echoes, since carbon and silicate dust grains have strongly-differing features at $\lambda < 2500\text{\AA}$ (Sugerman 2003).

As a final note, in treating echoes with a planar approximation, this scattering model assumes that the observed echo is well represented by a slab of dust of thickness Δz , all of which is scattering the integrated flux $F(\lambda)$ toward the observer. In reality, the echo is the integral of many volume elements of gas, each of which scatters a particular time-dependent flux from the SN lightcurve (see §2.1 of Sugerman 2003). For echo observations in which a resolution element is much smaller than the outburst duration $c\tau$ (such as those from V838 Mon Bond et al. 2003), a much more detailed scattering model can deconvolve the spatially-resolved dust properties using the time-dependent lightcurve. However, such treatment is unsuited to circumstellar echoes from SN 1987A, since the image resolution is larger than 100 light days.

3. DATA

3.1. Observations

SN 1987A has been observed many times per year since day 375 (after core collapse) in a ground-based campaign to monitor the appearance and evolution of its light pulse as it illuminates circumstellar and interstellar material. Some data from this campaign have previously been reported by Crofts, Kunkel & McCarthy (1989); Crofts & Heathcote (1991); Crofts & Kunkel (1991); and Crofts et al. (1995) in studying the circumstellar environment, and in Xu, Crofts & Kunkel (1994, 1995) and Xu & Crofts (1999) for interstellar echoes.

For the present application, we require data with high signal-to-noise, good seeing (arcsecond or better), and sufficient resolution to resolve most crowded stars and detail in the narrow surface brightness features. Those epochs of imaging that match these criteria are listed in Table 1. Data were primarily taken on the 2.5-m (100-inch) Dupont telescope at

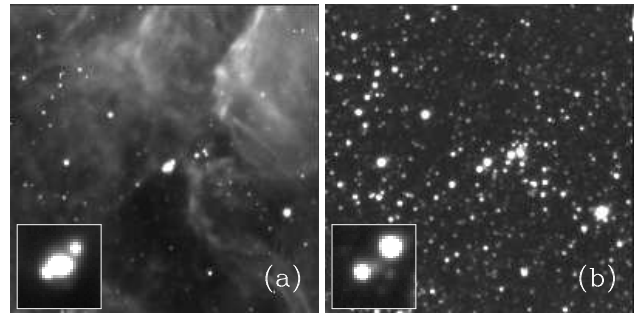


FIG. 6.— Ground-based images of SN 1987A from day 1998. Each image is $130''$ on a side, in a standard orientation with north up, east left. The inset at bottom left is $10''$ on a side. (a) Narrow-band $H\alpha$ image. The inset shows the extended nebula surrounding the SN, as well as stars 2 and 3. (b) F612 continuum-only image of the same field as (a).

the Las Campanas Observatory (LCO) at platescales of $0''.163$ and $0''.260 \text{ pix}^{-1}$, but one epoch from the Cerro Tololo Inter-American Observatory (CTIO) 4-m telescope is also used.

Since its launch in 1990, *HST* has been used at least yearly to observe the SN, largely through the efforts of the Supernova Intensive Survey (SInS) collaboration. We used archival Wide Field and Planetary Camera 2 (WFPC2) data taken between 1994 and 2001 for the current application. Those epochs in which echoes were discovered are also listed in Table 1.

3.2. Photometric Bands

SN 1987A is located in a region of the LMC with considerable nebular structure, as shown in an $H\alpha$ image from day 1998 in Figure 6a. Furthermore, the three-ring nebula surrounding the SN is the strongest source of line emission in this region. These extended surface brightness features create significant sources of noise when searching for light echoes, especially in the inner few arcsec around the SN, since the flux from three-ring nebula changes with time. To minimize the contribution of nebular-line contamination, four specially-selected continuum bands were selected for the monitoring campaign, centered at 4700, 6120, 6880, and 8090 \AA . The laboratory transmission curves are plotted in Figure 7. These bandpasses were chosen to avoid the brighter emission lines of the diffuse LMC clouds (e.g., $H\alpha$, [N II], [O III], and [S II]), as well as strong emission lines from the SN ejecta. This has the added benefit of suppressing flux from the central SN at early times by 1–1.5 mags (Crofts et al. 1995).

In keeping with the *HST* filter naming convention, we will refer to each continuum filter by its central wavelength in nm, preceded by an “F”, such that the 6120 \AA filter is F612. Note however that these differ from *HST* filter names since the latter are appended with the width of the filter (i.e. F656N). The effectiveness of these filters at suppressing nebular-line emission is shown in Figure 6b, the F612 image from the same epoch as panel (a). There is no detectable signal from the large cirrus-like clouds or the inner circumstellar nebula. An echo results from the SN light pulse scattering off dust, and since its spectrum had a bright continuum over the duration of its outburst (Fig. 4), these filters will not suppress echo signal.

4. DATA REDUCTION

Data were reduced in the following stages: (1) CCD processing, (2) homogenization, (3) pipeline pre-processing, and (4) PSF-matched difference imaging. Each stage is designed to be minimally-invasive, thereby maximally preserving faint

TABLE 1
 LIGHT ECHO OBSERVATIONS

Epoch	Day	Telescope	Platescale	Filters
1988 Dec 14	659	LCO-100	0''163	B,V,R,I,Z
1989 Mar 15	750	LCO-100	0''163	6023,6067,6967
1989 Dec 18	1028	LCO-100	0''163	F470,F612,F688,F809
1990 Feb 14	1086	LCO-100	0''163	F470,F612,F688,F809
1991 Mar 4	1469	CTIO-4	0''124	F688
1992 Jan 15	1787	LCO-100	0''260	F612,F688,F809
1992 Mar 20	1851	LCO-100	0''163	F612
1992 Aug 14	1998	LCO-100	0''260	F612,F688
1992 Nov 19	2095	LCO-100	0''260	F612,F809
1993 Nov 22	2462	LCO-100	0''260	F470,F612,F688,F809
1993 Dec 27	2498	LCO-100	0''260	F470,F612,F688,F809
1994 Jan 6	2508	LCO-100	0''260	F470,F612,F688,F809
1994 Apr 1	2593	LCO-100	0''260	F612
1994 Sep 24	2769	HST/WFPC2	0''045	F555W,F675W,F814W
1994 Nov 25	2830	LCO-100	0''260	F612,F688,F809
1995 Jan 7	2874	LCO-100	0''260	F612,F688,F809
1995 Mar 5	2932	HST/WFPC2	0''045	F555W,F675W,F814W
1995 Mar 10	2935	LCO-100	0''260	F612,F688,F809
1996 Jan 12	3245	LCO-100	0''260	F612,F688,F809
1996 Feb 06	3270	HST/WFPC2	0''045	F555W,F675W,F814W
1997 Jul 10	3789	HST/WFPC2	0''045	F555W,F675W,F814W

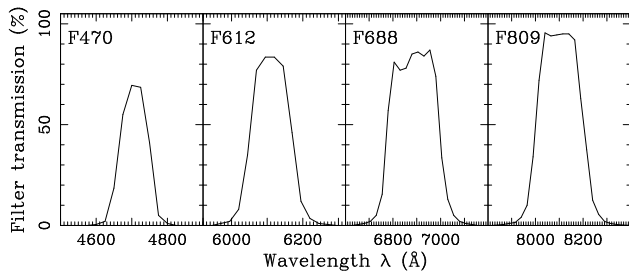


FIG. 7.— Filter transmission curves for the narrow-band continuum filters used to observe SN 1987A.

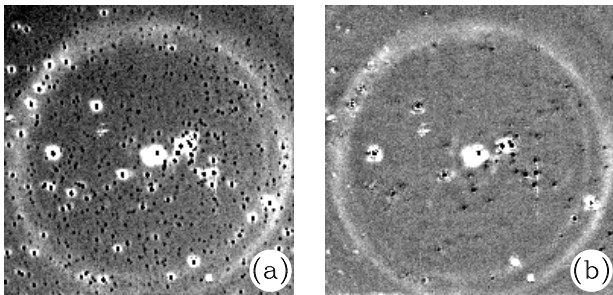


FIG. 8.— Differences of two photometrically scaled images, showing (a) the direct subtraction, and (b) the PSF-matched subtraction.

structure and flux. We begin with a discussion of difference-imaging, followed by the four reduction stages listed above.

4.1. Difference-Imaging Photometry

Consider the problem of subtracting two photometrically-scaled images to study time variable phenomena. Figure 8a shows a typical direct arithmetic subtraction. Even under identical circumstances (same telescope, detector, airmass, etc.) the point-spread function (PSF) across the detector can change, caused by e.g. flexure of the mirrors, movement of the filter, or change in atmospheric seeing. As a result, residuals remain around every star in the field, leaving holes and haloes

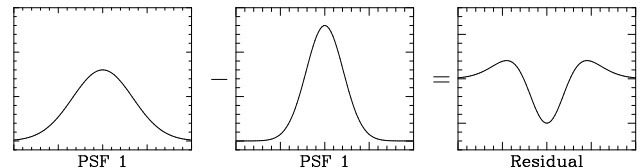


FIG. 9.— Two different PSFs of identical area are subtracted, yielding the residual in the right-hand panel.

such as those seen here.

This is easily understood by subtracting two Gaussians of differing peak and FWHM, but identical total area, as shown in Figure 9. The residual has a bright halo in the wings and a hole in the center, since an uneven amount of flux was subtracted from each point along the profile. This can be addressed a few ways. Each image can be degraded, by smoothing with e.g., gaussian filters. This is an invasive procedure, smearing out structure and detail that might otherwise be studied. Rather, an optimal technique is to remap the flux in one PSF to that of the other in a uniform and consistent way.

Our technique is to seek a convolution kernel k such that the input star i can be mapped onto the reference star r , or $i = r * k$. From the Convolution Theorem, the Fourier Transform (FT) of this mapping becomes

$$\text{FT}(i) = \text{FT}(r) \times \text{FT}(k) \quad (7)$$

from which we isolate the convolution kernel

$$k = \text{FT}^{-1} \left[\frac{\text{FT}(i)}{\text{FT}(r)} \right]. \quad (8)$$

Tomaney & Crotts (1996) implemented this method of PSF-matching in an external IRAF¹⁰ package *difimphot* (Difference IMaging PHOTometry), originally designed for use with the M31 microlensing project (Crotts 1992), and subsequently updated for the MACHO microlensing project (e.g.

¹⁰ IRAF is distributed by the National Optical Astronomy Observatories, which are operated by the Association of Universities for Research in Astronomy, Inc., under cooperative agreement with the National Science Foundation.

Alcock et al. 1995). In its simplest implementation, empirical or model PSFs are used with equation 8 to build the kernel, which is then convolved with the input image, and the reference image is subtracted away. We have implemented further modifications to employ the robust PSF-fitting and building algorithms of *daophot* (Stetson 1987), as described in Appendix A. See Alard (2000) for an example of alternative methods of PSF-matching.

The same data entering the arithmetic subtraction in Figure 8a are shown after PSF-matching in panel (b). Nearly all stars have been cleanly subtracted. Since Poisson noise σ scales as the square-root of signal, the data are slightly noisier at the positions of subtracted stars than in the surrounding sky. Nonetheless, this represents an improvement in the background noise by a factor of ~ 2 for faint stars, and $\gtrsim 5$ for those of median brightness. The brightest stars with linear profiles are well-subtracted except in the cores, where Poisson noise is highest. We can reliably detect extended surface brightness only $1 - 2\sigma$ above the background sky, while for noisier regions (near bright stars or other variable sources) this threshold must be evaluated on an individual bases.

PSF-matching can not completely subtract away stars with non-linear or saturated profiles for many reasons. (1) These stars do not have a uniform profile that can be described by a single function. (2) The PSF of such a star does not properly represent how flux is recorded on the chip. (3) Since these are the brightest objects in the field, even if the average profile is well-subtracted, the residuals will be largest. Thus these represent untreatable sources of error even in the best of subtractions.

4.2. CCD Processing

Ground-based data were reduced within *IRAF* in the standard manner. Images were column biased, checked for residual bias and, if appropriate, a full bias frame was subtracted. Images were then flat-fielded. Bad columns, rows or pixels were *not* cosmetically fixed; however, most images had bad data within 1–4 pixels of each edge, which were reset to zero value. Pipeline-calibrated WFPC2 images were used directly from the data archive.

4.3. Homogenization

For a given epoch, all data in a single filter must be combined into a single “stack” image. To perform difference-imaging, this data must also be geometrically-registered to a common reference frame. This latter step is critical since registration errors lead to large stellar subtraction residuals, a significant source of noise and error. We chose to register all ground-based data to the $0''.163 \text{ pix}^{-1}$ platescale, for the following reasons. The primary interest of this work is to detect and resolve faint structure, thus data need to be of high-resolution. Faint structures become brighter when resampled onto a lower-resolution grid, but the ability to resolve these from the background (stars, subtraction residuals, cosmetic defects, statistical pixel noise) is diminished with the width of such features. Resampling high resolution data onto a lower-resolution grid also degrades the FWHM of stellar profiles, and PSF-matching works best with a well-sampled $\text{FWHM} \gg 2$ pixels.

Since the images taken at $0''.260 \text{ pix}^{-1}$ have high signal-to-noise and the stellar PSFs are well-sampled, the data can be interpolated onto a higher-resolution grid without great loss of information in faint features. This has been rigorously tested and discussed by Fruchter & Hook (2002) within the context

of “drizzling” data to higher resolution. Individual frames were all registered to a common orientation, then stacked. Since most frames are slightly offset from each other over a single epoch, this is effectively the same procedure as drizzling observations with sub-pixel shifts.

4.3.1. Geometric Registration

One epoch at $0''.163 \text{ pix}^{-1}$ was chosen, and the F612 image was geometrically-registered to orient the (x, y) axes with north and west, using an astrometric solution derived from stars in the UCAC-1 and 2 catalogs (Zacharias et al. 2000, 2004), which we determine to be accurate to within $0''.03$ of the Hipparcos astrometric reference frame in this region of the sky. This is the absolute reference orientation. All other filters within that epoch were registered to this orientation, then all other epochs were registered to the corresponding filter in the reference orientation. For those epochs with non-standard filters, the nearest equivalent was used.

Registration transformations for ground-based frames were computed for a third-order polynomial with half-cross terms, and resampling was accomplished using a bicubic interpolated spline. Since centroids are the dominant source of error in these transformations, we employ the techniques of crowded-field PSF-fitting, for which extensive software exists in the *daophot* package (Stetson 1987). An empirical PSF is built using actual stellar profiles from the frame, as outlined in the *daophot* package. This PSF is then iteratively fit to groups of stars using a non-linear least-squares minimization, and centroids are output to a file. Avoiding stars with saturated or non-linear profiles, we find PSF-fitting has an average centroid uncertainty of less than 1% of the FWHM. Matched pairs of stars in both input and reference images were made using *starmatch*, a highly efficient implementation of the triangle-matching algorithm of Groth (1986). In 98% of the frames, geometric registration was accomplished with RMS errors less than 0.1 pixel in both dimensions.

4.3.2. Image Stacking

All registered images in a given filter per epoch are combined into a single “stack.” This begins with determining a list of reference stars, which are uncrowded, have a clean spatial profiles, high signal-to-noise, and constant flux. These lists are used to build empirical PSFs, and determine the photometric scalings between images for combining and differencing.

As a general algorithm, reference stars are identified from a group of images. Bright and unsaturated stars are selected by applying flux cut-offs to the stellar identification algorithm *daofind*, while crowding and clean profiles are addressed by the *daophot* software (e.g. *pstsel*), and custom software in the *difimphot* package. Aperture and PSF-fitted photometry is performed on this star list for all images in the group. The photometry provides an initial guess of the photometric scaling between images, which is applied to the flux of each star per image. Stars that vary by more than a user-specified amount are rejected, and the procedure is repeated. Stars that vary within 3% of their median value are treated as constant, and constitute the reference-star list.

PSF-fitted photometry is performed on each image in the stack using the reference star list. This photometry is used to determine an additive (sky) and multiplicative (scale) scaling to remove the median sky and photometrically normalize each image to the best-seeing, highest signal-to-noise image

in the stack. Data with unusually-poor seeing or large photometric scalings can be rejected, and the remaining images are combined using a weighted average, where each image is weighted by

$$w = \frac{1}{\text{scale}^2 \cdot \text{sky} \cdot \text{FWHM}^2}, \quad (9)$$

renormalized such that $\sum w_i = 1$. Bad pixels, from cosmic rays, warm or dead pixels, cosmetic defects, or large statistical outliers, can be rejected using sigma-clipping if there are $\gtrsim 10$ images in the stack, otherwise we use the median. We found through trial-and-error that when sigma-clipping rejection could not be used, rejecting the highest and lowest pixel value for a given position in the data was sufficient to remove most bad pixels.

4.3.3. The Homogenized Data

The result of the above is a homogenous set of registered images, one per filter per epoch, which maximized the signal-to-noise while minimally-resampling the data. This last point is important, since each spatial resampling degrades the image quality, thereby smearing out faint echo signal, making them more difficult to detect.

Finally, note in Figure 6 that Stars 2 and 3 are crowded with the SN and the immediately-surrounding nebula. Star 3 is known to be variable, and will leave subtraction residuals in many difference images, depending on its flux at the time of observation. Since the SN is fading with time, it too will produce confusing residuals at early times, when it was still bright in the continuum. We therefore PSF-subtract the SN and Stars 2 & 3 using *daophot*. This was performed two ways. First, we allowed the subtraction algorithm (*allstar*) to locate its own centroids for the three sources. Second, we generated a geometric transformation between the ground-based frame and the WFPC2 F656N (H α and [N II]) field, in which the centroids of these three sources can be measured to within 5 mas, and fixed the centroids to these transformed values.

WFPC2 data were registered and stacked as described in Sugerman *et al.* (2002). Tiny Tim model PSFs were used to subtract Stars 2 and 3, as well as all other bright stars with detectable diffraction spikes. Note that in this and the following, ground-based and WFPC2 data are never intercompared.

4.4. Pipeline Preprocessing

As explained in §A, pre-processing requires the selection of reference stars, building of PSFs, and creation of reference images. For both the ground-based and WFPC2 images, reference-star lists were constructed from those stars that are present and photometrically constant in each dataset. High signal-to-noise and clean PSFs were built using these lists as outlined in §A.2. In the current application of difference-imaging, we are searching for extended surface-brightness features that vary in time. As such, we require a reference image (§A.1) that is free of all echo signal. Since echoes are present in each epoch in the ground-based imaging, an iterative procedure must be adopted to generate such a frame, as described below.

All stacked images in a given filter were median-combined into a temporary reference stack, using zero-point offsets (for the sky) and photometric scalings derived from photometry of the reference-star list. Each stacked image was then PSF-matched to and differenced (§A.3) by this temporary reference stack. For a given epoch, the difference images from

all filters were co-added into a single echo image. If a faint structure is truly an echo, it will appear as positive signal in all continuum filters, while background noise is a random distribution about a fixed value. Artifacts, such as flat-fielding errors or ghosts, can either vary or remain constant between different filters, and therefore can present themselves as false signals in these images.

Light echo candidates in each echo image were identified using a custom-written implementation of the friends-of-friends algorithm. The median and standard deviation are computed within a moving box of $m \times m$ pixels, and any pixel whose value is more than $N\sigma$ above the median is flagged as a “friend.” Subsequently, every pixel touching that friend that is more than $n\sigma$ above the median is a friend of the friend. Every friend-of-a-friend is found in the image, with different groups merging when they touch. From a practical standpoint, this works best on block-medianed images, in which each pixel in a 4×4 moving box is replaced by the median value in that box. This smooths out a great deal of statistical shot noise, making echoes easier to detect above the background. In general, we found that $N = 3$ and $n = 2$ were sufficient.

Friend-lists surrounding bright stars or more than $30''$ from the SN were rejected. The remaining groups were checked against those from the two adjacent epochs to ensure the signals are real. It is highly unlikely that a bright echo will appear in only one epoch, and not a few months prior or later, since such a structure would have to be extremely thin on the plane of the sky and along the line of sight, as well as being fortuitously placed to be illuminated at that particular epoch. Additionally, groups were checked to ensure they did not result from ghosts from nearby bright stars; as there are many such stars near the SN, many such ghosts were found. Those lists that survived all cuts were turned into pixel masks for each image in that epoch.

In some cases, consistent structures appeared as positive flux in early difference images and negative flux later, or vice versa, indicating that an echo was present in the reference image. In such cases, stacks were differenced from other individual stacks well separated in time, and friend lists were generated from these difference images.

All stacks in a given filter were then again median-combined, this time with the echo pixels in each image masked out. The above steps were repeated with these new reference images, and very few additional echoes remained. The third iteration generated reference stacks which did not produce any detectable echo residuals. We adopt these as our reference, echo-free images. The same technique was used for both the ground-based and WFPC2 images; however, in the latter case, echoes disappeared from the PC chip by 1997, after which considerable data exist. Thus generation of the WFPC2 echo-free images was much more straightforward.

4.5. PSF-Matched Difference Imaging

PSF-matching and difference imaging proceeded as explained in §A.3. For the ground-based data, difference images were made between each epoch in each continuum filter and the corresponding reference image, for all three kinds of stacks: those in which no PSF stars were subtracted, those in which the SN and Stars 2–3 were subtracted with floating centroids, and those in which the centroids were fixed by their astrometry.

In many cases, no matter how the PSF was created, it left circular residuals around star 2, and to a lesser degree around star 3. The cause is straightforward: the empirical PSF is

scaled to match the flux of star 2, as are its wings. Since the wings of any empirical PSF are noisy (due to the low signal-to-noise of the data that comprise them), this noise becomes significant when scaled to the flux of a bright or non-linear star, such as star 2. One may either replace the wings *a posteriori* by, e.g., an elliptical gaussian (as we do in PSF-matching) or attempt to minimize this effect by carefully constructing the PSF. The former option is not built-in to *daophot*, and rather than write a revised version of this software, we opted for the latter.

In subsequent discussions of structures found within $3''$ of the SN, a ground-based result is not deemed significant unless it appears in both PSF-subtracted difference images. Furthermore, a result that lies within a noisy PSF-subtraction residual is not significant if we cannot demonstrate that the structure is real and not an artifact of the noisy wings. This is easy to test by examining the non-PSF-subtracted difference image, or by PSF-subtracting other bright stars and examining their residuals.

For WFPC2 imaging, the *Tiny Tim* model PSFs have no noise in the wings, thus there is no need to consider alternate PSF-subtractions. All epochs of data were differenced from the corresponding reference image in the three filters of interest, F555W, F675W and F814W.

4.6. Photometric Calibration

To study the density and composition of the dust producing the observed light echoes (§2.1), it is necessary to photometrically calibrate the continuum filters. Since fluxes determined from broad-band Johnson filters may be a poor fit to our narrow continuum bands, we instead determine the calibration spectroscopically, as follows.

Space Telescope Imaging Spectrograph (STIS) spectra in G430L and G750L (blue and red) were taken through the $2''$ -wide slit in 2000 November as part of a Director's Discretionary *HST* allocation to study hot spot evolution (Sugerman et al. 2002). This pointing included stars 4, 7, 34 and 35 from Walker & Suntzeff (1990), respectively $5''.5$, $9''.7$, $17''.0$, and $16''.0$ from the SN. Each star is reasonably un-crowded on our ground-based frames, allowing for accurate PSF-fitted photometry with *daophot*. All four are close to the SN on the sky, and assuming they are similarly located within the LMC, all five sources should suffer roughly the same extinction.

Pipeline-calibrated spectral images were combined and one-dimensional spectra extracted using optimal techniques packaged within *stdas*. Since stars were located at different positions orthogonal to the dispersion axis, their spectra suffer constant, positional-dependent offsets, which we corrected empirically by matching absorption features.

The red and blue spectra were integrated over the filter response functions $T(\lambda)$, as shown in Figure 7, to determine each star's observed fluence. The average of these fluences, compared to the observed counts (per second) of the stars in the reference images, give the calibrated flux of one count per second. The difference between the four stars per filter are consistent to within $\sim 5\%$.

Note that this calibration is for *observed* fluxes, and has not been dereddened. Walker & Suntzeff (1990) find that the field surrounding SN 1987A is consistent with a reddening of $E(B-V) = 0.17$, while Scuderi et al. (1996) determine $E(B-V) = 0.19$ from *HST* Faint Object Spectrograph spectra of star 2. These two papers assume $R_V = 3.1$ for the LMC, while Misselt, Clayton, & Gordon (1999) give an av-

erage value of $R_V = 2.6$ using ten sightlines. However, if one assumes the SN, surrounding dust, and these nearby stars all suffer the same extinction, then the dust-scattering model (§2.1) can be applied without any reddening corrections.

5. ECHO MEASUREMENT AND VISUALIZATION

In this section, we present the PSF-matched difference images, describe how light echoes were identified and measured, and discuss analysis and visualization tools that will be used in this work.

5.1. Light Echo Data

All epochs of imaging listed in Table 1 were pipeline-reduced, PSF-matched and differenced as explained in §4. A subset of the resulting difference images are shown in Figure 10. Recall that the WFPC2 PC has 3.6 times higher resolution per pixel and therefore a smaller field-of-view. Since *HST* observations were rarely taken at the same orientation, the images are clipped with respect to ground-based data, and the clipped regions change with epoch.

For all observations, images are shown in a standard north-up, east-left orientation, with major tick marks denoting angular distances of $10''$ each. The innermost echoes were particularly bright up to day 1469, and are washed out at the brightness-stretch used to display the background and outer echoes. In such cases, a $12''$ -square inset centered on the SN is shown at the top right of each panel, scaled in brightness to better-resolve the innermost echo signal. All images are shown with a linear greyscale scaling, the limits of which differ between images to better show the echoes in each particular epoch.

Panels (a) and (b) were taken through the *V*-band and a narrow continuum filter centered at 6067\AA , respectively. In the first case, this image (day 659) was differenced from a sum of the F470 and F612 reference images, weighted to approximately reproduce the throughput of the Johnson filter. This scheme worked well for removing most faint background sources. We compared this image to a difference made against another *V*-band observation from 1990 Nov. 5 (day 1171) and found the background was sufficiently flattened using the combination of narrow filters. The non-standard narrow continuum image from day 750 was differenced against the F612 image, the result of which is of equivalent quality to other F612 difference images. In both cases, it was preferable to use the echo-free reference images rather than the same filter at a later epoch, since this latter option introduces additional confusion from echoes present in the later data.

The data in panel (d) were taken in a dithered pattern by imaging the SN on each of the four extreme corners of the detector. The resulting mosaic has different noise characteristics depending on the amount of overlapping data.

A number of the images, e.g., panels (f), (g), and (i), show the limitations of PSF-subtracting Stars 2 and 3 prior to differencing, also described in §4.5. Star 2 is especially bright and often has significant flux in its wings at a radius larger than can be adequately modeled by an empirical PSF. This can be well seen in panel (g). Additionally, the wings of the model PSF are intrinsically noisy at large radii, and the bright flux from star 2 made even small-scale fluctuations large, producing subtraction residuals within the model-PSF radius. This is most obvious in panel (i).

There are many noteworthy artifacts present in these data. As noted in §4.1, the Poisson noise is highest at the position of a bright star, and will therefore leave a subtraction residual at

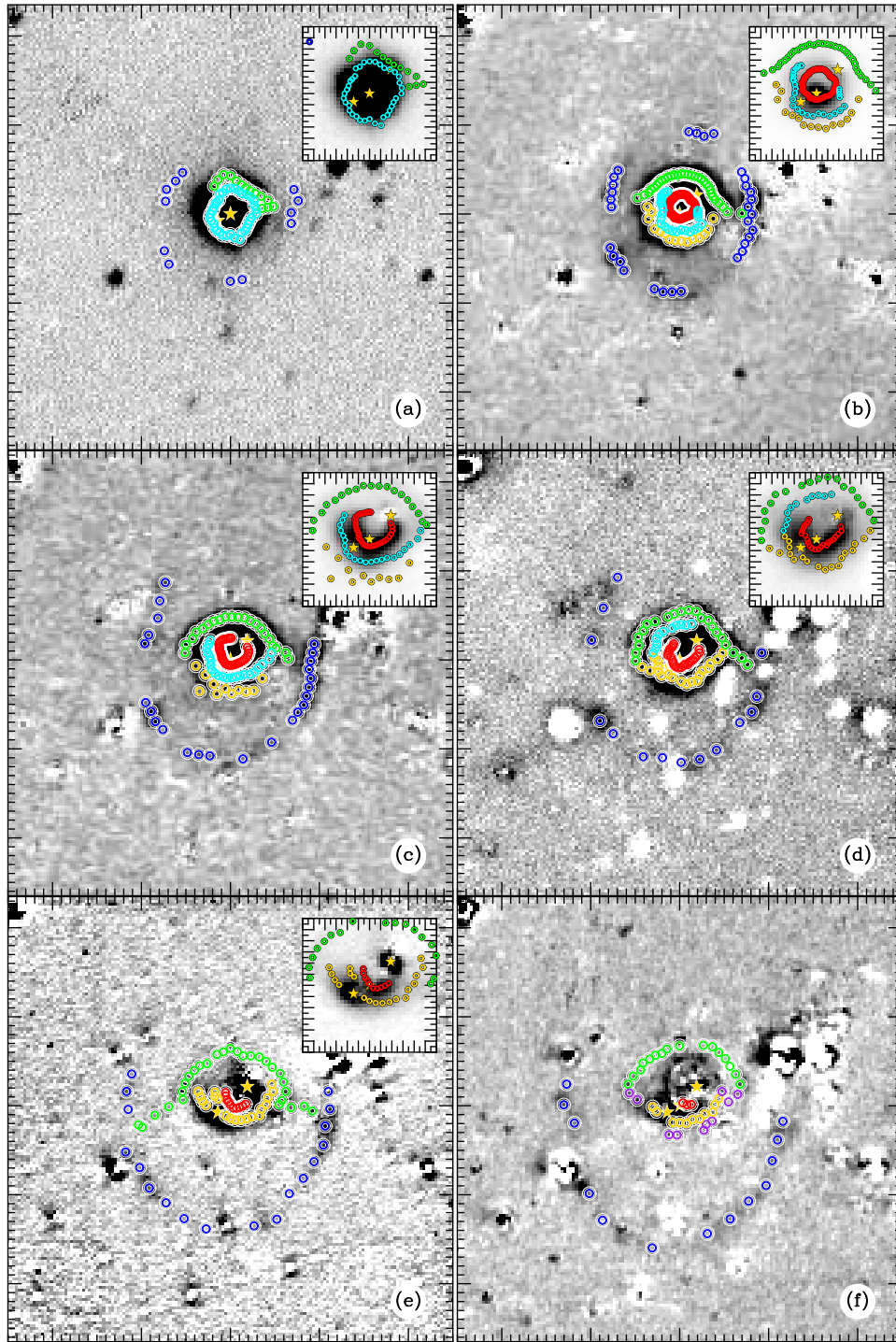


FIG. 10.— Selected $50'' \times 50''$ difference images. North is up, east is left, and major ticks mark $10''$. The position of the SN, Stars 2 and 3 are marked with yellow stars. Echoes are marked by colored circles. The inset shows the central $12''$ at a different color stretch to resolve the innermost echoes. Colors are explained in §5.2.2. (a) V image from day 659. (b) 6067\AA image from day 750. (c) F612 image from day 1028. (d) F612 image from day 1086. (e) F612 image from day 1469. (f) F612 image from day 1787.

its core. Such residuals can be seen throughout the data. Non-linear and saturated stars leave much larger residuals, both as noisy cores and diffuse wings, such as can be seen in the upper left corner or in the bright-star cluster $\sim 15''$ WNW of the SN in ground-based images. Ghosts of bright stars, caused by internal reflections within the detector optics, are particularly noticeable in panels (g) and (i), but can be easily

identified since they generally occur with the same positional offset from all bright stars.

WFPC2 data suffer from a host of image artifacts that complicate echo detection. Foremost are the extended diffraction spikes from bright stars, which can extend over $6''$ (128 pixels) from the source. These have been included in the *Tiny Tim* model PSF, but in practice can never be completely subtracted

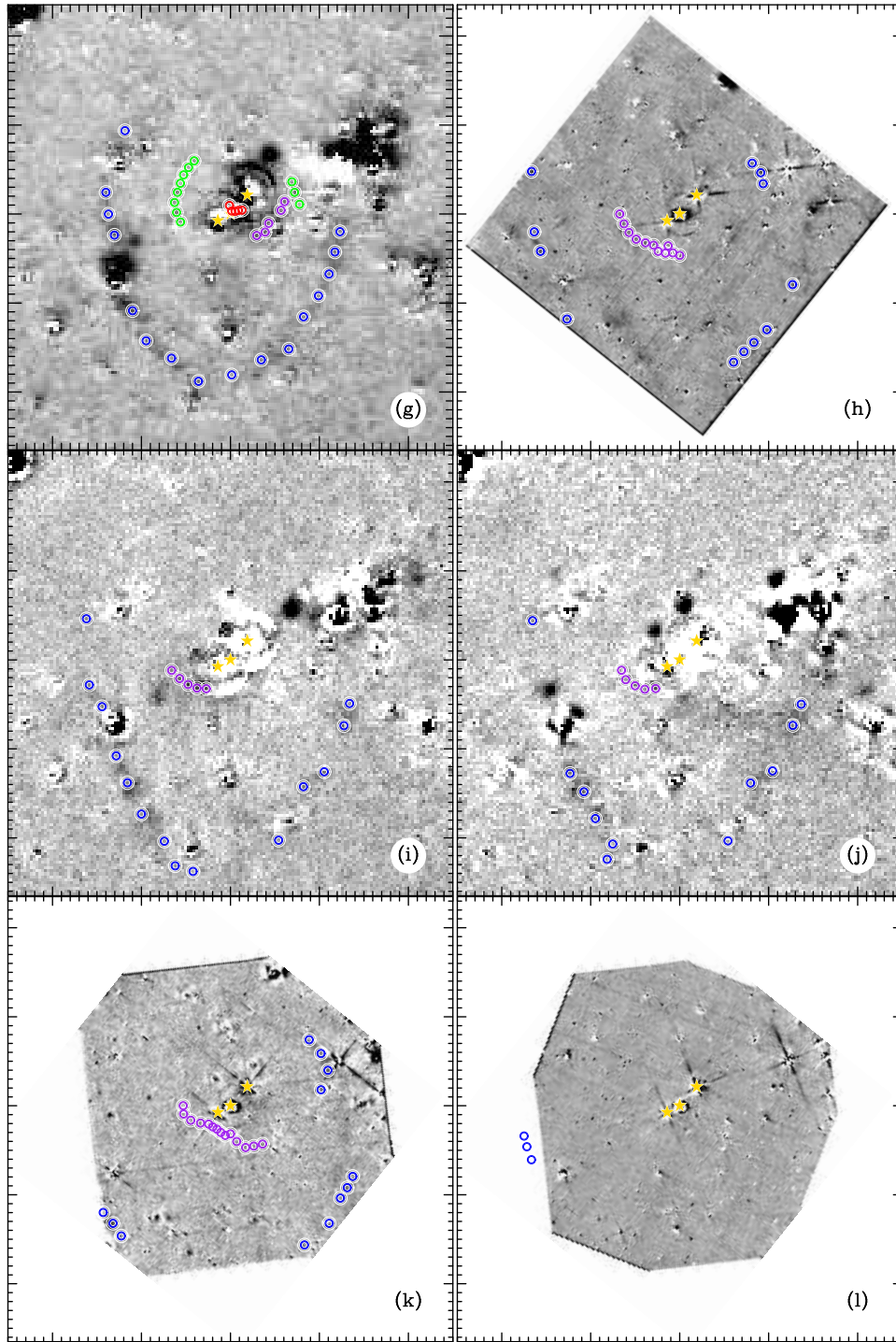


FIG. 10.— continued. (g) F612 image from day 2095. (h) WFPC2 image from day 2769. (i) F612 image from day 2830. (j) F612 image from day 2874. (k) WFPC2 image from day 3270. (l) WFPC2 image from day 3789.

away. Linear banding from charge transfer of bright stars is also omnipresent. Stray light from a bright star positioned within a well-defined avoidance region outside the PC field of view will cause broad arcs and thick bands of flux (fully discussed in the WFPC2 ISR 95-06), which may be seen as dark regions along the left side of panel (h). A smaller, roughly-horizontal dark arc on the right side, roughly $6''$ south of the SN, is also a bright-star artifact. There may be much more echo signal in this image than we could reliably identify (next

section), due to these considerable sources of noise.

5.2. Light Echo Detection

Echoes are present at a variety of positions and over a wide range of surface brightnesses. To measure its position, an echo may either be specified by the total locus of bright pixels, or as the central position of the surface-brightness profile. However, quantifying the structure of extended, diffuse echoes, particularly in the wings of the brightest ones, is dif-

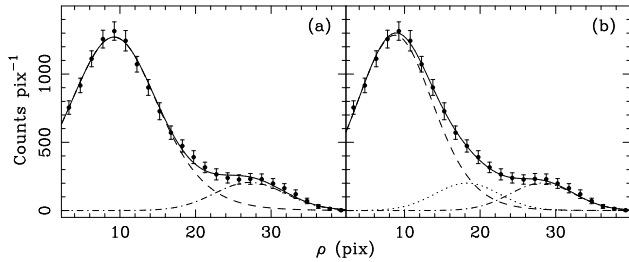


FIG. 11.— Sample radial profile from $PA \sim 50^\circ$ on day 1028 (black points), fit by two and three moffats in panels (a) and (b), respectively. Each individual function is shown with a different line style, and the sum of all functions is drawn in black.

ficult, for a variety of reasons.

Identifying all pixels associated with an echo is comprehensive in giving a better representation of the complete spatial region producing the echo. However, it is important that the echo positions can be visualized in a meaningful way. We experimented with describing echoes three-dimensionally as the complete locus of all pixels (identified with our friends-of-friends algorithm, §4.4) within the surface-brightness profile, and found that when many epochs were rendered in 3-D, the result was very difficult to analyze, since background data were completely obscured by foreground material. Since visualization of the data is critical to interpreting the positional information contained in the echoes, we instead adopted a discretized measurement by which the signal is described as a series of convolved profiles.

Consider a bright, resolved echo with wings that extend to roughly three-times the FWHM of a PSF. This could result from a large, single distribution of dust, or from the convolution of many discrete dust distributions, each with their own density. In the first case, if we identify the echo only at its center, we reject information contained in the wings, namely, that there is dust there. Rather, if we treat the extended flux as the convolution of many discrete echoes, even if there is only one echo present, we will better represent the spatial dust distribution.

The PSFs in most of our images are better described by moffats than Gaussians. The functional form for a moffat is given in Appendix B.1; it is essentially a modified Gaussian that can have a more rapid or shallow profile in the wings. Echoes were identified by fitting multiple moffats to radial surface-brightness profiles, generally measured by summing over wedges of arclength 10° .

Moffats were fit using a highly “hands-on” implementation of Levenberg-Marquardt (LM) minimization (Appendix B.1). Once the surface-brightness profile is measured, the user determines the radial range over which moffats will be fit, and can reject data that are known to be bad i.e., points coincident with subtraction residuals. The user specifies the number of moffats to be fit, and an initial guess for the peak, center, width, and exponent β . Parameters are relaxed into the “best-fit” through iterative calls to the LM algorithm, with parameters replaced or reset when they deviate from reasonable values. “Reasonable” is fairly subjective but not without practical limits. For example, the width of a moffat was not allowed to be smaller than that of a stellar PSF, but was also not allowed to grow larger than $\sim 2\text{FWHM}$.

Each profile is first fit with a single function, and additional moffats are added only as needed to reproduce the flux distribution. It is rare that more than three moffats were needed for

a given echo. An example is shown in Figure 11. The profile (points and error bars) is poorly described by a single Gaussian or moffat, as it has an extended plateau around $\rho = 25$ pix, and will require at least two functions. The best-fit solution for two moffats is shown in panel (a) in black, with the individual functions plotted in different line styles. Note that the fit is only marginal between $\rho = 18 - 26$ pixels. Subtracting these from the profile reveals a third peak centered near $\rho = 18$ pixels. Indeed, including a third function (panel b) is a much better fit, improving the χ^2 residual threefold.

Once a successful fit is made, parameters are varied to ensure the fit is robust. If so, the parameters are recorded, with the width of the echo $\Delta\rho$ taken to be the moffat width σ . Radial profiles were examined at all position angles in each image, and out to a radius of at least $16''$ at early times, and $32''$ at later times, to ensure that faint, distant echoes were not overlooked. The results have been marked in the difference images, and color coded to compare echoes believed to originate in physical associations between epochs.

As can be seen from the difference images in Figure 10, many echoes are faint, lie near bright stars, or in the case of the innermost echoes, near the positions of the SN and Stars 2–3. As with generating the echo-free images (§4.4), faint echo signal was better resolved from the background by coadding the difference images from all filters in a given epoch. Echoes beyond $\sim 5''$ of the SN were generally measured in these summed images. Identification of echoes within $5''$ is complicated by the unknown quality of the PSF-subtraction of the SN and Stars 2–3. Profiles were fit from difference images made using both methods of PSF-subtraction explained in §4.3, and carefully compared for consistent results. When inconsistent, or we felt the subtraction of these sources could influence the result, the measurement was thrown out. In some cases echoes may be present but not reported.

The difference image from day 659 (Fig. 10(a)) deserves special note. At this early date, the SN was sufficiently bright to saturate the detector long before sufficient surrounding signal could be gathered. The PSF of the SN is too bright and extended to perform a PSF-subtraction, however we did find that subtracting a single moffat from the radial profiles left consistent echo signal in the PSF wings, as marked.

5.2.1. Photometry

Once identified as described above, echo brightness was measured as follows. All stars bright enough to leave a detectable subtraction residual were masked from each image. Echo fluxes were measured from these images with annular apertures of the same angular width as used during detection, and with radial widths given by the FWHM of each echo at each position. Since many echoes are extremely faint, we measured each twice, first as the surface brightness through the aperture allowing all data, and again counting only positive pixel values. The corresponding median sky value was subtracted from each surface brightness, and the two values were rejected if less than the propagated noise, or averaged if greater. Counts were converted to fluence using the scaled exposure time from difference imaging and the photometric calibrations described in §4.6.

5.2.2. Discussion

During their detection and measurement, echoes were categorized as belonging to one of three expected structures, listed here in order of increasing radius on the plane of the sky: a

circumstellar hourglass-shaped nebula reported in Crotts et al. (1995), Napoleon’s Hat (Wampler et al. 1990a), or circular echoes at large radii (Bond et al. 1989; Couch & Malin 1989; Crotts & Kunkel 1989) interpreted as the contact discontinuity between the progenitor’s RSG and MS winds (Chevalier & Emmering 1989). These have been color coded in Figure 10 with the primary colors red, green, and blue, respectively. However in fitting Moffat profiles, we found that additional identifications could be made between the hourglass and Napoleon’s Hat, generally colored cyan for echoes looping to the north of the SN, or yellow for positions south. Many of these southern echoes, once examined in 3-D, appeared at a larger distance, consistent with a southern counterpart to Napoleon’s Hat, and have been marked in purple.

That diffuse structure exists between the inner hourglass echoes (red points) and Napoleon’s hat (green points) has been previously reported. Crotts & Kunkel (1991) detected diffuse emission from $3'' < \rho < 12''$ from the SN, measured in semi-circular apertures. Crotts et al. (1995) reported the detection of a “jet-like” feature, several arcsec in length, projecting northeast from star 3 between days 1028 and 1727. These are consistent with the cyan and yellow echoes identified in the same region of the current data, which now map out a much more extensive volume of the innermost circumstellar environment.

Contact-discontinuity echoes have been previously reported by Crotts et al. (1989), Bond et al. (1990), and Crotts & Kunkel (1991) in observations only up to day 1028, while we are able to trace this structure through day 3270. Napoleon’s Hat was imaged as early as days 850 and up to day 1650 by Wang & Wampler (1992), while we detect its signal from day 659 to 2095. We believe this is the first discussion of the southern-counterpart (purple) to Napoleon’s Hat.

5.3. Visualization and Analysis Tools

The 3-D analysis of these echoes is divided into the three broad categories defined above, and will be presented in §6–8, making use of visualization and analysis tools presented here.

5.3.1. Coordinate Definitions

In the following discussion of echo positions, we will make use of a few coordinate systems. On the plane of the sky, we use standard two-dimensional cartesian coordinates. The origin is always defined to be the SN, west is to the right and north is up. Polar coordinates ρ denote the radial distance from the origin, and position angle (P.A.) is measured as the counter-clockwise (CCW) angle from north.

Three-dimensional coordinate systems are shown in Figure 12. Let us define the standard orientation to be the orthonormal cartesian axes with z toward the observer, orthogonal to the 2-D image plane and centered at the SN, with x increasing west, and y increasing north. Thus, the line-of-sight distance, or depth, is measured by z . A point P in space can be described by its cartesian, spherical, or cylindrical coordinates. The spherical distance r is measured from the origin O , with polar angle ϕ measured from north (y), and azimuthal angles are measured in the $x-z$ plane CCW from the line-of-sight (z). We reserve an unscripted θ for the scattering angle at point P , which is the angle between vector \vec{OP} and \hat{z} (under the reasonable assumption that $d \gg r$). Cylindrical coordinates will be used for structures with rotational symmetry about an inclined axis z' . The point P has axial radius π' measured orthogonally

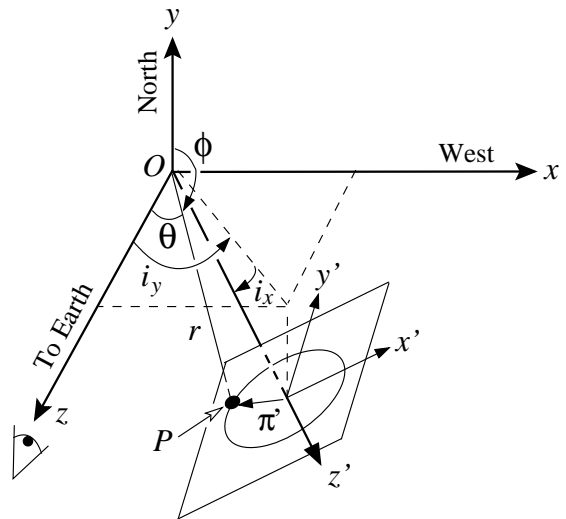


FIG. 12.— 3-D coordinate definitions for discussing light echoes.

from z' . Transformed cartesian axes x' and y' may also be defined in the plane orthogonal to z' containing P .

Rotational transformations are performed using a permutation of the pitch-yaw-roll (PYR) convention, where rotations are performed about each of the three cartesian axes through the triplet $(\psi_z, \theta_x, \phi_y)$, where we first rotate (roll) about z by ψ_z , then about the rotated x (pitch) axis by θ_x , and finally about the rotated y axis by ϕ_y (yaw). Positive rotations are made about an axis following the right-hand rule. When referring to inclinations, the rotation is named for the axis about which the rotation is made, i.e., a rotation north or south is made about the x axis and named i_x . The cylindrical axis z' is then inclined south/north by i_z from the $x-z$ plane, and rotated i_y west/east from the $y-z$ plane.

5.3.2. Three-Dimensional Rendering

To study echo positions in 3-D, we have custom-written graphics software to perform simple renderings, in which the positions of the echoes are transformed to allow viewing from any angle. An illustrative example is shown in Figure 13.

To realize a 2-D visualization of 3-D data, the following steps are performed. First, the user specifies the shift, rotation, scaling, and if desired, translated point of view of the observer and perspective. Using the matrix transformations explained in Appendix C, the data are transformed into a 2-D matrix of positions on the page, with the third dimension saved as a “ z -buffer”, which gives the depth of the point in or out of the page. Data are sorted by the z -buffer position so that points furthest from the observer are plotted first; in this way, distant points behind nearer ones will be covered. To facilitate an interpretation of depth, point size scales with distance from the viewer, with smallest points furthest away.

In viewing 3-D structures, we find variation of point size is not sufficient to give the viewer an immediate sense of depth. We have added a simple ray-traced shading, assuming a single light source positioned behind the observer. In general, ray-tracing on an arbitrary shape is very difficult and involves complicated algorithms such as tessellation. However, all our echo data lie on parabolae of known functional form, thus the normal, or gradient, is always known. Points are shaded by the angle between the normal and line of sight, such that

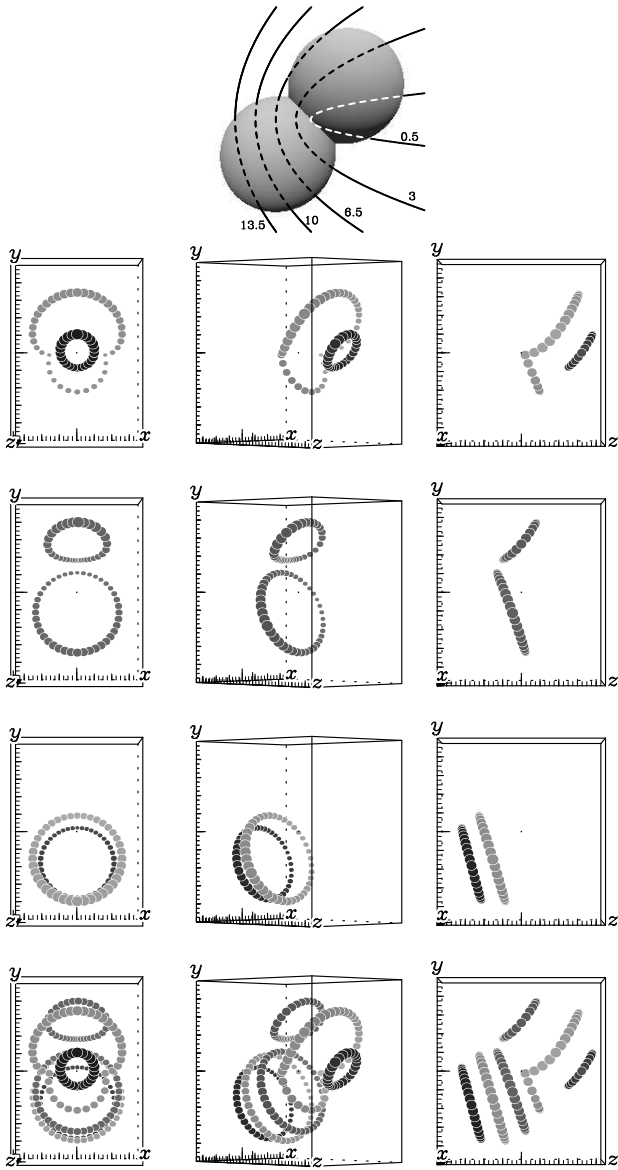


FIG. 13.— Illustrative examples of 3-D renderings of light echoes in a simple bipolar nebula. This non-trivial example is intended to guide the reader in visualizing light echoes, and to annotate the rendering technique. The nebula, depicted at top, is inclined 45° to the line of sight, which is to the right; each lobe is 5 ly in radius, with the centers separated by 8 ly. Five echo parabolae are drawn, each occurring at the time (in years) indicated next to each curve. Below, renderings show the light echoes for the first two parabolae (first row), third parabola (second row), last two parabolae (third row), and all parabolae (last row). Axes are defined as in §5.3.1; axis labels indicate the positive direction. The origin is set at the SN, and is always marked by a black dot. Major ticks mark 2 ly, and the origin is indicated by the longest tick along each axis. The coordinates and axes have been given a slight perspective transformation (Appendix C). Points are shaded using simple ray tracing, and larger points are closer to the observer. *Left Column:* Face-on view (the plane of the sky). *Middle Column:* Oblique view rotated 45° . *Right Column:* Side view from far to the east. Note that the geometry of the nebula, as revealed in light echoes, is only clear when many echoes well-separated in time are considered at once.

0° (modulo 180°) is shaded light, and 90° (modulo 180°) is dark. In practical terms, that part of the paraboloid that is orthogonal to the viewer’s line of sight will appear whiter, and limbs will appear darker. For completeness, the line of sight in this context is orthogonal to the page, intersecting the origin (black dot), and the observer is out of the page looking

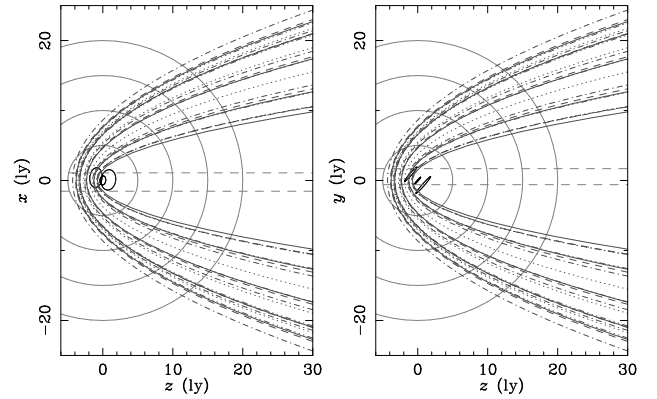


FIG. 14.— Regions of space surrounding SN 1987A probed by light echoes. The left and right panels show the view from far to the north and east, respectively. The probable positions of the three rings (§8.3) are centered at the origin. Circles of constant radii, in multiples of 5 ly, are drawn in light grey. The positions on the plane of the sky of Stars 2 and 3 are indicated by horizontal grey dashed lines. Echo parabolae corresponding to the epochs of observation used in this work (and listed in Table 1) are indicated in dark grey, with line style cycling from solid – dashed – dot-dashed – dotted – dot-dot-dot-dashed in order of increasing epoch.

down.

5.3.3. The Volume of Space Probed by Echoes

Interpreting light echoes is often confusing, since they lie along paraboloids, a surface one rarely encounters when considering geometric intersections. A plane, perpendicular to the line of sight, will appear as a concentric ring, growing in radius with time, until the paraboloid is larger than the material boundary. A thin, spherical shell of radius r , centered on the echo source, will appear first as a ring of increasing radius as the paraboloids expand with time, until the paraboloid sweeps into the rear half of the sphere, after which the ring will collapse and eventually disappear at $t = 2r$.

Other, more complicated geometries can appear in particularly-unrecognizable forms until the echoes have illuminated a substantial part of the structure. For example, the inclined, bipolar nebula in Figure 13, can appear as (1) centered or offset rings, both circular, elliptical, or highly distorted; (2) a distorted figure-eight; (3) multiple distorted rings; or (4) small curved segments, depending on the time and orientation at which echoes are observed.

Figure 14 is more relevant to echoes from SN 1987A, showing the positions of echo parabolae corresponding to all epochs of data in Table 1. Each panel shows a planar cross section of space passing through the origin: the $x-z$ plane viewed from above on the left, and the $y-z$ plane viewed from the side on the right. Concentric circles at radius intervals of 5 ly are plotted to show how these echoes will illuminate structures of different sizes. Also shown is the probable geometry of the three rings, as determined in §8.3, and the line-of-sight positions of Stars 2 and 3 (as horizontal dashed lines), whose relative positions with respect to the supernova are unknown.

5.4. The Three-Dimensional Echo Positions

Echo positions in 3-D are computed from the 2-D positions on the plane of the sky using equation (1). We have implicitly assumed that the echo center is produced by the light pulse maximum (which we take to be 87 days after discovery, §2.3), and correct the observation date in Table 1 by this amount when it enters equation (1). The angular size ρ is converted to

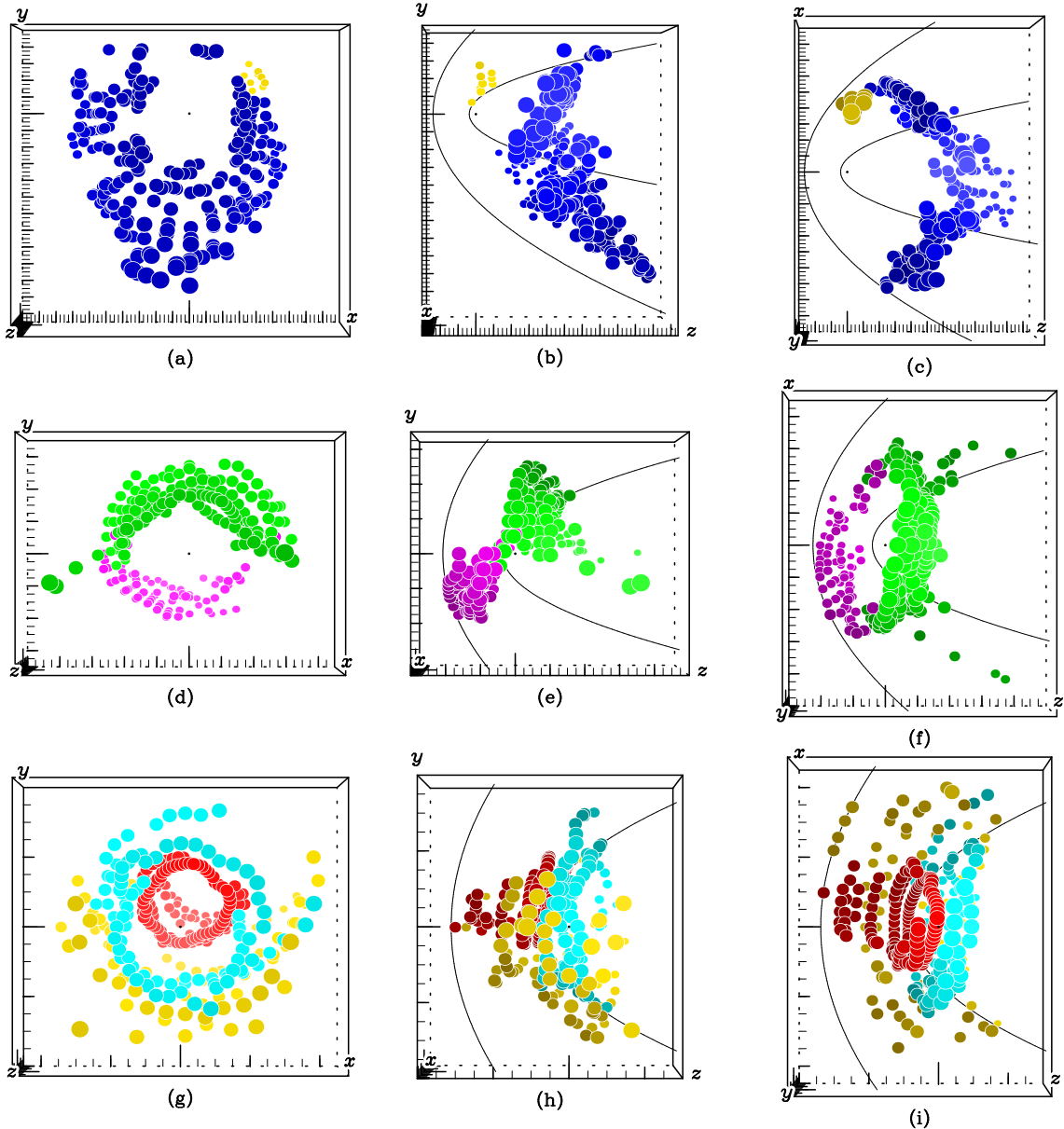


FIG. 15.— Rendered views of all light echoes identified in Fig. 10. Points have been rendered using the method described in §5.3.2; also see Fig. 13. The left column shows observed views in the plane of the sky, the middle column shows views from the side (far to the east) and the right column shows views from the top (far to the north). Parabolae from the earliest and latest epochs at which echoes were observed are indicated in the side and top views. Point colors correspond to those in Fig. 10 except for the gold points in the top row, which denote echoes found in WFPC2 images which could not be resolved from the residuals of nearby bright stars in ground-based images. Note that the field-of-view changes between rows, but major tick marks always denote 2 ly. *Top row:* Contact discontinuity echoes. *Middle row:* Napoleon’s Hat and southern counterpart. *Bottom row:* Inner circumstellar hourglass echoes.

physical units assuming the SN of 50 kpc away. This value is a good average between many of the derived distances to the LMC, which vary between 45–54 kpc (Gould & Uza 1998; Feast 1999; Romaniello et al. 2000).

The 3-D positions of all echoes identified in Figure 10 are rendered in Figure 15, using the methods described in §5.3.2. The top, middle, and bottom rows show the data for the contact discontinuity (CD), Napoleon’s Hat (NH), and the inner circumstellar (CS) material, respectively. Except for the gold-colored points in the top row (see below) colors correspond to those indicated in Figure 10. A rigorous analysis of these data is presented in §6–8, however we give a short qualitative discussion of the echoes below.

5.4.1. The Contact Discontinuity

In the plane of the sky (panel *a*), there is no data within $\rho = 5$ ly of the SN. This results from the lack of echo imaging prior to 1988 December; this is seen in panels (*b*)–(*c*), for which there can be no data interior to the inner parabolae. There are two noticeable holes in the eastern blue echoes at (x, y) coordinates $(-7, -1)$ and $(-10, -6)$ ly, since a saturated star lies at each position. The bulk of the echoes are located between 20 ly south and 4 ly north of the SN, with very few echoes positioned further north. Since light echoes symmetrically probe all regions of space around the line of sight, this suggests that there is little structure in front and to the north of the SN, with the structure being illuminated inclined predominantly south

of the line of sight.

The distribution of blue echoes east and west of the line of sight is fairly symmetric, however echoes extend to only $\rho = 11$ ly west, while they are present to the east up to $\rho = 14$ ly. Comparing the two halves, there are eastern counterparts for all western echoes, yet there are no western counterparts between P.A. 250° – 300° to the eastern echoes at $\rho > 9$ ly from P.A. 60° – 110° . Since there is a cluster of bright and saturated stars in this western region, which makes reliable detection impossible, the absence of westerly echoes may not be meaningful. To the south, the echoes extend beyond $\rho = 14$ ly. These southern points do not appear symmetric about the y axis, but rather about an axis rotated 5° – 10° eastward.

When viewed from the side (panel *b*), the eastern/western points lie 4–14 ly in front of the SN, in a mainly vertical distribution extending 8 ly north and 12 ly south of the line of sight. The southern echoes are primarily oriented linearly along an inclined axis that points toward the SN. These echoes extend 10 to 20 ly in front of the SN, corresponding to radial distances of 14 to 28 ly. From this point of view, the southern echoes have a thin, sheet-like quality to them.

Panel (*c*) shows the top view, from which we see that the eastern/western material follows a thin, curved surface that may be wrapping around the SN. These points lie at a fairly constant radius (in the x – z plane) of 12–14 ly from the SN. There is greater scatter in the eastern echoes than to the west, however both sets appear thin in the radial direction. This suggests the echoes may be the walls of a shell-like structure, such as a cylinder or spheroid. In contrast, the southern points again appear thin and sheet-like.

The geometry of the complete structure is unclear from this subset of points. It may be a conical or prolate shell, although from only these data, it appears the structure may not wrap completely around the SN. Note that, aside from the small number of gold-colored points (see below) echoes do not appear north of the SN. Instead, the material seems to stop abruptly along the northern edge of the early echo parabola (panel *b*).

A small subset of the echoes have been colored gold. These points were identified in WFPC2 images very close to the bright northwest star cluster (P.A. 300° , $\rho = 15''$). As mentioned above, large residuals from these closely-spaced, bright stars made echo identification difficult-to-impossible in ground-based images. As they were observed at late times, these points lie 6–8 ly behind other echoes similarly located on the sky. No counterparts to these echoes are seen to the east, or at any other position angle at this radius and depth. These points do not immediately appear associated with the rest of the CD echoes, however we include them for completeness.

5.4.2. *Napoleon's Hat*

Figures 15*d*–*f* show the 3-D positions of the NH echoes. As the northern echoes are already a known feature, we begin by describing them. These “NH-north echoes” are shown in green in Figure 15.

The NH-north echoes are reasonably symmetric between east and west on the plane of the sky (panel *d*). Viewed from the side (panel *e*), the bulk of the material lies along a thin shell that loops around the northern half of the three rings. At their closest to the observer, these echoes appear aligned with the equatorial plane containing the ER, and extend outwards roughly 1.5 ly beyond the NOR. This shell looks to be aligned with the inclination of the rings, both south (as viewed from

the east) and east (viewed from the north). From the side, the echoes could lie on a cylinder or spheroid aligned with the ring axis. Viewed face-on, the northern points are closer to the SN than to the east or west, suggesting that the structure has an elliptical cross section.

Two nearly-horizontal features protrude from this shell toward the observer, appearing horn-like when viewed from above (panel *f*). In the following discussion, we refer to these as the “horns,” to distinguish them from the rest of the NH material. These are the echoes seen in early imaging that bridged between NH-north and the larger-radii CD echoes (Fig. 10).

Between 1992–1996, arc-like echoes appear 1.5–4 ly south of the SN. These are disguised from echoes arising in the same region at earlier times for two reasons. First, most of these echoes are isolated features on the sky, i.e., in radial profile they have distinct flux minima on either side of the peak, as opposed to the earlier southern echoes, which appeared as a convolved complex of nearby features. Second, the 3-D positions of these points are consistent with a thin shell-like counterpart to the NH-north echoes, while earlier echoes are widely dispersed around positions interior to this shell.

We discuss these interior echoes within the context of circumstellar material below, while the shell-like points are identified as NH-south. These are shown in Figure 15 in purple. Considered independently of the NH-north points, these echoes appear elliptical (panel *d*) and lie along a thin shell looping around the southern half of the three-rings. It therefore appears that both northern and southern shells lie on the same structure, which (despite the temptation to call these “Napoleon’s Collar”) we will simply refer to as NH.

5.4.3. *Inner Circumstellar Material*

The 3-D positions of the CS echoes are rendered in Figures 15*g*–*i*. Echoes passing within $1''$ of the SN were identified as part of the hourglass nebula (Crotts *et al.* 1995), and have been colored red. These form (nearly) complete loops at early times (up to day 1028), collapsing with time into increasingly-shorter arcs until only a single point was distinctly-identifiable on day 2462. Outside of these innermost loops, those echoes that form (nearly) complete loops or pass north of the SN have been color coded cyan, and those that remain primarily south of the SN are shaded gold. This particular choice of categorization is arbitrary, and has been made only for clarity in viewing the echo positions.

Viewed from the side (panel *h*), the red echoes do indeed appear to trace out a hollow, conical or tube-like surface. Visually, these points appear inclined roughly 45° to the line of sight, with the opening oriented north and away from the observer, while viewed from the top (panel *i*), they appear to lie along an axis rotated 10 – 15° from z . That there are no loop-like counterparts in front and slightly north of the SN is a selection effect of the positions of the echo paraboloids, as shown in panel (*h*) and Figure 14. This latter figure does suggest that the earliest echoes may have skirted the southernmost edge of the hourglass. Panel (*h*) does show cyan and gold echoes positioned roughly at these expected positions. There is, however, *no a priori* means to establish which of such echoes intersect the hourglass, versus which echoes are from material external to that structure. The gold echoes, when viewed from the side, are suggestive of a larger double-lobed structure surrounding the inner hourglass. Again, physical association of these points is difficult to establish, and we defer further discussions to our quantitative analyses in §8.

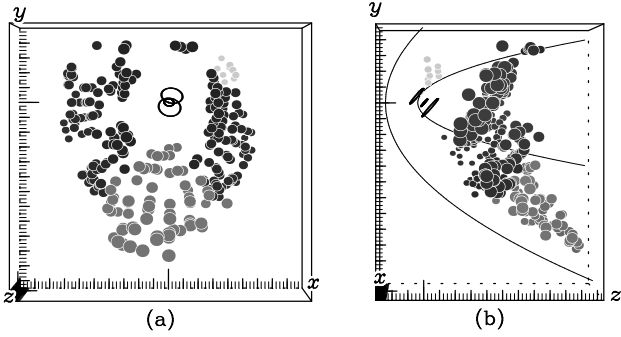


FIG. 16.— As Fig. 15a–b, showing only the CD echoes, where now “shell” echoes are dark grey, “radial” echoes medium grey, and light-grey points denote the WFCP2 echoes that are difficult to interpret (§6.1.1). The probable positions of the three rings (§8.3) are indicated in each panel.

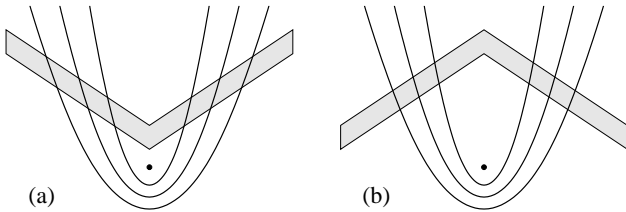


FIG. 17.— Schematic intersection of (a) outward-facing and (b) inward-facing cones with light echoes. The source is marked with a solid dot.

6. CONTACT DISCONTINUITY ECHOES

As explained briefly in §1, a strong body of evidence suggests that the progenitor star passed through a RSG phase before terminating as a BSG. Those echoes identified as part of the contact discontinuity (CD) between the RSG and MS winds were color coded blue in Figure 10, and blue or gold in Figure 15a–c. Figure 16 shows the same 3-D echo positions, but in greyscale. In §5.4.1, we noted that the geometry of the eastern/western points appeared different from those to the south (P.A. 150°–210°). Here, the former points have been shaded a darker tone than the latter, and the WFCP2 data for which there are no ground-based analogs are shaded the lightest.

6.1. Geometry of the CD

The reader may wish to skip to §6.2 for a summary. From the side (Fig. 16b), the CD echoes appear to lie along a conical surface. A cone, opening away from the SN, and inclined roughly 10° south, will contain many of the echo points. However, the fit is only good for the southern material (medium-grey points). Consider the intersections of echo parabolae with cones, as shown in Figure 17. Recall that the parabolae become larger with time. Light echoes through an outward-facing cone (panel a) intersect it at increasingly-large distance from the source with time, consistent with the southern points (medium grey points). However, eastern/western material (dark-grey points) remain at constant or decreasing distance with time, more consistent with a spheroidal shell, or an inward-oriented cone (panel b). This implied “saddle” geometry is unlikely, since no counterparts to the southern echoes are observed to the north. Qualitatively, the structure of which these echoes are a subset is unclear, and we proceed to a more detailed analysis.

6.1.1. Geometry in Spherical Coordinates

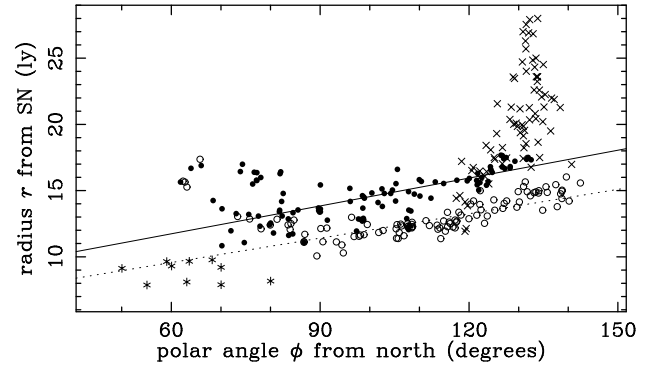


FIG. 18.— CD light echo positions in spherical coordinates ϕ versus radius r . Shell (dark grey) echoes are plotted with circles, filled for those east of the line of sight, and open for those to the west. Radial (medium grey) echoes are plotted as \times , and the small subset of WFCP2 echoes to the northwest (light grey) by asterisks. The best-fit lines through the east and west shell echoes are indicated by solid and dotted lines, respectively.

As the eastern/western echoes appear to form a curved surface surrounding the SN, let us first look at these data in the spherical coordinates ϕ and r , shown in Figure 18. Medium-grey points in Figures 16 are plotted as crosses, light-grey with asterisks, and dark-grey as circles, filled or open if they lie east or west of the line of sight. Roughly speaking, the circles lie in a horizontal band between 10 and 18 ly from the SN, while crosses are distributed vertically at constant ϕ . A radial line will appear vertical in such a plot, while a sphere will appear horizontal. In the broadest terms, the circles seem to form a shell-like feature at roughly constant radius from the SN, while the crosses form a radial feature at roughly constant inclination. In the following discussions, we will distinguish these sets of points by referring to the crosses as a “radial” feature and the circles as a “shell.”

The radial echoes extend 14–28 ly from the SN. Their distribution is nearly vertical about $\phi = 130^\circ$, consistent with a radial line inclined 40° south of the line of sight. A few points are located at $r \lesssim 17$ ly and $\phi = 120^\circ$. Whether these points are part of the shell, or yet another structure inclined 30° to the line of sight, will be addressed in the next subsection.

To the west (open circles), the shell is radially thin at all angles. At any given ϕ , these points show a scatter of roughly 2 ly, which combined with the intrinsic echo width ($\Delta z \sim 1-3$ ly; see Sugerman 2003) suggests a shell thickness of ~ 4 ly. To the east (filled circles), the shell thickness increases from a scatter of 1 ly at large ϕ to up to 6 ly at small ϕ . Both eastern and western sets of points are visually suggestive of curved structures, nearest to the SN around $\phi = 90^\circ$ (i.e., the $x-z$ plane), and flaring outward in radius above and below that plane. To test this, we first examine how well each set is described by a linear fit. These are shown as solid and dotted lines for the eastern and western points, with an RMS scatter about each line of 1.1 and 0.8 ly, respectively. Both lines are generally a good fit to the data, however at $\phi < 90^\circ$ both sets of points deviate to larger r . Points at $\phi \gtrsim 120^\circ$ may marginally deviate from these lines to larger radii.

The western half of the shell is closer to the SN by 2.7 ± 1.4 ly, using the best-fit lines described above. Although only a 2- σ difference, this could indicate an asymmetry in this structure. If the CD, whatever its actual shape, has symmetry, then its axis is spatially offset from the SN. If we require this axis to pass through the SN, then the asymmetry may lie in the hydrodynamic interaction that formed this structure, including

the outflows from the progenitor, and the medium into which they propagated (e.g. interaction with the remnant of a previous, nearby SN).

A cartesian line that does not intersect the origin will appear as a convex curve in spherical coordinates, symmetric in slope about the minimum in r . That the shell points appear to lie on such curves suggests they are part of a nearly-linear surface of revolution, such as a cylinder or a cone. Comparing Figure 18 to the expected distributions for various geometric surfaces, shell points could be consistent with an inclined ellipsoid, cylinder, or inward-opening cone. Heuristically, the inward-facing cone may be the best fit since its apex translates into a highly inclined, nearly vertical distribution, as seen for the radial points.

The northwestern WFPC2 echoes, marked as stars in Figure 18, are nearly colinear with the western shell material. This could be consistent with the conical distribution described by the rest of the CD echoes if the cone becomes more cylindrical as it passes the SN. However, it is difficult to reconcile this structure with the shell material that flares to larger radius at $\phi < 90^\circ$, indicative of a cone growing to larger radii as it nears the SN. The association of these points with the rest of the CD echoes is unclear, and they may instead arise from isolated inhomogeneities in the surrounding ISM, or an unusual, extended image artifact, rather than from stellar outflows.

6.1.2. Finding the Orientation

If the shell and radial material are part of a spheroidal or conical structure, it should have a well-defined axis of symmetry. We assume this axis passes through the SN, and attempt to find it by χ^2 minimization. Note that only a portion of the physical CD structure has been illuminated. A numeric minimization of some merit function will always be more successful at recovering the axis of an object with a complete cross section (e.g., a full cylinder), than with a partial one (e.g., a cylindrical segment). Thus, exploring this material's geometry is inherently uncertain.

First, we directly fit the axis by finding the line that minimizes the geometric distance to all echo points (Appendix B.3). Constraining the fit to have zero offsets, we find the best-fit line is inclined 37° south and rotated 8° east of the line of sight. The formal error of this fit is 0.5° per axis of rotation, and while it is robust to perturbations in the parameters, we expect the actual uncertainty is higher.

The echo points are transformed onto a cylindrical coordinate system about this line, designated by the primed coordinates in Figure 12. Figure 19 shows the “radial profile” of axial position versus radius for the transformed data. As noted in §5.2, we only measure the center of echoes, therefore points have 1–4 ly uncertainty in their spatial extent. Symbols are the same as in Figure 18, except for the “+” marks, which we discuss shortly. In these coordinates, a cylinder will appear as a horizontal feature, a regular cone as an inclined line, and a biaxial ellipsoid (with major axis along z') as a curved feature with $d\pi'/dz' < 0$ and $d^2\pi'/dz'^2 < 0$. We have again plotted the best-fit lines through the shell material, which show that the bulk of it lies on a linear incline, and thus delineates a conical structure.

The shell material is best fit by the line $\pi' = (14.4 \pm 0.4) - (0.5 \pm 0.04)z'$, giving the conical structure an opening angle of $\sim 53^\circ$. Considered independently, the eastern and western halves are fit with zeropoints of 16.2 ± 0.5 and 13.3 ± 0.5 ly, and slopes of -0.62 ± 0.05 and -0.43 ± 0.05 , respectively. Although these values differ, the eastern points appear only

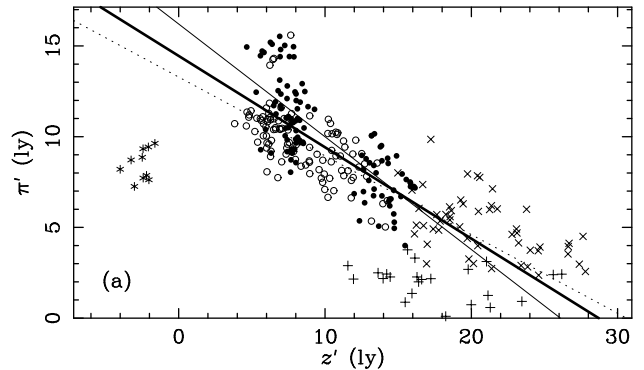


FIG. 19.— CD echoes, transformed into cylindrical coordinates with z' along the axis of symmetry given by $i_x = 37^\circ$ and $i_y = 8^\circ$. Coordinates are shown in Fig. 12, with z' along the axis, and π' measured radially from it. Symbols and line-styles are the same as Fig. 18, with the heavy solid line is the best fit through all data. A subset of the radial echoes have been marked by +, indicating “cylindrical jet” material.

marginally offset to higher radii than those to the west. Close to the SN, the shell flares outward to a larger radius of 15–16 ly, as first suggested in Figure 18. The cone continues with roughly constant slope and thickness until shell data ends at $z' = 16$ ly. Much of the radial material is colinear with the shell echoes between $z' = 15$ and 28 ly, but with slope -0.25 , for an opening angle of $\sim 30^\circ$. Treating the shell and radial points as part of a single “conical-shell” structure, we find that it does have a curvature to its profile.

A small subset of radial material between $z' = 11$ –26 ly lies at π' just below the shell material. After considering many possible inclinations (§6.1.3), we have identified the points marked by “+” symbols as behaving differently from the bulk of the radial data. If we consider these points to be part of the conical shell, then the entire ensemble of radial points (\times and $+$) have the same slope as the shell-only echoes (circles). In such a case, the conical shell thickens with distance from the SN, and approaches an apex or termination at a distance of $r = 28$ ly. The subset of radial points in Figure 18 that are consistent with a 30° inclination (§6.1.1) are all found within this new set of points. If we treat them as an independent feature, they are well fit by a horizontal line. These echoes lie within $\pi' < 3$ ly, and extend inward toward the SN, suggestive of a quasi-cylindrical region. If a narrow jet pierced through the CD, its interaction with the RSG wind might have formed such a narrow conical or cylindrical high-density feature. With this in mind, we will treat these points as a separate feature from the conical shell, and will refer to them as the “jet.”

Finally, the WFPC2 echoes northwest of the SN are located at a radius inconsistent with the slope of the other CD echoes. Since there are no echoes located between $z' = 0$ and 4 ly, one can only speculate how the profile of the CD structure changes as it passes the equatorial plane. If, as noted above, the shell flares out to large radius at small z' , these WFPC2 echoes do not lie on the boundary of a structure, but instead may simply be part of a local overdensity of gas and dust, as noted previously. If the profile does curve in, and it contains these echoes, then one must ask why no material joining the shell to these points was illuminated. These echoes appear isolated, and have no counterparts at other P.A.s, thus we give them little weight when considering the CD structure.

Since the CD echoes appear to lie along a conical shape,

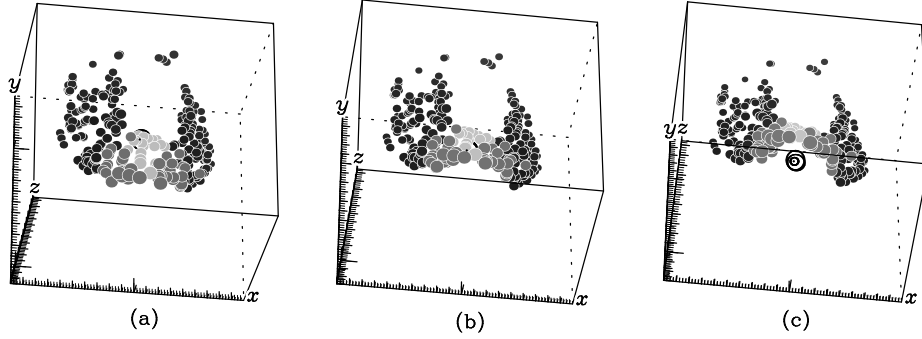


FIG. 20.— Renderings of CD echoes (Similar to Fig. 16), showing possible symmetry axes at (a) 30° , (b) 40° , and (c) 50° . The northwest WFPC2 data are not plotted (§6.1.1), and the “jet” material (§6.1.2) is now shaded lightest grey.

its inclination should be better studied by performing the χ^2 minimization of a cone rather than a single line. Unfortunately, the minimization of this merit function (Appendix B.4) provided few useful results. Because the echoes trace out only a limited portion of the structure on which they are located, the best-fit cones have inclinations larger than $i_x = 60^\circ$. Such highly-inclined cones are poor fits to the total dataset, but minimize χ^2 by passing very close to a large subset of points at large distance from the SN. As a result, the remaining discrepant points effect the merit function very little, even though the overall fit is poor. While these fits give little information on the inclination of the conical structure, inclinations in the range of $i_x = 30 - 50^\circ$ consistently require rotations of $i_y = 5 - 10^\circ$. In the following subsections, we describe alternate techniques for establishing the most probable orientation of this conical structure.

6.1.3. Alternate Orientations

As it cannot be established whether the proposed inclination is correct, we adopt a different approach by studying how the radial profiles vary over a range of inclination angles. We consider inclinations i_x between 30° and 56° from the line of sight, tested every 2° , with the corresponding rotation i_y given by the best-fit 3-D line to the data at each inclination. For clarity, the CD echoes are rendered for $i_x = 30^\circ$, 40° , and 50° in Figure 20. The jet material has been shaded light grey, to distinguish it from the radial echoes. Qualitatively, the echoes appear to lie on a conical surface of revolution only for the 40° and 50° inclinations. An inclination near 40° has the most overlap (in projection) of the jet echoes and the SN, which strengthens its interpretation as a narrow, cylindrical jet. At 50° , the radial and jet material lie neatly on a surface of circular cross-section, suggestive of demarcating the edge of an evacuated, cylindrical region, perhaps connecting to the ER and SOR. Although this inclination is not suggested by the previous analysis, we question whether it could be a viable fit to the full set of CD echoes.

As in Figure 19, we transform the CD material into cylindrical coordinates about each inclination axis, and generate radial profiles through which we measure the best fit lines. The slopes of those lines are summarized in Figure 21. The slope ($d\pi'/dz'$) of the shell material is fairly uniform between -0.45 and -0.51 , with this steepest slope occurring at $i_x = 42^\circ - 44^\circ$. Although the variations appear smaller than the quoted error bars, we note that uniform positional errors of unity were assumed in the least-squares fits. The radial echoes are nearly horizontal at the smallest and largest inclinations, with the

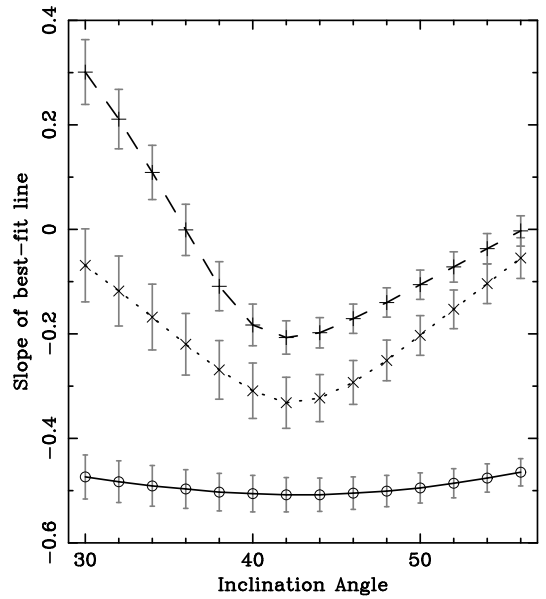


FIG. 21.— Slopes of the best-fit lines $\pi' = a + bz'$ through the CD echoes, inclined to the south as given along the abscissa. Symbols denote the same material as Fig. 19, except all shell material is represented by open circles. Grey error bars show the formal uncertainty from the least-squares fit, assuming equal errors for all data.

steepest slope also occurring near $i_x = 42^\circ$. At no point are the slopes of the radial and shell echoes equal. This reinforces the interpretation from §6.1.2 that radial points, if axisymmetric, lie on a structure with much shallower opening angle than that of the shell material. The slope of the jet material is very sensitive to inclination, with the implied axisymmetric structure appearing as a wide cone opening away from the SN at $i_x = 30^\circ$, a narrow cylinder at $i_x = 36^\circ$, or a narrow cone opening toward the SN at $i_x > 38^\circ$. Are these results consistent with viewing the hypothesized conical shell at different inclinations?

Consider viewing a complete frustum at different inclinations, as sketched in Figure 22. The radial profile of π' versus z' is linear only close to the true axis, marked as line A. Away from A (e.g., line B) the plots become highly non-linear, and the slope of the best-fit line becomes more vertical, with increasing inclination away from the true axis. This is shown in Figure 23a, which is generated by viewing a simulated frustum at different inclinations. Here, the slopes are steepest at the highest inclinations, contrary to the data in Figure 21. Ex-

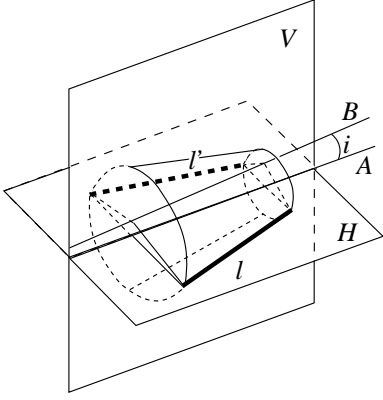


FIG. 22.— Cartoon sketch of a frustum, and its intersection (l, l') with the horizontal plane H . The axis of symmetry is line A , common to planes V and H , where V and H are orthogonal. We consider inclinations i of the axis relative to line B , also in plane V .

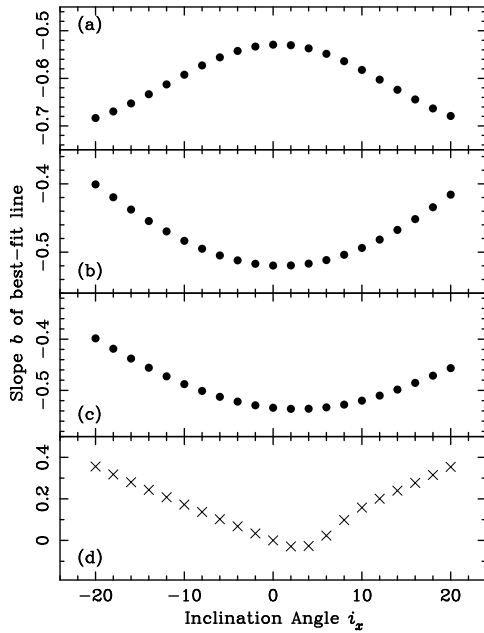


FIG. 23.— Data similar to Fig. 21 but for a simulated frustum, oriented as in Fig. 22, with its axis along line A , and inclinations i_x made in the plane V . Panels (a)-(c) use a frustum with large opening angle, simulating the shell echoes. Best-fit slopes are calculated as follows: (a) Points sampling the complete surface of revolution. (b) Points within 30° of plane H . (c) Points from 30° below to 60° above plane H , meant to simulate the positions of actual shell echoes. (d) Points along the upper-half of a frustum with small opening angle, simulating the jet material.

amination of the renderings in Figure 20 shows that for the shell and radial echoes, material is primarily located left and right of the symmetry axis, not above and below. Since the inclinations move this axis through the region with no echoes, there is no material present to cause the effect just described.

Rather, the situation is akin to rotations in the plane of reflection between two curved sheets. Reconsider Figure 22, in which two lines l and l' , with reflectional symmetry about plane V , lie in plane H . The slope of line l as measured from line B (inclined in V) will be similar to, but shallower than, the slope measured from line A , for moderate inclinations. If we instead consider thin, curved sheets located on the frustum (similar to the shell and radial material illuminated by echoes), but only extending some angle above and below H ,

the same effect will occur. This is shown in Figure 23b. Under these circumstances, the slopes are the shallowest at the highest inclinations, consistent with the conical-shell data.

If the shell and radial material were uniformly distributed above and below the axis of symmetry, then Figure 21 would imply the actual inclination is near 43° . However, as seen in Figure 20, more material is above the axis than below it. Figure 23c shows the expected variation for a frustum wedge chosen to approximate the actual distribution of data. Now the steepest slope occurs at an inclination a few degrees larger than that of the true axis, leading us to favor an inclination $\sim 2^\circ$ – 4° less than 43° , i.e., near $i_x \simeq 40^\circ$, for the conical-shell material.

If we interpret the jet material as a segment of narrow, semi-cylindrical sheet, its change in slope should appear as Figure 23d. Similar in appearance to the jet data in Figure 21, these simulated points also suggest the extremal slope is offset by 2° – 4° from the true axis. If we continue to interpret the jet as an independent feature, its inclination may also be in the range 38° – 40° .

6.1.4. The Conical-Shell Cross Section

From the previous arguments, the favored inclination of the conical shell is around $i_x = 40^\circ$, although the alternate values of 37° and 50° have yet to be ruled out. If the echo points do lie on a surface of revolution, the cross section as viewed along its axis should appear circular. An elliptical cross section would either indicate a viewpoint inclined to the symmetry axis, or that the surface is inherently elliptical. We investigate this by fitting ellipses to cross-sectional profiles through χ^2 minimization, as explained in Appendix B.2. Since the axial radius π' varies with z' for the conical-shell, points must be normalized to a common radius. The radial profile at a given inclination is divided into bins of width 1 ly in z , then axial radii are normalized by dividing out the average value in that bin.

For each inclination tested in the previous subsection, the cross-section of the echoes is calculated (viewed along the axis) as described in §6.1.2. A subset of these are shown in Figure 24 for the inclinations noted in each panel. The shell echoes lie closely scattered along two arcs of a circle or ellipse. With increasing inclination, less material appears under the abscissa. At small i_x , the radial points appear to form the bottom edge of the ellipse, and become intermixed with the shell echoes at higher inclination. The jet material form a smaller circular shape at moderate inclination, and eventually merge with the other material into a single ellipse at $i_x = 56^\circ$, supporting the suggestion from Figure 20(c) that the inclination axis is large.

Assuming one of these to be the true inclination, we can build the conical shell implied by its radial profile, then test whether the other cross sections are consistent with inclined views of that data. This is shown in Figure 25. Linear fits to the radial profiles at inclinations of 37° , 42° , and 50° define the function $\pi'(z')$ for the shell and radial data. For each inclination, the function is rotated about the z' axis through position angles chosen to approximate the actual cross section. Points along these surfaces are chosen at random, and given random scatter, to form a simulated conical shell. Each shell is shown in a single row, as labeled on the left side, and inclined north or south of z' by the angle given at the top of each column.

Suppose the CD is actually inclined at $i_x = 37^\circ$. That panel in Figure 24 should be compared with the 0° inclination of

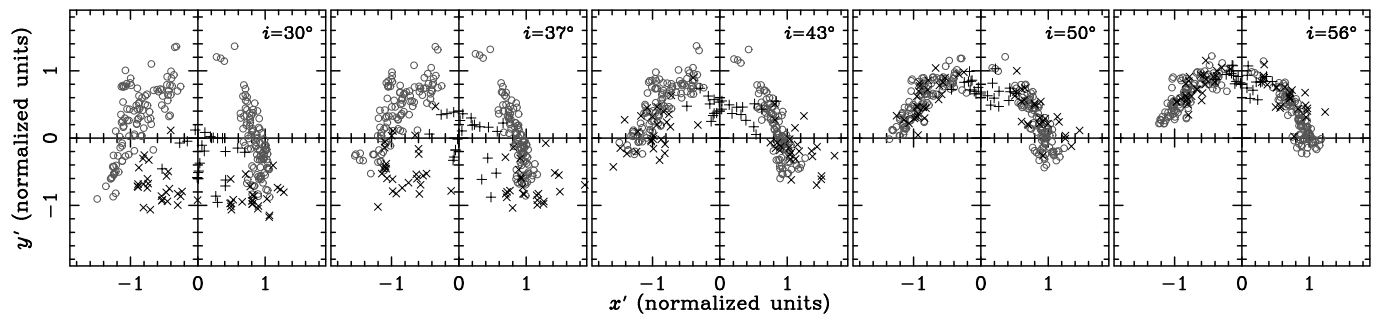


FIG. 24.— Cross sections of CD material, viewed along a hypothetical symmetry axis with inclination as noted in each panel. All data are normalized by their average distance $\langle \pi' \rangle$ measured in bins along z' . Labels x' and y' are the cartesian axes defined in Fig. 12. Symbols are the same as Fig. 19, except all shell material is designated by open circles, which are shaded grey to facilitate the viewing of other symbols. Comparison of this figure with Fig. 25 shows the most probable CD inclination is near $i_x = 40^\circ$ (see text, §6.1.4)

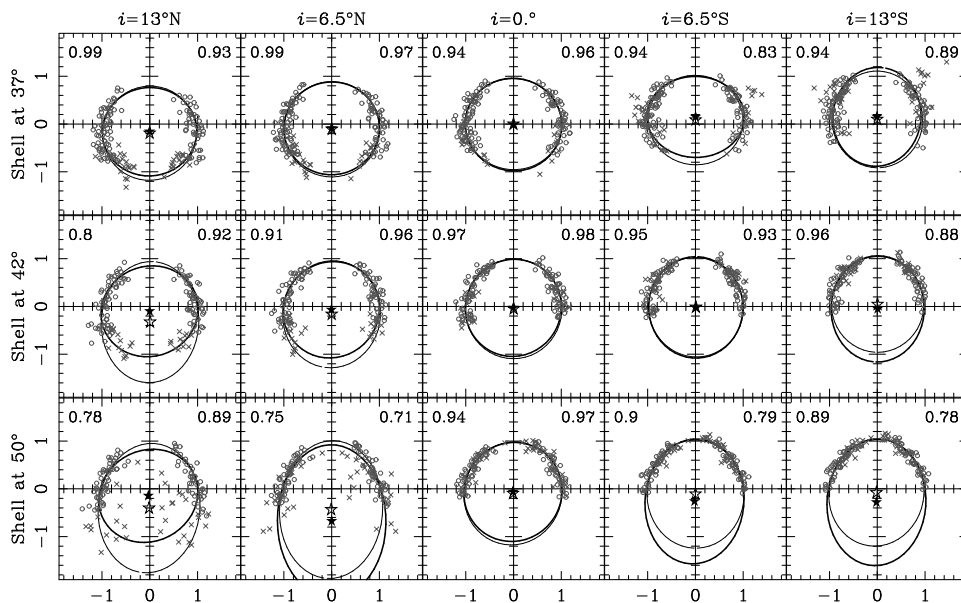


FIG. 25.— Cross-sectional views similar to Figure 24, but for simulated conical shells. Each shell reproduces the CD data viewed at the inclinations listed at the left of each row, and is viewed at the inclinations listed at the top of each column. Open circles represent simulated shell material, and simulated radial material is marked by \times . Also plotted are the best-fit, 5-parameter ellipses and centers through the full dataset (thick lines, solid star) and only through the shell points (thin lines, open star). The ellipticity b/a for each fit is given at top right and left of each panel, respectively.

the top row in Figure 25; it is a reasonable fit since it was so constructed. When inclined north or south, the data should transform as the simulation does. If inclined to the north, the data in Figure 24 at $i_x = 30^\circ$ is reasonably similar to the simulation at 6.5° in the top row of Figure 25. When inclined to the south, however, the simulated radial material in Figure 25 appears above the abscissa with considerable scatter, a poor fit to the data in Figure 24 at $i_x \geq 43^\circ$. Thus, an inclination of 37° seems unlikely. The same exercise for $i_x = 42^\circ$ results in a much better overall agreement between the data and simulation, with the simulated radial points matching the rough positions and scatter of the real ones. At $i_x = 50^\circ$, the simulated views to the north (corresponding to the data viewed close to 43° and 37°) again fail to correctly place the radial material. Specifically, the simulated radial material viewed from the north at 6.5° looks more like echo data at $i = 37^\circ$, whereas it should match up with the view at $i = 43^\circ$. Within its limited predictive capacity, these results favor a true inclination in the vicinity of $i_x = 42^\circ$.

The model can also test whether fitting ellipses to these particular data can provide meaningful results. For each panel in

Figure 25, we fit ellipses through all points, and through only the simulated shell points. Those fits, as well as their ellipticities (b/a), are indicated in each box. The actual ellipticities, from left to right, should be 0.96, 0.99, 1.0, 0.99, and 0.96, with the centroid's y -offset changing roughly as shown in the top row.

In very few cases does either fit give the correct ellipticity, and only in one-third of the cases are the offsets correct. Most fits favor an orientation with the major axis along y' . Considering only the face-on view (middle column) the fits have an error of 3–5% including all data, and 3–14% using only the shell points. In the top two rows, the fits are, on average, good to 5%, with considerable room for additional error. The bottom panel shows highly-eccentric fits with large centroid offsets y_0 . These are “false positives,” since χ^2 has been minimized, but the ellipse does not reproduce the actual cross section. Note however that in all panels, the centers rarely deviate east or west, thus a measured offset in x_0 may be genuine.

Since the uncertainty in a fit is much larger than the change in ellipticity with inclination, it is difficult to perform an anal-

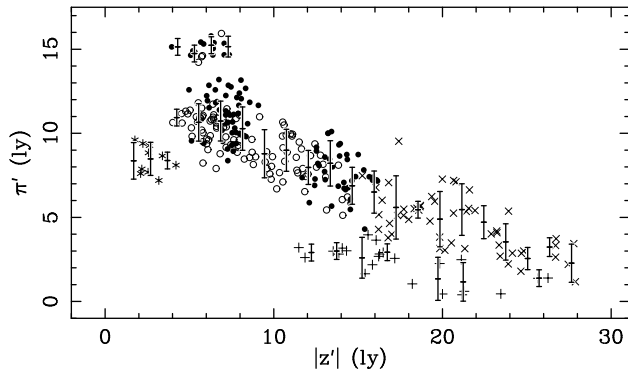


FIG. 26.— Similar to Fig. 19, but for the favored orientation of $i_x = 40^\circ$ and $i_y = 8^\circ$, and showing $|z'|$ along the abscissa. Overplotted is the average radial profile, measured as the average position (and standard deviation) of points binned along $|z'|$.

ysis similar to that in §6.1.3 using ellipse fitting. Nonetheless, we fit a variety of ellipses to the cross-sectional profiles of the CD echoes for $i_x = 40^\circ - 42^\circ$. We consistently find the cross section’s center is shifted east by ~ 1.5 ly. This is consistent with the offset in shell material first noted in §6.1.1. At these inclinations, cross sections also have an ellipticity of $b/a = 0.95 \pm 0.05$, with the major axis aligned toward north. However, as noted above, this is not a robust measurement for this particular dataset.

6.2. A Complete Picture of the CD

The analyses of the previous subsections suggest the CD echoes lie on a surface of rotation about a single axis, with a favored orientation of $i_x = 40^\circ$ and $i_y = 8^\circ$. The radial profile for this orientation is shown in Figure 26. All features are quantitatively very similar to those in Figure 19. Shell points are described by nearly the same linear fits as for $i_x = 37^\circ$ (§6.1.2), while the radial and jet points are fit by slightly-steeper lines. Both the radial profiles and ellipse-fitting suggest that this structure’s axis may be offset to the east of the SN by $\lesssim 1$ ly. This is not a robust result, and since such a small offset will have a negligible effect on the shape of the CD structure, we ignore it for now.

Assuming these data also trace a structure that is symmetric about $z' = 0$, an average radial profile of $\langle \pi' \rangle$ versus $|z'|$ can be constructed by binning the points along the axis. The average radial profile (and standard deviations in each bin) is shown over the data in Figure 26.

The probable CD structure is visualized by revolving this function about the symmetry axis, reflecting it about the equator, and reinclining it to the favored orientation, as shown in Figure 43a–b. Panels (c)–(d) show this complete structure plotted in monotone grey, overlaid with the actual echo points from Figure 15. For these panels, shell points are colored blue, while radial points are red and the jets are green.

This structure is fairly complicated, and can not be described by a simple geometric function. Figure 27 shows a scaled cartoon of the salient features. The “shell” echoes appear to lie along a prolate spheroid with a polar axis of 20 ly and equatorial axes of 11 ly. However, the ends of this spheroid have been extended into tapering cones with opening angles of about 35° (the “radial” echoes), extending from 16 to 28 ly from the SN. Embedded within this prolate structure are narrower, tapering cones (the “jet echoes”) extending from 10–26 ly from the SN, with an opening angle of about

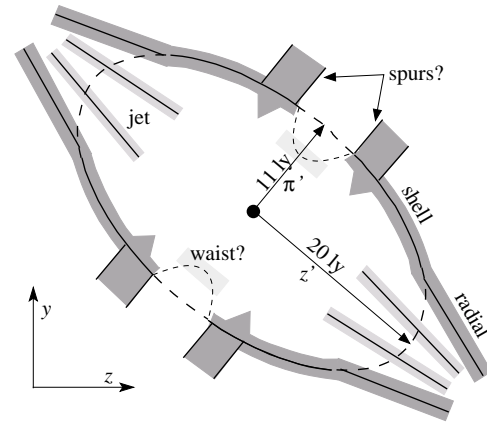


FIG. 27.— Cartoon sketch of the salient structures traced out by the CD model from Fig. 26. This figure is to scale, with the length of the two orientation arrows equal to 10 ly. Solid lines trace the average radial profiles, and the scatter above those profiles is indicated by the solid greyscale regions surrounding each line.

20° , and a maximum radius of 3 ly. Some shell points in Figure 26 are located at $\pi' \sim 15$ ly, and appear disconnected from the rest of the material. These points, which we call the “spurs,” lie along a cylindrical annulus that smoothly encircles the CD.

It is unclear whether the prolate shell is continuous in z' along its equator (dashed equatorial line in Figure 27), since no echoes were observed from that region. Whether this is due to shadowing from material closer to the SN is addressed in §9. The northwestern-WFPC2 echoes are positioned at $z' \sim 4$ ly along the axis, and at roughly 8 ly in radius. This could suggest the prolate shell is pinched at its waist to a smaller radius of 8 ly. However given the very limited spatial sampling of these inner echoes, there is little evidence that they lie on a uniform structure.

At this point in the analysis, evidence that the structure containing these echoes has rotational and mirror symmetries is indirect, and since construction of the probable CD nebula shown in Figure 43 relies on these two assumptions, they merit a brief discussion. First, we recall that Figures 18 and 19 are consistent with surfaces of rotational symmetry. However, rotational symmetry need not imply mirror symmetry, as in the cases of a paraboloid or cone. As we will see in the next two sections, light echoes from material interior to the CD nebula lie on axisymmetric surfaces which do exhibit mirror symmetry. We therefore make the (reasonable) assumption that stellar winds producing symmetric structures at small distances would also produce such structures at larger ones.

In concluding this section, we first comment on the suggestions in §6.1.3 and §6.1.4 that the CD has an inclination of $i_x = 50^\circ$. This is a result of the particular portion of the CD that was imaged in echoes, rather than an intrinsic property of the CD itself. The probable CD is rendered in Figure 28, now shaded by the relative brightness of dust scattering (Sugerman 2003), with assuming uniform density and composition is a function of distance and scattering angle. Panel (a) shows what the entire CD would look like though a complete set of observations well-sampled in time. Panel (b) shows only that portion of the complete CD that could have been observed in our epochs of observation. When viewed from the CD symmetry axis (panel c), we see that brighter echoes form a sharp, circular ridge that could easily be mistaken for delineating the

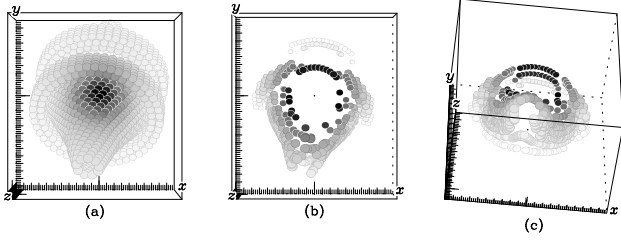


FIG. 28.— Simulated CD showing relative brightness of echoes, where greyscale indicates relative brightness, with darker grey corresponding to brighter echoes. To distinguish faint points, they have been circumscribed with darker grey circles; the reader is reminded that they shade of grey inside these circles indicates brightness. (a) Full CD, viewed face-on. (b) Random points illuminated by the echo parabolae from all epochs. (c) Panel (b) inclined along the CD axis of symmetry.

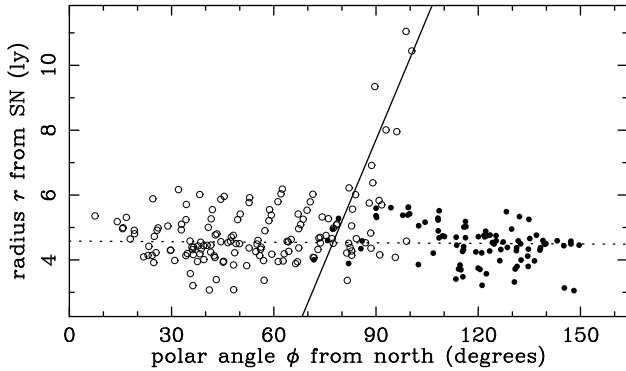


FIG. 29.— Spherical positions of NH echoes (see Fig. 18). NH-north are plotted with open circles, and NH-south with filled circles. The best-fit lines through the horns (solid line) and the other data (dotted line) are indicated.

sharp edge of a narrow cylinder that was seen from $i_x = 50^\circ$ in Figure 20(c).

Finally, if the CD is indeed mirror symmetric, why were echoes not seen from the far half of the nebula (material at $-z'$)? In particular, there is a small portion of material north of the SN interior to the late-time paraboloids (northern points just interior to the large parabola in Figure 15(b)). Figure 28(b) shows that echoes of this small northern portion were very faint due to the large scattering angle, and hence were unlikely to be detected. On the other hand, a segment of the spurs along the closer half of the CD should have created very bright echoes at a radius of $\rho = 7$ ly, roughly from PA $315^\circ - 30^\circ$. Very little signal was detected in this region, which may suggest that the spurs are isolated clumps, rather than a uniform feature.

7. NAPOLEON'S HAT

In contrast to the previous case of the CD echoes, there is much less ambiguity over the possible structures of which the NH echoes are a part. As shown in Figure 15d-f, NH appears to be some surface of revolution with a well-defined axis, such as a prolate ellipsoid, cylinder or frustum. However, it is not immediately clear whether the two horns are part of such a structure. If not, where do they lie, and if so, why has such a limited portion been illuminated? The geometry of the NH echoes will be quantified in the following subsections.

7.1. Geometry of NH Echoes

7.1.1. Spherical Coordinates

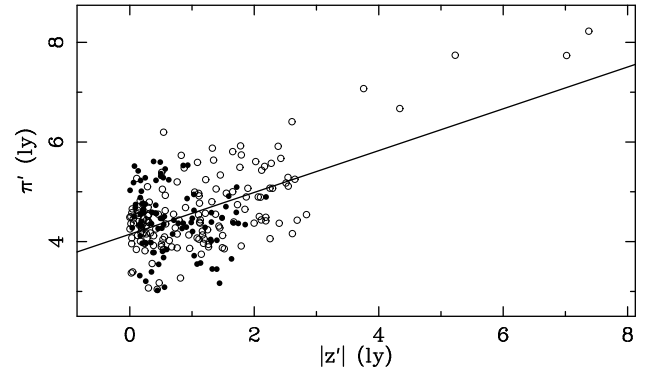


FIG. 30.— Cylindrical positions of NH echoes (see Fig. 19) for the best-fit inclination of 40° south and $6^\circ.5$ east. Symbols are the same as Fig. 29. We assume NH is symmetric about the equator, and plot $|z'|$. The solid line is the best-fit through all points.

As with the CD, we examine the NH echoes in spherical coordinates, shown in Figure 29. The bulk of the echoes fill a horizontal region in ϕ , with points distributed between $\pi' = 3 - 6$ ly, but concentrated around $r = 4 - 5$ ly. In these coordinates, a thick spherical shell with radius $r \sim 4.5$ ly and width $\Delta r = 1$ ly would populate the same region. However, such a structure is unlikely: if the data lay along a spherical shell, echoes in front and south (or behind and north) of the SN should have been observed.

The horns are also inconsistent with a spherical structure, as they are instead located in a highly inclined, almost radial region extending from 6–11 ly from the SN. Rather, the total ensemble of NH echoes can be understood to lie along a cylinder or hourglass. The distributions of points on such structures, viewed in spherical coordinates, populate a horizontal region in ϕ near the equator, while points far from the equator will be highly inclined.

7.1.2. Cylindrical Coordinates

As with the CD echoes, studying points in cylindrical coordinates requires knowing the axis z' . Since the candidate structures for the NH echoes are an hourglass or cylinder (a specialized case of an hourglass), we start by fitting a biconical frustum to all NH echo points, as explained in Appendix B.4. We first restrict the figure's cross section to be circular, and the SN center to lie on the symmetry axis. With these constraints, the best-fit structure (RMS scatter of 0.73 ly) is an hourglass with waist radius of 3.7 ly and opening angle $36 - 39^\circ$, inclined $i_y \sim 40^\circ$ south and $i_x = 2 - 4^\circ$ east of the line of sight. Allowing for an elliptical cross section improves the χ^2 by nearly a factor of two (RMS=0.55 ly), yielding semi-major and minor axes of 4.6 and 3.8 ly, with opening angles at the axes of 28 and 40° , respectively. The major axis is rotated $96^\circ \pm 4^\circ$ east of north, and the axis of the hourglass is oriented with $i_y = 39.5 \pm 0.5$ south and $i_x = 6.5 \pm 0.5$ east of the line of sight. This fit is robust to perturbations in the fitted parameters, including spatial offsets of the waist from the SN.

Figure 30 shows the radial profile of these points as a function of absolute position along the axis (this assumes the data have reflectional symmetry about $z' = 0$). This figure is consistent with an hourglass shape. The best fit through all data is given by $\pi' = (4.13 \pm 0.06) + (0.42 \pm 0.04)|z'|$, which corresponds to a waist radius of 4.1 ly and an opening angle of 46° . While there is a large scatter (RMS=0.5 ly) about this line, note that there are similarly-sloped loci of points $\lesssim 1$ ly

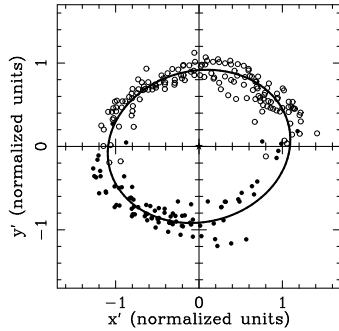


FIG. 31.— Cross-sectional view of NH echoes looking down the best-fit inclination axis. Symbols are the same as Fig. 29. The best-fit ellipse is indicated by the solid line.

above and below it. This is further suggestive of a structure with elliptical cross-section.

The horns extend along the axis from 1–7 ly in front of the SN, and radially 4–8 ly from the axis. They are best-fit by the line $\pi' = (4.4 \pm 0.2) + (0.52 \pm 0.07)z'$, which corresponds to a frustum with inner radius 4.4 ly and an opening angle of 55° . The horns do not appear to be truly linear, but curve to shallower slope at larger z' , as if they lie on a surface of parabolic, rather than linear, profile.

We directly examine the ellipticity of the NH cross section by observing the distribution of points looking down the best-fit axis of inclination (40° south, 64.5° east). Similar to §6.1.4 with the CD, echo positions (x', y') in the plane orthogonal to z' (see Figure 12) are normalized by the average radius π' as a function of z' given by the best-fit line in Figure 30. The resulting distribution, shown in Figure 31, is fit with a 5-parameter ellipse, as described in Appendix B.2. The best-fit ellipse has negligible offset from the origin, and $b/a = 0.82 \pm 0.02$ with the major axis rotated $103^\circ + / - 3^\circ$ east of north. This is consistent with the hourglass fit above, which yielded $b/a = 0.83$ and major-axis rotations of $92\text{--}101^\circ$.

We use these values to remove the ellipticity from the radial profile, yielding the distribution shown in Figure 32. As expected, the horns have shifted to smaller radii, and the scatter between the rest of the NH points has diminished. Also shown is the average radial profile of the NH echoes, generated by binning the points along the inclination axis and computing the average radius about that value. The implied structure appears cylindrical with a semi-minor axis of 4 ly up to $|z'| = 1.5$ ly, after which it has a fairly constant slope. The best-fit line through the entire profile (solid line) is given by $\pi' = (3.53 \pm 0.23) + (0.52 \pm 0.06)z'$, corresponding to an hourglass with semi-major and minor waist axes of 4.4 and 3.5 ly, and an opening angle near 54° . Excluding the horns, the fit is considerably shallower (dotted line), suggesting an opening angle of 36° , and axes of 4.8 and 3.8 ly. Despite the ambiguity in functional form, these fits are all consistent with the values found by the hourglass fitting.

7.1.3. What are the horns?

If the horns are part of the same hourglass-like structure containing the rest of the NH echoes, why was such a limited section of the much larger surface illuminated? Assume the horns lie along the solid line in Figure 32. This line can be revolved about the z' axis, then reinclined from the line of sight by the best-fit NH orientation to generate a complete frustum, as shown in Figure 33a. As in Figure 28, greyscale indicates

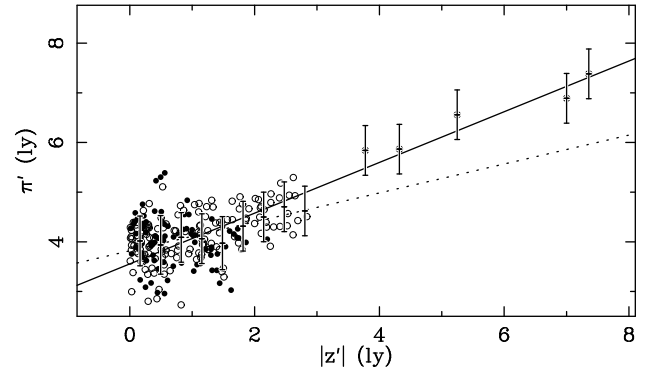


FIG. 32.— Data from Fig. 30, with the ellipticity from Fig. 31 removed. Overplotted is the average radial profile, measured in bins along $|z'|$. Single points have fixed errors. The best-fit line through the complete profile is indicated by a solid line, and the best-fit through points excluding the horns ($|z'| < 3$ ly) by the dotted line.

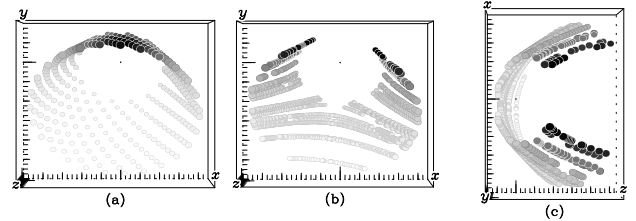


FIG. 33.— As Fig. 28 but showing the frustum containing the horns. Darker shading indicates increased surface brightness of an echo. (a) The complete frustum as revealed through a complete, regularly sampled set of echoes. Random points along the intersection of the frustum with echo parabolae from our observations are shown in panels (b) (face-on) and (c) (from the top). Greyscale is normalized to the brightest and faintest points plotted, thus shadings differ between panels (a) and (b)–(c).

relative brightness of echoes based on their scattering angle and distance from the SN. Points along the northern limb are the brightest, since the scattering angle is lowest.

Random points on this frustum along echo paraboloids observed in our data are shown in panels (b)–(c). The northern limb was never illuminated by echoes as it lies inside the earliest paraboloid. The earliest intersection occurred just south of this limb, and over time, increasingly-southern slices were illuminated, becoming fainter with increasing epoch. The brightest echoes came from the first few epochs, appearing as linear, radial features at roughly constant north-south position. Furthermore, at the earliest epochs, the illuminated material is oriented close to the line of sight, thus these echoes appeared even brighter due to a limb-brightening effect. Thus the limited portion of this structure that was illuminated as “the horns” is consistent with these points lying on the same hourglass as the rest of the NH material.

7.2. A Complete Picture of the NH Structure

The probable structure containing the NH echoes is an hourglass, the waist of which has an ellipticity of $b/a = 0.82$, with a semi-major axis of ~ 4.9 ly rotated about 102° east of north. Bootstrap analyses of these fits yield errors of about 3% for each parameter. If the horns lie on a surface with similar eccentricity, the hourglass flares to a semi-minor axis of ~ 7 ly about 7 ly from the SN along the axis of symmetry. The entire structure is oriented at $i_y = 40^\circ$ south and $i_x = 7^\circ$ east of the line of sight. To visualize this, the average radial profile from Figure 32 is reflected about the equator and revolved

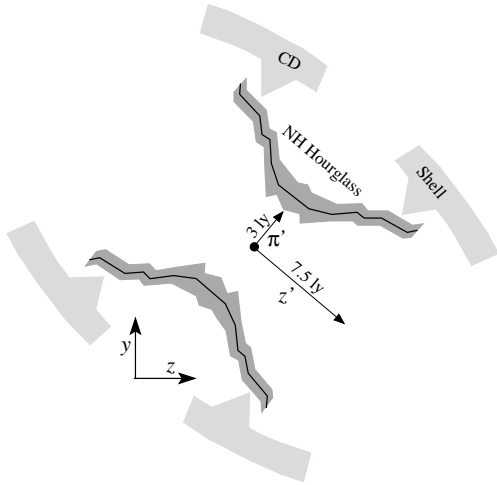


FIG. 34.— As Fig. 27, but for the NH echoes, with the orientation arrows measuring 4 ly. The solid line traces the radial profile from Figure 32, and the width of the greyscale region traces the scatter of points about that profile.

around the axis, then reinclined from the line of sight by the inclinations just given. The resulting distribution is rendered in Figure 43e–h.

A much larger portion of this nebula was sampled by echoes than was actually observed. This was discussed in some detail above within the context of the horns, from which we concluded that the majority of the signal from the near half of the hourglass was very faint due to the larger distance and scattering angle of that material compared to the dust at the waist. The same argument applies to the far half of the hourglass, explaining why no discrete signal was observed from the northern parts of the structure at later times.

A number of small-scale features not represented in this figure are better discussed in the cartoon sketch of the NH echoes shown in Figure 34, where grey-shading represents the scatter in points about the average profile. In the first two bins ($|z'| < 0.5$ ly) in Figure 32, material extends beyond the average scatter to smaller and larger radii of $\pi' \lesssim 3$ and $\pi' \gtrsim 4.5$ ly. Furthermore, over one-third of the NH points lie within these first bins, which implies these data trace out an equatorial enhancement in both density and radial position. This is shown in Figure 34 as small spurs pointing toward and away from the SN in the equatorial plane. A similar, but less significant, inward-pointing feature is seen roughly 1.5 ly along the axis. CKH95 reported a small set of echoes within 3 ly of the SN that are coincident with the ER plane, which they interpreted as evidence for an extended circumstellar equatorial disk. The NH equatorial echoes appear to extend this disk to a radius of 5 ly, with a thickness of $\gtrsim 0.75$ ly.

7.3. Comparison with Previous Work

As NH was the subject of interest in the early 1990's, we compare the newly revealed material with previous interpretations. Wampler et al. (1990a) first reported the discovery of the “Napoleon’s Hat” echo in narrow-band [O III] and [N II] imaging as diffuse nebulosity, which blended smoothly into background filamentary structure that defines the eastern and western rims of a “V”-shaped “dark bay” south of the SN (see Fig. 6). Wampler et al. (1990b) further noted that the larger, arcmin-radius echoes from interstellar dust (e.g., Xu et al. 1995) fade when crossing over this bay. A natural interpretation was that this bay is an evacuated region, and

no light echoes were seen there because of its particularly low density. As the background filaments loop around the SN, they proposed that the progenitor’s MS winds evacuated the bay, and its V-shape can be attributed to the proper motion of the progenitor through the ISM.

Wang & Wampler (1992) reanalyzed their ground-based data and were able to trace the NH echoes as early as day 890, but the echoes had faded by day 1650. An interpretation that these echoes lie along a disk coplanar to the inner ER was disfavored, since the flux had the wrong distribution and shape for a solid, dusty disk, and since the echoes moved very little in time. Rather, Wang & Wampler (1992) and Wang, Dyson, & Kahn (1993) considered these structures consistent with a parabolic bow-shock to the north of the SN, which could be further interpreted as the terminal edge of the dark bay evacuated by the MS progenitor.

Given the limited data at hand, and considerable confusion from the background filaments in the LMC, the bow-shock model was an attractive scenario. However, the current analysis has revealed a much more extensive volume of material illuminated by the SN, the 3-D positions of which are inconsistent with a bow shock. Rather, these data imply that the disfavored interpretation of Wang & Wampler (1992)—that NH is in the equatorial plane—was correct.

Suppose the star does have a large proper motion, and that the dark bay is the region evacuated by the MS wind. Whatever the star’s proper motion through the ISM, it must have moved at least 25 ly north during its lifetime to create this bay and end at its observed position. The CD echoes from this region have illuminated a prolate structure that ends at roughly the same position on the sky as the center of this bay. This is also inconsistent with the bow-shock model. Most likely, the filamentary nebula is not associated with the SN, and we propose that the correlation between the position of the NH echoes and the “V”-shaped nebula is a positional coincidence.

8. CIRCUMSTELLAR ECHOES

As noted in §1, the inner $3''$ surrounding SN 1987A have been previously studied by CKH95 using a subset of the data presented here. Employing PSF-subtraction and rudimentary PSF-matching, the authors detected echoes along a bipolar nebula with an hourglass shape, in the sense that a narrowed waist separates two open-ended lobes. A smaller set of echoes coplanar with the ER were identified as evidence of an extended circumstellar disk.

The current analysis differs from CKH95 in a number of ways. In the previous work, the authors paid particular attention to the inner few arcsec around the SN, and their reduction may have less noise from PSF-subtractions of the SN and stars 2 and 3 than from our automated reduction pipeline (§4.3.3). The general PSF-matching algorithm has been greatly improved since 1995, and we have implemented a number of custom modifications to minimize difference-residuals and to increase the detection threshold of echo signal. Since we were interested in echoes from a much larger range of radii, we also have increased the spatial extent over which circumstellar (CS) echoes have been sought. Finally, we used a very different technique for identifying the positions of echoes. Sufficient differences exist between the two methods that the current data merit an independent analysis.

8.1. Geometry of CS Echoes

An exploration of the geometry of these echoes (summarized in §8.2) is facilitated by the work of CKH95, which es-

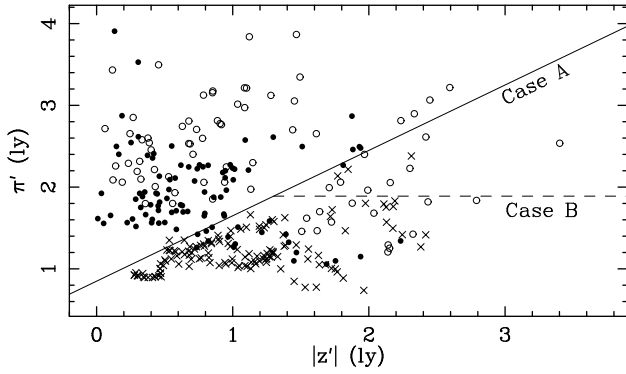


FIG. 35.— Cylindrical profile of π' versus $|z'|$ for the CS echoes inclined by $i_x = 45^\circ$ and $i_y = 8^\circ$. Symbols correspond to points in Fig. 15g–i, with closed and open circles denoting cyan and yellow extended flux points, and \times marking the red hourglass. Points below the solid line are potential members of the CS hourglass, and comprise distribution “A,” while those also under the dashed line are distribution “B” (§8.1.1).

established the cylindrical symmetry axis of the double-lobed CS hourglass. We cannot immediately explore such a feature in our data since, as noted in §5.4.3, it is unclear which extended-flux echoes are associated with this hourglass. However, CKH95 reported a small number of echoes along this southern lobe, and we can use their data to help disentangle our points.

8.1.1. Geometry in Cylindrical Coordinates

We begin by fitting a biconical hourglass to the CKH95 data, using the χ^2 minimization described in Appendix B.4. Assuming the frusta have circular cross-sections, the data are best-fit by a structure inclined by $i_x = 45^\circ$ south and $i_y = 8^\circ$ east of the line of sight. This compares favorably to the orientation reported in CKH95 using a minimization-of-scatter estimator, but our rotation i_y is larger than theirs ($3^\circ \pm 5^\circ$). We adopt this as the preliminary orientation axis, and transform all echo points into cylindrical coordinates (see Figure 12) about this axis. Assuming the structures are symmetric about the equator ($z' = 0$), we plot in Figure 35 the radial profile of π' as a function of absolute distance $|z'|$ along the axis. The region containing northern-hourglass echoes (marked by \times) includes some extended-flux material, which may correspond to additional points along the northern and southern lobes.

The northern-hourglass echoes in Figure 35 can be considered as lying along one of two regions. Case “A” is roughly delimited as points below the solid line, which follows the outer edge of the echoes at any given point along the axis. When binned, the northern-hourglass points follow a somewhat curved trajectory that approaches constant radius with increasing $|z'|$. Such a region is approximately bounded by the dashed horizontal line, which we denote case “B.” While a few extended-flux points straddle the solid boundary, the majority are located above it, suggesting that points above the solid line are part of a different structure, and only points below it can be part of the hourglass. We proceed by testing which distribution of points is most-likely on such a structure.

Biconical hourglasses are fit to the case A and B distributions. Case A points are consistent with an hourglass inclined 41° – 42° south and 10° – 13° east of the line of sight. The fit to distribution B is similar, with an inclination of 40° – 41° south, 12° – 15° east. This fit has a χ^2 nearly three times

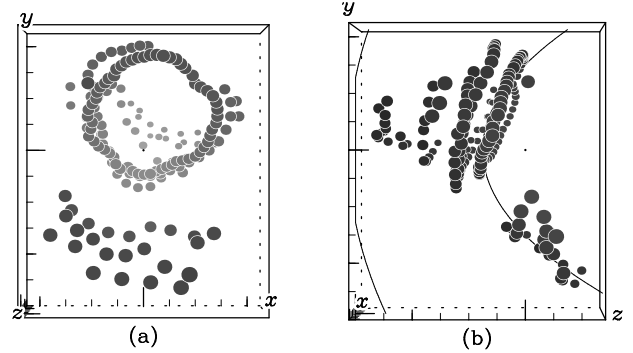


FIG. 36.— Same as Fig. 43g–h, but showing only those CS points believed to lie along the hourglass (the case B distribution from Fig. 35).

TABLE 2
OBSERVED GEOMETRIC PARAMETERS OF THE ER

Parameter	Unit	Value
Centroid Offset	(mas W)	18.7 ± 0.4
Centroid Offset	(mas S)	2.0 ± 0.7
Inclination Angle	($^\circ$)	43.0 ± 0.1
Semi-Major Axis	($''$)	0.820 ± 0.005
Semi-Minor Axis	($''$)	0.600 ± 0.005
P.A. of Major Axis	($^\circ$ E of N)	81.1 ± 0.8

smaller than for case A, while there are only 16 fewer points, suggesting that the points above the dashed line in Figure 35 are not directly part of the hourglass structure. Accordingly, we choose the B distribution as the probable set of hourglass points. These points are rendered in Figure 36. As expected from the earliest echo parabola, only a small arc along the southernmost limb of the southern lobe is present.

The best-fit hourglass to these data is inclined at (i_x, i_y) of $(-40.7^\circ \pm 0.2^\circ, 14.7^\circ \pm 0.7^\circ)$, with a westward shift of 0.04 ± 0.01 ly. The waist has an ellipticity $b/a = 0.94 \pm 0.03$ and semi-major axis 1.01 ± 0.2 ly, rotated $10^\circ \pm 1^\circ$ north of east. As noted in Appendix B, these errors are the scatter in parameters fit to random subsets of the data.

8.1.2. Constraints from the Equatorial Ring

If we assume the three-ring nebula lies symmetrically about the hourglass, then the positions of the rings on the sky should intersect, or be symmetrically bounded by, the hourglass. These rings are commonly assumed to be planar circles, appearing elliptical due to their inclination. As such, their observed positions should be reproduced by simple geometric figures viewed in the hourglass frame of reference. Unlike the ORs, for which only limited velocity data exists, the velocity shear across the ER indicates it is a planar structure (Crofts & Heathcote 1991, 2000), and its projected geometry is very-well constrained (see below). The ER is therefore the best candidate for this exercise.

Sugerman *et al.* (2002) measured the ER geometry by fitting ellipses to a high-resolution WFPC2 image. The reader is referred to that paper for a thorough description of the method. Briefly, the ER was divided into bins of equal arc-length, and the flux in each bin was normalized to the second brightest pixel value. Ellipses were then fit to the brightest $N\%$ of the pixels in each bin, where N varied from 50% to 95%, and the resulting parameters averaged to give final

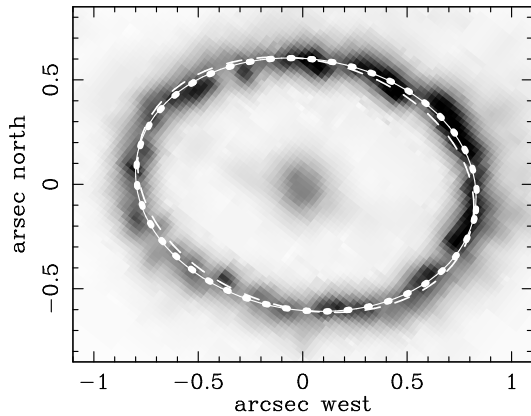


FIG. 37.— Drizzle-reconstructed (0.23 pix^{-1}) WFPC2 F656N image of the ER from Sugerman et al. (2002). The best fit ellipse to the observed ER (Table 2) is indicated with the thick dotted line. The projected position of an ellipse oriented by the PYR triplet ($-16^\circ, -14^\circ, 41^\circ$) is shown with a thin dashed line, corresponding to the best fit to the hourglass from §8.1.1. The projected view of the ellipse that best-matches the ER from §8.1.2 oriented by ($-9^\circ, -8^\circ, 41^\circ$) is indicated by the thin solid line, which nearly exactly matches the thick dotted line.

values. However, their choice of fitting algorithm was not as robust as that described in Appendix B.2. We reproduced their fit by substituting our improved minimization algorithm, the results of which are given in Table 2 and drawn with heavy dots in Figure 37.

If the ER is a planar ellipse, then viewed at the hourglass orientation, it should overlap closely with our best-fit. For all the orientations listed in the previous section, no combination of ellipse parameters (offsets, axes and major-axis rotation) can fully reproduce the observed geometry. The best fit achieved using those orientations is shown with a thin dashed line, and has an average deviation of 18 mas. This error is more than double the uncertainty of the ER axes, and is as large as its centroid offset, thus the orientation provided by the hourglass fit is not ideal.

Allowing the orientation of the ellipse plane to vary as well, the absolute best fit to the observed ER deviates by only 3 mas. Shown by the thin, solid line, this ellipse has an orientation of $i_x = 41^\circ$ south and $i_y = 8^\circ$ east, and with the major axis rotated 9° north of east. The ellipse has a major axis 0.82 , $b/a = 0.98$, and the centroid is shifted 19 mas west of the SN. A circle at this same orientation fits the ER with three-times larger χ^2 . Provided the ER is connected to the CS hourglass, this is the first direct measurement of the ER’s orientation and deprojected geometry.

8.1.3. Geometry in Cylindrical Coordinates II

Why do the hourglass and ER fits yield values of i_y discrepant by over 6° ? The hourglass is well-sampled only along the southern edge of the northern lobe, otherwise, the data are sparsely sampled. This distribution is sufficient to constrain the north-south inclination i_x , but allows great freedom in east-west rotations. We test the newly-proposed orientation by repeating the hourglass fit, this time holding i_y fixed at 8° .

The result is an hourglass inclined $i_x = 41.2^\circ \pm 0.2^\circ$ and shifted 0.1 ± 0.02 ly west; a waist with semi-major axis 1.04 ± 0.02 ly rotated $9^\circ \pm 1^\circ$ north of east; and $b/a = 0.94 \pm 0.01$. The same caveat for the errors from §8.1.1 applies. The frusta have a half-opening angle of $12^\circ \pm 1^\circ$, which is close to that found by CKH95. This is very similar to the orientation sug-

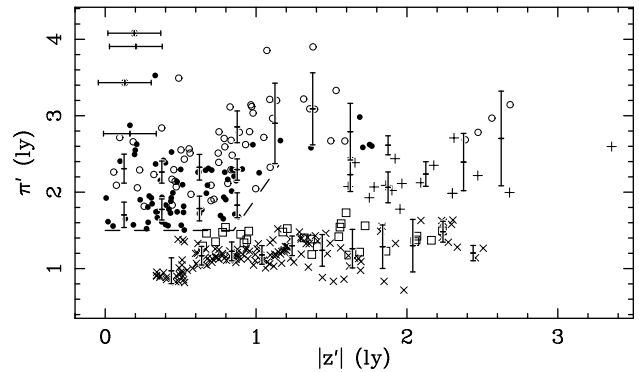


FIG. 38.— Same as Fig. 35, but with data inclined by the favored CS orientation of $i_x = 41^\circ$ and $i_y = 8^\circ$ and an ellipticity of 0.94 removed from the radii. Circles that are now considered part of the hourglass are marked by open squares, and the case-A only points (Fig. 35) are marked by pluses. The average radial profiles to each structure are overplotted. The dashed line shows the inner edge of the belt, used in §8.3. Note that there are many binned averages in this plot, which are discussed in the §8.2.

gested by the ER fit, and therefore we adopt it for the CS material. Note that fitting an hourglass confirms the findings in §8.1.2 and by Sugerman et al. (2002) that this nebula is offset slightly west of the SN.

The cylindrical-radial profile for the data oriented about this new axis is shown in Figure 38. An ellipticity of $b/a = 0.94$ has also been removed from each radius, based on its position angle along the elliptical hourglass fit given above. Extended flux points that are now associated with the hourglass are plotted as squares, and the points belonging only to the case A distribution are shown with plus marks. A large subset of the extended-flux echoes (circles) are concentrated within 1 ly of the equatorial plane ($z' = 0$), between 1.5–4 ly from the SN, and appear to form a thick equatorial waist or belt circumscribing the hourglass. As in the previous two sections, we measure the average radial profile of these points in bins along $|z'|$. There is much structure to these data, which requires the fitting of six profiles. These, and their interpretation, are discussed in the next section.

8.2. A complete picture of the CS nebula

Surrounding SN 1987A is a complex CS nebula, inclined at $i_x = 41^\circ$ south and $i_y = 8^\circ$ east of the line of sight, translated $\lesssim 0.1$ ly to the west of the SN, with an elliptical cross-section ($b/a \simeq 0.94$) whose semi-major axis is rotated 9° clockwise from east. We visualize this nebula by reflecting each radial profile about the equator, revolving it around the cylindrical axis, then reinclining it by the best-fit orientation. The ellipticity removed in making Figure 38 was reintroduced when revolving the profiles about the cylindrical axis. The result, rendered in Figure 43*i–j*, shows the probable structure of the CS material. Colors are discussed below. The next two panels (*k–l*) compare the complete structure in grey to the observed echoes. Here, colors are similar to Figure 15*g–i*, only now all hourglass points are colored red, and the Case-A only points (Fig. 35) are colored green. For completeness, we show only the CS hourglass in panels (*m*)–(*p*).

Figure 39 shows a scaled cartoon of the relevant CS features. In the following subsections, we discuss each feature based on its radial profile and three-dimensional shape.

8.2.1. The CS Hourglass

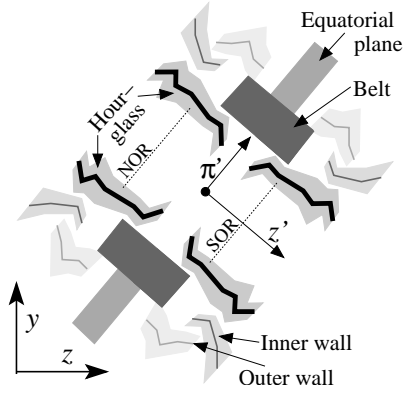


FIG. 39.— As Fig. 27, but for the CS echoes, with the orientation arrows measuring 2 ly. The expected positions of the ORs are indicated by thin dotted lines (§8.3).

The innermost radial structure is the hourglass, shaded red in Figure 43*i–j* and shown by itself in panels (*m*)–(*n*). In Figure 38, these are the crosses (\times) and squares within about $\pi' \leq 1.5$ ly. This is fairly cylindrical, with a semi-minor axis of 1.2 ly, tapering close to the equator and opening just slightly at large z' . The profile is well-described by a line of slope $\Delta\pi'/\Delta z' = 0.14$ and zeropoint $\pi' = 1.02$, suggesting an opening angle of the wall of only 8° . A very small number of points suggest that it also tapers around $z' = 1.5$ – 2 ly, but this feature is marginal at best.

A number of small-scale features are worth noting in the hourglass. The northern-lobe points extend to a relative maximum in radius ($\pi' \sim 1.5$ ly) at $|z'| = 1.4$ ly, tapering slightly in radius on either side; a similar feature is also seen around $|z'| = 0.9$ ly. In Figure 38, many of the extended-flux points lie just outside the average position of the hourglass. Since most of these points are part of the southern lobe, this could suggest the southern lobe is wider than its northern counterpart. A more likely interpretation is that many of the southern-lobe points represent dust just outside the densest part of the hourglass, which was illuminated prior to our earliest epoch (see Fig. 43*p*).

Consistent with CKH95, we do not see evidence for a “capping surface” to this structure, as would be expected from a bipolar peanut-like nebula, the result of many interacting-winds formation models. To distinguish this hourglass from the larger one containing the NH echoes, we refer to each by their association—i.e., the latter is the “NH hourglass.”

As in previous sections, we address why only a limited amount of this complete hourglass structure was illuminated by echoes. Referring to Figure 43(*p*), only the southernmost portion of the near (or south) half of the hourglass was probed by the earliest echo. While the greater majority of the far (or northern) half of the CS hourglass lies inside the earliest and latest echo parabolae, the particular sampling of our observations probed the northern edge only at the earliest epochs. A comparison of this panel with Figure 36(*b*) shows that we have detected roughly all the material that could have been observed.

8.2.2. The Equatorial Plane and Belt

Immediately surrounding the CS hourglass is the thick waist of extended high-surface brightness, which we call the “belt,” and have colored green in Figure 43*i–j*. It extends ± 1 ly along the z' axis, and from 1.5 to 2.5 ly in radius. To better

represent the extent of this material, two profiles have been fit in Figure 38, binned both in radius and along the axis. Beyond the outer radius of this belt, echoes lie fairly well constrained to the equator, tracing a thinner (0.5 ly thickness in z') but extended equatorial plane to an outer radius of $\pi' = 4$ ly. This feature has been colored blue. The belt does not appear to taper smoothly into the thinner equatorial plane, but rather has a fairly sharp transition at its outer boundary.

8.2.3. The Inner and Outer Walls

The rest of the CS material lies along one of two “walls.” In Figure 38, the innermost of these is marked mostly by pluses at $|z'| > 1.5$ ly, while the outer wall is marked with circles from $0.9 \leq |z'| \leq 1.9$ ly. The inner wall extends 1.5 to 2.6 ly along the axis, and may be considered to join with the hourglass around $|z'| = 1.5$ ly. The profile is positively sloped, which translates into a wide cone with half-opening angle of 40° . This may simply trace a decreasing dust-density profile extending out from the sharp peak of the hourglass. A single datum is located at $|z'| = 3.4$ ly, and it is unclear whether this can be trusted as a real feature.

The outer wall bridges the belt and the inner wall at radii between 2.6 and 3.4–4.0 ly. These have been colored cyan and gold in Figure 43*i–j*. Unlike the inner wall, the average profile is concave, reaching its maximum radius roughly 1.4 ly along the axis. This corresponds to a local maximum seen along the hourglass, and to the expected positions of the ORs (Crotts & Heathcote 2000). Noting the conspicuous lack of echo signal between the hourglass and outer wall at this position, we question whether this is indicative of episodic mass loss, and if the OR formation mechanism is somehow related.

8.3. The Geometry of the Outer Rings

While great attention has been placed on the geometry of the ER (Jakobsen *et al.* 1991; Plait *et al.* 1995; Burrows *et al.* 1995), relatively little work exists on the ORs. In §8.1.2 the ER was used as a constraint to the geometry of the CS nebula. Now that a three-dimensional map of the nebula exists, this problem can be inverted to ask instead how the echoes can constrain the 3-D geometry of the ORs.

Burrows *et al.* (1995) reported the NOR is well fit by an ellipse with $b/a = 0.678$, and a semi-major axis of $1''.77$ oriented at P.A. $70^\circ.7$, while the SOR is fit by an ellipse with $b/a = 0.513$, and semi-major axis $1''.84$ oriented at P.A. 90° . Assuming both rings to be circular in their reference frames, they are inclined roughly 43° and 31° to the line of sight, respectively. Accordingly, if the SOR has the same inclination as the ER and NOR, it cannot have a circular shape. They also note that the segment connecting the centers of both ORs misses the SN and ER centroid by $\sim 0''.4$. Crotts & Heathcote (2000) use these orientations to fit a kinematic model to the ring velocities as measured in STIS and ground-based echelle spectra. This model suggests the NOR and SOR are located 1.32 and 1.04–1.24 ly (depending on whether one forces the SOR to be circular or not) from the SN along the inclination axis.

Figure 40 shows the complete three-ring nebula from the same WFPC2 image used to study the ER in §8.1.2. We measured the positions of each OR at various P.A.s by performing the same radial-profile fitting as that used in measuring echoes. With the positions of the rings on the sky known to better than one pixel ($0''.023$), the only unknown for each point is its line-of-sight distance from the SN. If one assumes the ring lies on or about the CS hourglass, each z position can

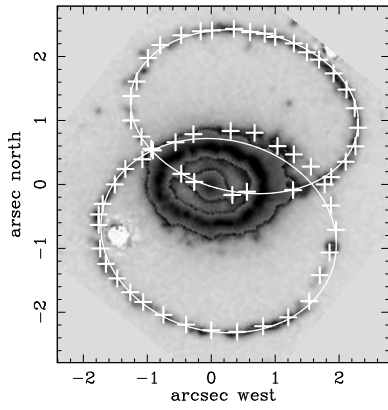


FIG. 40.— The full WFPC2 image of the three rings, from which Fig. 37 is taken. To increase the display range, brighter pixels are displayed with a separate color stretch. Heavy crosses show the positions of the rings as measured through radial profiles. The best-fit planar ellipses to these points are traced by thin, solid lines.

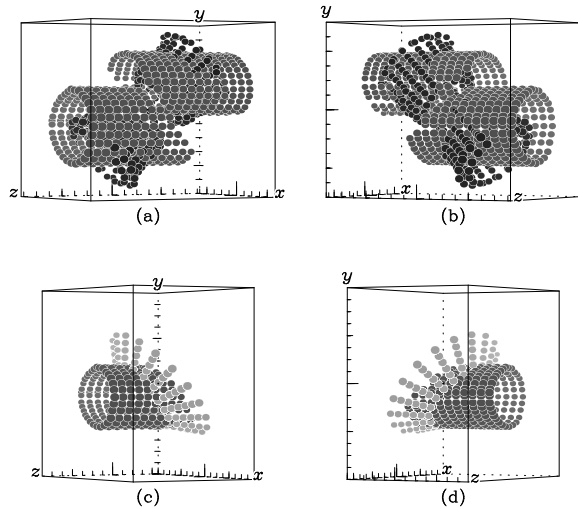


FIG. 41.— Rendered points showing the determination of OR positions. The NOR and SOR must lie along the upper (opening away from the observer) and lower (opening toward the observer) medium-grey tubes, respectively. One possible location of the rings could be the intersection of these tubes with the CS hourglass, shown in panels (a)–(b). Panels (c)–(d) show the inner edge of the belt (light grey), which is a good fit to the SOR.

be determined as the intersection of the hourglass with the “tube” of all possible z positions for a given point on the ring.

Figures 41a–b show the results of this exercise. The red hourglass from Figure 43 is shown in dark grey, while lighter dots trace all possible z values for each point along the NOR (upper tube) and SOR (lower tube). The hourglass intersects both tubes at many points, but fails to do so along the western side of the NOR and the entire northern half of the SOR. If we instead consider the intersection of each tube with the outer edge of the hourglass (using the radial-profile error bars in Fig. 38), the NOR is well fit at all P.A.s by points located at $z' = 1.37 \pm 0.05$, while the SOR still fails.

We consider two possibilities for the SOR. First, were the southern lobe oriented with $i_y \sim 0^\circ$, it would cleanly intersect the SOR tube. It is only by construction that the hourglass has a single axis of symmetry, unfortunately too little of the southern lobe was illuminated by echoes to test for such a departure. Second, rather than simply lie on or around the hourglass, the SOR may result from its intersection with an-

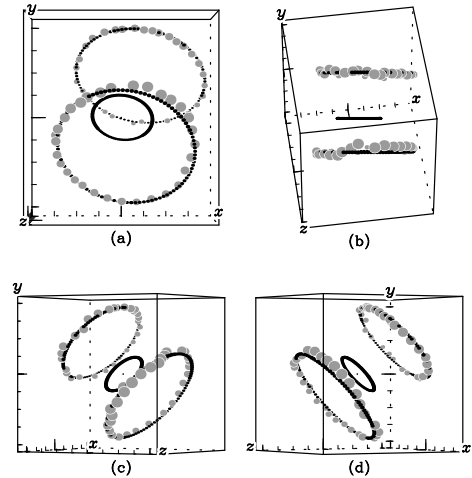


FIG. 42.— Probable positions of the ORs (grey) and the planar, elliptical fits (black) to each ring, viewed (a) face-on, (b) 60° east, (c) 60° west, and (d) orthogonal to the inclination axis.

TABLE 3
BEST-FIT ELLIPSES TO THE CS RINGS

Ring	x'_0 (ly west)	y'_0 (ly north)	z'_0 (ly)	a (ly)	b (ly)	ϕ ($^\circ$)
ER	0.015	0.0	0.0	0.647	0.98	81.1
NOR	0.26	0.04	-1.36	1.42	0.94	70.5
SOR	0.19	0.06	1.00	1.59	0.92	-1.1

other structure. In Figure 38, the dashed line traces a sharp, inner edge to the belt, which nearly intersects the southern lobe of the hourglass (traced with squares). When the diagonal segment of this boundary is revolved around the hourglass axis (light-grey in Fig. 41c–d), it intersects the SOR tube continuously at all P.A.s at a distance of $z' = 1.0 \pm 0.05$ ly from the SN. We question whether the SOR is some sort of density enhancement resulting from the interaction between the hourglass flow and the inner edge of the belt.

This same belt material makes a poor fit to the NOR, and we can not readily identify a similar intersection of observed structures. However, echoes from material behind the SN could have been missed for a variety of reasons, including source confusion and small scattering efficiency.

The 3-D positions of the ORs are rendered in Figure 42, and appear reasonably planar. We approximate both rings as planar ellipses (Appendix B.2), fit to each distribution of points viewed along the CS inclination axis. The resulting parameters are listed in Table 3, where (x'_0, y'_0) are the centroid offsets from the axis, z'_0 is the distance to the SN along the axis, (a, b) are the semi-major and minor axes, and ϕ is the P.A. of the major axis from north. For completeness, the parameters for the ER (§8.1.2) are also listed.

These fits are indicated in black in Figure 42, and by thin white lines in Figure 40. The approximation to the NOR is quite good, but the SOR ellipse fails to intersect the points that pass just north and west of the ER. This is not surprising, since no single ellipse can fully reproduce the observed shape of the SOR unless it is non-planar. Since these ellipses are consistent with both the CS structure and observed three ring nebula, we have used them in the echo renderings throughout this work.

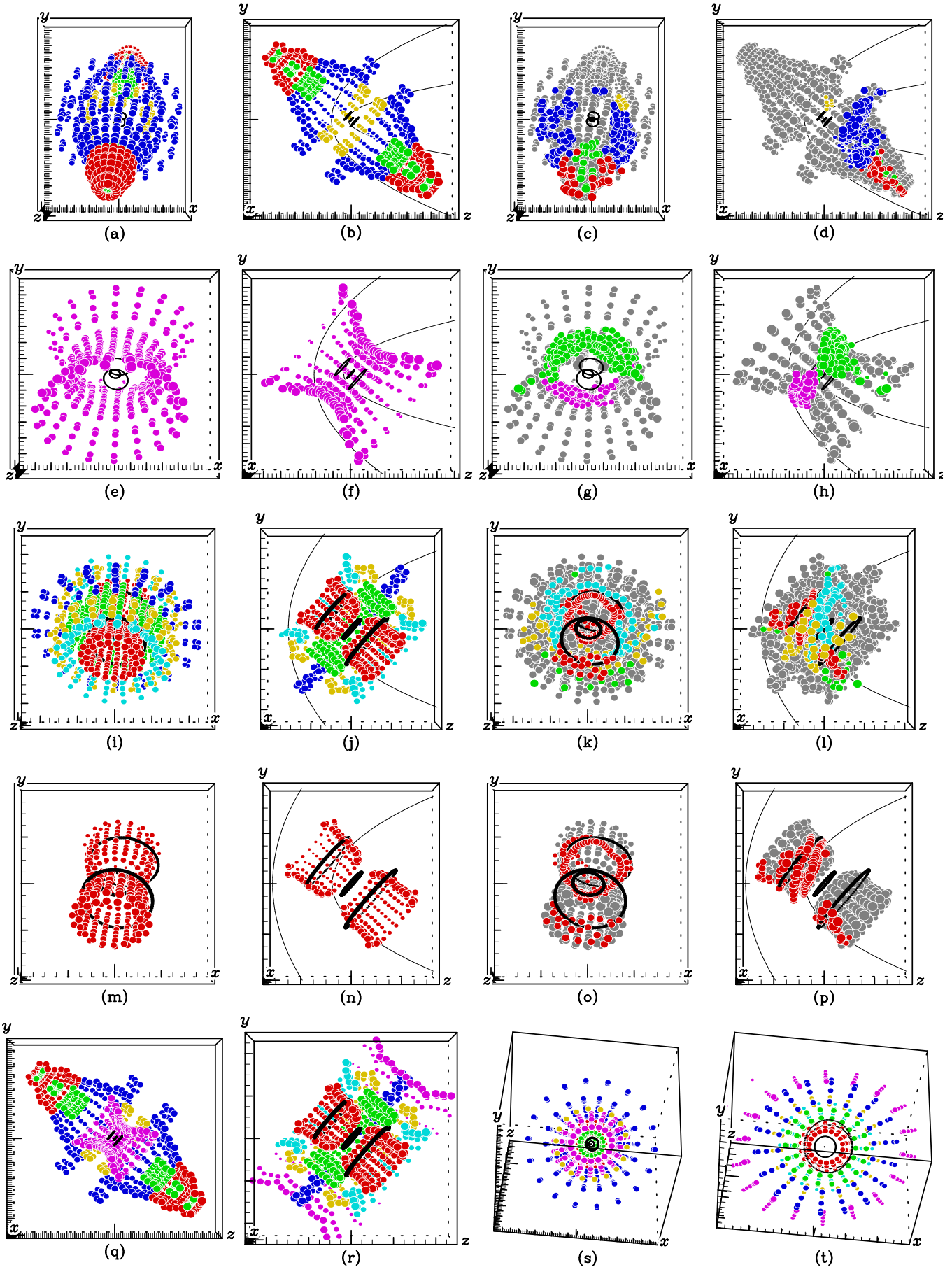


FIG. 43.— Rendered views of the probable structures containing the observed echoes. *Top Row:* The CD nebula. *Second Row:* The NH nebula. *Third Row:* The CS nebula. *Fourth Row:* The CS hourglass. For these top four rows — *Left column:* the face-on view of the complete structure; *Second column:* the western half, viewed from the east, showing a clear view of the interior; *Right columns:* face-on and side views of the complete structures in monotone grey, overlaid with actual echo points from Figure 15. For the bottom row — (q) The western halves of the CD and NH, and (r) NH and CS nebulae, viewed from the east. (s) The northern halves of the CD and NH, and (t) the NH and CS nebulae, viewed along the inclination axes from the south. See text for colors.

9. DENSITY AND MASS OF THE CSE

9.1. A complete picture of the CSE of SN 1987A

The probable geometry of the structures containing all echoes within $25''$ of SN 1987A are rendered in color in Figure 43, and summarized in Table 4. The final column gives the approximate total volume of the structure containing each echo, found by integrating the radial profiles in Figures 26, 32, and 38 along, and revolved 2π about, the respective inclination axes.

The east/west and north/south inclinations are quite consistent, suggesting all circumstellar material shares a common inclination of $i_x = 40^\circ$ south and $i_y = 8^\circ$ west. The inner two structures (CS and NH) both have elliptical cross sections (see Figure 43s–t), although the ellipticities and orientations differ. However, it is unclear whether this particular result is significant. As noted in Appendix B, χ^2 minimization does not readily allow for errors in multiple dimensions, yet the measured echo positions have finite width and depth. Rather than attempt much more complicated (and error-prone) techniques, such as iteratively reweighted least squares with robust estimators, we give these results with the understanding that the CS and NH ellipticities are most-likely bounded between the values reported for the two structures.

The CS gas is nested neatly within the NH material. The extended CS equatorial plane connects to the waist of the NH hourglass, forming a continuous structure from 1.5 to 5 ly from the SN. Tracing NH out from the waist, there are inward-pointing spurs above and below this equatorial plane that connect to the outer CS wall, which itself connects to the belt. The CS belt, equatorial plane, outer wall, and the waist of NH are therefore consistent with a single, uniform thick waist, extending inward to the CS hourglass. This is shown in Figure 43r.

The outer edges of the NH hourglass almost reach the inner spur of the CD shell, and indeed the echoes as viewed on the sky do connect at early times (Fig. 10). As shown in Figure 43q, no material was illuminated along the equatorial plane exterior to NH. Unless this region was shadowed from the SN by material at smaller radii (§9.2.1), there is no higher density gas outside the waist of NH, suggesting the NH hourglass is the pinched waist of the CD.

The one caveat to this argument is that just above the equatorial plane and outside the NH hourglass are the northwestern WFPC2 echoes, whose relationship to the rest of the CD material was unclear in §6. Shown as gold in Figure 43m, these would have formed a cylindrical band outside the waist of the NH hourglass. We do not believe these are image artifacts, nor part of a distinct, uniform, and rotationally-symmetric structure. Rather, they may indicate local inhomogeneities in the undisturbed CSM, or they may simply trace the outermost edge of the contact discontinuity. In the following, we will exclude them from our analyses.

Figure 44 shows all circumstellar material, simplified according to the above arguments. The outer structure is peanut-like, extended along the poles to $r \lesssim 28$ ly, and narrowly-pinched at the waist at $r \sim 5$ ly. We will henceforth refer to this outer shell (traced by the CD and outer NH echoes) as the “Peanut.” Roughly 35° from the equatorial plane are the spurs, extending 3–4 ly out from each lobe, perpendicular to the Peanut’s axis. Unlike the northwestern WFPC2 echoes, these spurs do appear at more than one location, but they are limited enough in extent that it is unclear whether they are uniform features that encircle the entire structure, or are iso-

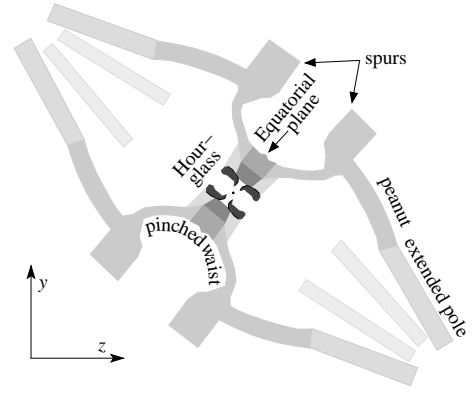


FIG. 44.— Revised cartoon showing the simplified CSE suggested in Figs. 27, 34, and 39. Structures are shaded to indicate density, which increases with greyscale. Fig. is to scale, and orientation arrows indicate 10 ly.

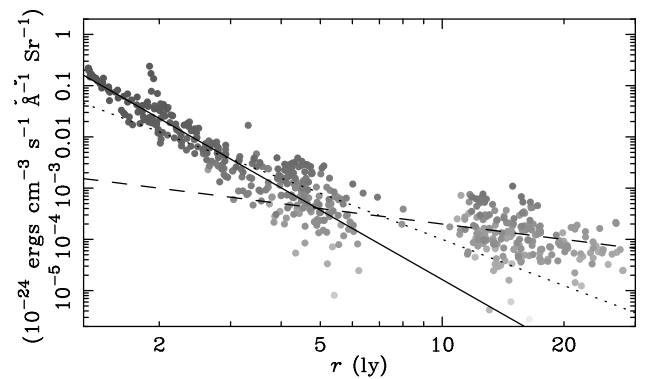


FIG. 45.— Flux density of scattered light per unit volume as a function of 3-D radius from the SN, measured for each echo in the F612 filter. Points are shaded in proportion to their signal-to-noise, which increases with darker greyscale. Lines are plotted as follows: $j \propto r^{-1}$ (dashed), $j \propto r^{-3}$ (dotted), $j \propto r^{-4.5}$ solid.

lated clumps.

Inside the equatorial region of the Peanut is a thick (~ 3.5 ly in radial thickness, 2 ly in axial length) annular ring (or belt), which extends inward until it terminates at the inner CS hourglass. The extent of this waist in z' is unclear. Echoes were detected outside the CS hourglass at most equatorial (π') radii between 1.6 and 4 ly, with a vertical (z') distribution extending at least as far as the CS hourglass itself. Still, the bulk of material is within 1 ly of the equator.

9.2. Density of the Circumstellar Material

To constrain the gas density and dust composition of the CSE, we apply the dust-scattering model from §2.4 using the surface brightnesses of each echo discussed in §6–8. Fluxes were only measured in the F470, F612, and F688 filters. Our integrated SN spectrum does not extend to 8090\AA , thus the model cannot be applied to the F809 filter without making considerable assumptions. We chose not to include measurements from WFPC2 data for a number of reasons. First, echoes were very extended and faint, resulting in large photometric errors. Second, intercomparing the observations from wide-band WFPC2 filters with the narrow-band, continuum-only ground-based data is challenging, due to e.g. potential line contamination, different filter wavelengths and widths, etc.

Figure 45 shows the volume emissivity j (flux density per

TABLE 4
SUMMARY OF ECHO GEOMETRIES

Structure	Inclination ^a			Cross Section ^b			Shape	Geometry ^c				
	i_x (°)	i_y (°)	i_z (°)	b/a	Δx_0 (ly)	Δy_0 (ly)		r (ly)	z' (ly)	π' (ly)	$\Delta\pi'$ (ly)	V_{tot} (ly ³)
CS	41°	-8°	-9°	0.94	$\lesssim 0.1$	0.	Hourglass	1–2.9	0.3–2.5	0.8–1.6	0.5–1	20
							Belt	1.5–2.8	0.–1.0	1.5–2.6	1.5–2.0	40
							Walls	1.8–4.2	0.8–2.7	1.8–3.6	2.0–3.0	120
NH	40°	-7°	12°	0.82	0.	0.	Hourglass	3–11	0.7–7.5	2.8–7.5	2–4	1300
CD	40°	-8°	...	$\gtrsim 0.95$	< -1	$\lesssim -0.1$	Prolate	10–28	4–28	0–16	4–5	1.2×10^4

^aPYR angles applied in order of roll-pitch-yaw (§5.3.1).

^b Δx_0 and Δy_0 are the western and northern offsets of the symmetry axis from the SN, which is at $x = 0, y = 0$.

^cSee Fig. 12 for coordinate definitions. $\Delta\pi'$ is the approximate width along π' . V_{tot} is the inferred total volume of the structure.

unit volume) of all echoes in F612 as a function of radius. Note that 2-D surface brightness was converted to 3-D flux density using the line of sight echo depth Δz given in Eq. (eq. [5]). This can be compared with Figure 3 of Crotts & Kunkel (1991). If the density of material is constant, j will decrease as r^{-1} (Eq. [12] of Sugerman 2003), while a uniform wind blowing into a homogenous, low density medium will produce an r^{-3} emissivity profile. These are shown in the figure as dashed and dotted lines. The outer-NH and CD echoes are well-described as constant density, while some NH/CS material may follow an r^{-3} profile. The best fit to the CS and inner-NH points follows $r^{-4.5}$, which is suggestive of a disturbed CSE, such as would occur via interacting stellar winds.

Recall from §2.4 that we defined three dust-grain size distributions: S, M, and L. We begin with type-L dust. The results are shown for pure-carbonaceous (C-only), pure-silicate (Si-only), and an LMC-abundance mixture (Ci+S) in Figure 46(a). For clarity, densities are plotted logarithmically but positions are given linearly, with the horizontal scale changing between each vertical line, which roughly delineate CS, NH, and CD material.

The C-only dust yields a close fit between F612 and F688 for the CS material, but the F470 is uniformly too dense. An overdensity implies a large scaling n_H , which results from an underluminous prediction. Since this dust does not produce enough blue flux, the model is too red. The Si-only model reconciles the F470 and F688 points, but predicts too much flux in F612. Adding carbon to silicates reddens the spectrum, which again pushes F470 densities to be slightly too high. Overall, the Si-only is the better fit.

For the most part, the NH densities vary in a similar fashion. The C-only model is too red, while the Si-only dust is a very good fit. Adding C to Si reddens the model slightly, making the F470 densities slightly more discrepant with the red points. The Si-only model is again the better fit. Finally, the CD echoes are well fit by all three models, with the C+Si model having the lowest scatter between filters.

Figure 46(b) shows the type-M model results. For the CS structures, the C-only model is a reasonable fit to the F470 and F688 data, yet the F612 flux is too high. Si-only dust is overly red, and adding carbon does little to improve the fit. Since smaller particles do not scatter enough red flux, the CS dust is better fit by a distribution including some large grains. The NH material is reasonably-well fit by all three models, but the least dispersion between filters occurs when silicates are present. Type-M dust is not a good fit for the CD, since this model is overluminous in F612 and too blue. Although not shown, the fits of the type-S model are poor

since the spectrum is too blue.

The CD colors require large grains, and are best-fit by the type-L C+Si model. Neither L nor M models are satisfactory fits to the NH and CS echoes, which leads us to explore intermediate grain-size ranges. We tested a number of upper size limits between $a = 0.1 - 2.0 \mu\text{m}$, and find that smaller values fit better. The CS and inner NH data ($r < 5$ ly) have the lowest dispersion between filters for Si-only, $a_{max} = 0.2 \mu\text{m}$ dust. We will denote this new size range as ML, as it includes particles slightly larger than the type-M dust. Outer-NH data ($r > 5$ ly) are more consistent with Si-dominated dust with larger grains. The general trend is that inner echoes are better reproduced by smaller, Si-dominated dust, and with increasing distance, the grain sizes and C-content increases.

Fischera, Tuffs, & Völk (2002) have modeled mid-IR emission from collisionally-excited dust grains heated in the shocks between the H II region interior to the ER and the forward blast of the SN. They find the emission is best explained by small ($a \lesssim 0.25 \mu\text{m}$) grains with a Si-Fe or Si-C composition. The dust abundance is quite low, which they attribute to evaporation from the UV flash and sputtering in the shocked gas. This further constrains grain sizes to $a \lesssim 0.25 \mu\text{m}$ and excludes a pure-carbon composition. The dust in both this H II region and the CS hourglass was formed from material expelled very late in the progenitor's life, thus we expect the dust properties to be similar. Indeed, our CS-dust model also favors silicate-dominated¹¹ dust with small grains ($a < 0.2 \mu\text{m}$).

Our models suggest that dust which formed at later times (and is consequently closer to the star) has a smaller carbonaceous-component. This can result from a change in surface CNO abundances over the star's late-stages of evolution, since carbon-rich envelopes create carbon-rich dust, while oxygen-rich envelopes create silicate-rich dust. Such CNO processing is also inferred from early IUE spectra (Fransson et al. 1989) of the ER, which show nitrogen and oxygen to be overabundant with respect to carbon.

The average dust density, taken from the best model results above is plotted in Figure 46(c). The innermost CS hourglass material has a relatively-constant gas density of $n_H = 2 - 3 \text{ cm}^{-3}$ up to $r \sim 1.6$ ly. We note that this value is consistent with the findings of Burrows et al. (1995), who argued the CS hourglass must have a density $\lesssim 5 \text{ cm}^{-3}$ to not be observed in recombination in WFPC2 images.

Beyond this position, the material splits into two distribu-

¹¹ "Astronomical silicate" dust parameters used in our model (Draine & Lee 1984; Weingartner & Draine 2001) are derived from olivine, a magnesium-iron-silicate.

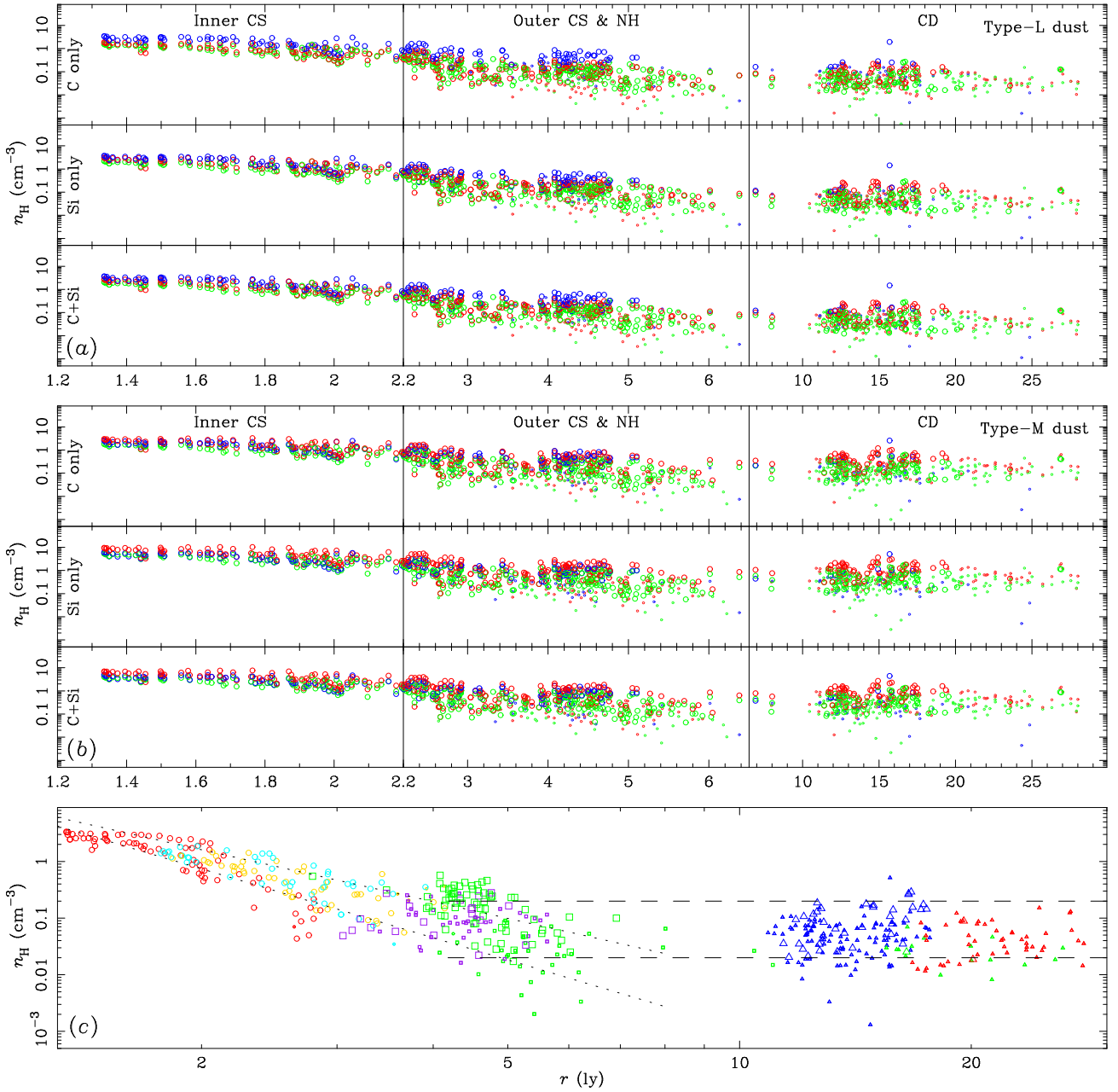


FIG. 46.— Gas density versus radius for the dust scattering model. Model results are shown for (a) type-L and (b) type-M dust. Each filter is shaded (roughly) corresponding color: F470 in blue, F612 in green, F688 in red. Large circles denote signal-to-noise above 2, and small ones show $S/N < 2$. The abscissa changes between columns, each of which contains the structure as noted in the top subpanel. Rows show the results for the dust compositions listed to the far left. (c) Average gas densities that match observed echo fluxes to the dust-scattering model. Note that the abscissa is shown in now logarithmic. Point colors correspond to those in Fig. 43. CS material is marked by circles, NH by squares, CD by triangles, and smaller symbols denote measurements with $S/N < 2$. Dotted lines are the best-fits through the upper and lower CS loci, corresponding to $n \propto r^{-3.0}$ (upper) and $n \propto r^{-4.5}$ (lower). Horizontal dashed lines delineate the rough density boundaries of the CD gas.

tions, for which density drops either slowly ($n_H \propto r^{-3.0 \pm 0.2}$) or rapidly ($r^{-4.5 \pm 0.2}$) with radius. Material outside the hourglass tends to lie along one of these two distributions, up to a radius of roughly 4 ly. That the density varies more steeply than the inverse-square expected for a freely-expanding wind suggests the mass-loss mechanical luminosity ($\dot{M}v_{exp}^2$) increased with time toward the end of the RSG.

The densest material traces the waist of the hourglass. The hourglass points along the r^{-3} profile are those at large π' for a given z' , which lie outside the average hourglass position, designated by the “extended flux” squares in Figure 38. Beyond

$r = 2$ ly, this profile traces the belt and equatorial plane material. The steeper, $r^{-4.5}$ profile includes most hourglass material and extends to include the inner and outer “walls.” Allowing larger dust grains or increasing the carbonaceous content of the dust shifts the densities uniformly lower by only 10%, thus these results are reasonably robust against the particular model chosen.

The outer CS gas makes a smooth transition to the inner NH points around $r \gtrsim 3$ ly. The two profiles described above also bound the majority of the NH gas up to a radius of 6 ly. Excluding a density enhancement between $r = 4 - 5$ ly, there

is no evidence of a structural distinction between the CS and NH gas, which justifies the simplified model in Figure 44. Returning to the aforementioned enhancement, there is a thin shell or wall at $r \sim 4.5$ ly, of thickness ~ 1 ly and density $n_H = 0.2 - 0.3 \text{ cm}^{-3}$, roughly three times higher than the rest of the NH gas. This high-density material is located primarily along the waist of the NH hourglass around $\pi' = 4 - 5$ ly, marking an outer edge to the equatorial overdensity.

The CD density is constant with radius, and bounded by $0.02 \leq n_H \leq 0.2 \text{ cm}^{-3}$, which are delineated by dashed lines Figure 46(c). The greater majority of the NH gas is also bounded by these values, confirming the suggestion from Figure 45 that the outer NH and CD mark a constant-density boundary. Although not a significant trend, the inner CD gas (blue conical-shell material), is at slightly higher density ($n_H \sim 0.06$) than the red, radial material at larger radii ($n_H \sim 0.04$). The green (radial jet) points have the lowest density around $\sim 0.02 \text{ cm}^{-3}$.

The greyscale shading of structures in Figure 44 reflects the differences in density among the many echoing structures, with darker grey indicating higher-density material. The picture of the CSE will be completed in the following subsections, in which we reexamine the Peanut's pinched waist, measure the density of dust between the bright echo structures, and estimate the total mass of all CSE material.

9.2.1. The Peanut: a Pinched Waist or Shadowing?

According to Figure 44, the CD and NH form a Peanut with a narrowly-pinched waist. To interpret this as the contact discontinuity between the RSG and MS winds, we must assume there is no disturbed MS material beyond these structures. The alternative is that material is present outside the waist of the NH structure, but that it was not illuminated by the SN pulse because of significant extinction, or shadowing, from equatorial material interior to the Peanut.

Heuristically, this situation is unlikely. That echoes were observed within 0.5 ly of the equatorial plane (Fig. 43h,l) demonstrates SN light did illuminate this region, so it is difficult to argue that the entire equatorial region is shadowed from, for example, the ER. An alternative is that all material inside NH has shadowed any material outside it. Let us assume the waist of the Peanut (NH echoes) has a lower density than the CS equatorial disk. Extinction scales with density, so the waist of the Peanut will cause much less shadowing than the material inside it. Otherwise stated, the Peanut itself contributes very little to the total optical depth, and therefore should not have been illuminated by echoes. Since NH echoes were observed at the equator, we conclude that material outside NH should have been illuminated as well, which is not the case.

If, alternatively, the waist of the Peanut has very high density and is optically thick, then less light will be scattered toward the observer than expected in our optically-thin model, and we will underpredict the actual dust densities by a large margin. We find the NH dust has about the same density as the CD shell of the Peanut in the previous section, which means the *actual* NH density must be just the right amount to *appear* to have the same properties as the CD material. This seems highly improbable, and leads us to doubt that any strong shadowing has occurred.

A conservative estimate of the column density of all equatorial dust, by integrating $n_H \times r$ to a radius of 6 ly in Figure 46(c), is $N_H \sim 6 \times 10^{18} \text{ cm}^{-2}$. The ER was not observed in echoes, however an average gas density of 10^4

cm^{-3} (Sonneborn *et al.* 1997) and observed width of 0.3 ly (Burrows *et al.* 1995) yields an additional column of $N_H \lesssim 3 \times 10^{21} \text{ cm}^{-2}$. The total extinction (Sugerman 2003) at 6120\AA for type-ML dust will be $A_{6120} = 5 \times 10^{-23} N_H$ for C+Si particles, and 30% smaller for Si-only. The total extinction from the SN to NH will be less than 0.2 mags, which will only attenuate the SN pulse by 13%. Since the column density within the ER is over two orders of magnitude larger than in the CSM, any shadowing from the ER would have hidden the CS and NH echoes as well.

If the ER is only the ionized skin of a much more extended equatorial disk (Plait *et al.* 1995) then the equatorial extinction will be correspondingly higher. Only if this disk has constant density and extends out to 1.5 ly can the equatorial extinction approach an optical depth of unity. Again, this seems unlikely. The qualitative and quantitative cases for shadowing are dubious, thus the narrow waist appears to be a genuine boundary.

9.2.2. An Unbiased Measurement of Density

The previous results are biased, in the sense densities were measured only in those regions known to be dense. Any dust intersecting an echo parabola will scatter light toward the observer, thus if any is present between or external to the known structures, its signature should be recorded in faint, background surface brightness. To probe these regions, we applied the dust-scattering model to unbiased photometry, as follows.

Surface brightness was remeasured in all difference images (Fig. 10) through circular-arc annuli from $0''.3$ to $50''$ (or $45''$ until 1990, as explained below) from the SN. Photometry beyond $\rho \sim 25''$ is intrinsically unreliable, since at these radii we made no effort to keep the reference images echo-free. However, with the exception of echo R310 ($\rho \sim 45''$ until 1990), all interstellar echoes (Xu *et al.* 1994, 1995) are located beyond $\rho = 50''$, and therefore cause no contamination. The results are shown in Figure 47, using the type-L Si+C dust model. Note that this figure extends to 300 ly in radius, a factor of 10 greater than the spatial coverage in Figure 46(c).

Panels (a) and (b) differ only in how surface brightnesses were measured. Semi-circular annuli, centered at P.A. 0° and 180° , were used in panel (a) to probe uniform, faint variations in background flux while smoothing over discrete, non-echo signal. Panel (b) shows the results from annuli of arclength 20° , centered at P.A.s 90° , 135° , 180° , 225° , and 270° , which better preserve small or non-circular echoes. In both cases, the average profile (black points and error bars) is determined as the weighted average of densities binned in radius.

A number of known features are recovered, such as the CS material at small radii, the denser waist of the Peanut around $r = 4$ ly, and the bright CD between 11–22 ly. The average density between the CS and CD structures ($r = 4 - 22$ ly) decreases as r^{-1} in panel (a), and $r^{-2.0 \pm 0.5}$ in panel (b). The exact value of the exponent is sensitive to the particular limits in radius. Nonetheless, the interior of the CD is filled with diffuse material.

As expected, the semi-circular apertures smoothed over most of the CD structure, however, a drop in density around $r = 30$ ly in panel (b) is consistent with its outer boundary. External to the CD, the gas density is very uniform with an average value of $0.01 - 0.02 \text{ cm}^{-3}$, up to a radius of 80–90 ly, at which there is a marginal density peak. These same densities correspond to that expected from a background-noise-only model at $r > 30$ ly, and are thus only upper limits to the actual density in this region.

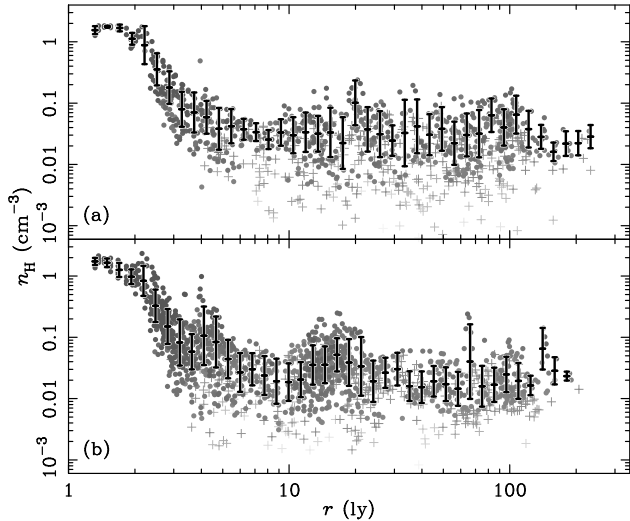


FIG. 47.— Type-L Si+C dust-scattering model densities for all flux within $50''$ of the SN, as measured through (a) semi-circular annuli centered at P.A. 0° and 180° , and (b) 20° annular wedges centered at P.A.s 90° , 135° , 180° , 225° , and 270° . Signal-to-noise increases with greyscale, and points with $S/N < 1$ are shown as crosses (included since our error estimates are very generous). Weighted averages measured through bins of constant $\Delta(\log r)$ are shown in black.

9.3. Total Mass of the Circumstellar Environment

The total mass of gas and dust within the CSE is estimated from the average density and volume of each structure. The volumes of the probable structures traced out by light echoes are measured by integrating the binned radial profiles in Figures 26, 32, and 38. Each profile is assumed to represent a surface of revolution, and the limits of integration in π' are determined as a convolution of the standard deviation of the average profile with the average spatial extent of each echo position, transformed into the cylindrical coordinate system. The resulting values are given in the final column of Table 4. The volume interior to the CD is estimated a few ways: as the volume of the ellipsoid enclosed by the CD, as the volume of two cones enclosed by the quasi-linear profile, and as the integrated volume under the same profile (Fig. 26). All three methods give a consistent result of about 6500 ly^3 .

The estimated masses of each structure are listed in Table 5, yielding total mass in all structures of $\sim 1.7M_\odot$. Since the gas-to-dust mass ratio is large (400–600), dust contributes a negligible fraction to the total mass. Number density is converted to mass density by $\rho_g = \mu n_H m_H$ where $\mu = 1.4$ is the cosmic average value. It is very difficult to quantify all the sources of error that enter these values, but we believe the tendency will be to underpredict the masses of the structures, given conservative measurements of their volume and the unknown extent to which dust was not observable, due to unfavorable geometry, poor data quality, confusion, or possible shadowing.

10. CONCLUSIONS

In this work, we have presented the discovery and analysis of light echoes illuminating material within 30 ly of SN 1987A. These results are also summarized in the first half of Sugerman et al. (2005), after which we show that no existing formation scenarios can explain this newly-revealed circumstellar nebula.

As noted in the introduction, the outflows from Sk $-69^\circ 202$

TABLE 5
MASS OF THE CSM

Structure	M/M_\odot
CS Hourglass	0.04
CS Belt	0.04
CS Walls	0.06
NH Waist	0.06
NH Walls	0.07
Intra-CD	0.2
CD	1.2
Total	1.7

are one example of a much wider class of bipolar outflows seen in many different classes of evolved stars. A small sampling of these include the supermassive LBV η Car, the B1.5ab BSG star 25 Sher in NGC 3603, the symbiotic star He 2-104, the “Etched Hourglass” MyCn 18, and the “butterfly” nebula M2-9. The underlying physical processes producing these objects are still far from understood. If the shaping of bipolar outflows occurs very early in the mass-loss history of a star, then the seeds of bipolarity or asymmetry have a strong effect on subsequent outflows, but are also erased by those same winds. Reconstructing these objects’ mass-loss histories is very difficult since there are few observational constraints extant from their early stages of evolution. Yet such “stellar paleontology” is critical to understanding the mechanisms of aspherical stellar-mass loss.

As one researcher recently noted at a conference on asymmetric planetary nebulae (Meixner et al. 2004), “most astronomers would gladly give a month’s post-doc salary to know the three-dimensional structure of a bipolar nebula.” The light echoes from SN 1987A have finally provided just that, not only for the visible nebula, but additionally for the products of stellar mass loss from the last $\gtrsim 3 \times 10^5$ years of the star’s life. It is our hope that this work will provide both a motivation and a means to readdress first the mechanisms of mass loss in Sk $-69^\circ 202$, and subsequently the phenomena of bipolar mass loss in many more systems.

B.E.K.S. wishes to thank Alex Bergier for assistance in ground-based image reduction, Robert Uglesich for assistance with difference imaging, and Eric Blackman, Roger Chevalier, Adam Frank, Peter Lundqvist, and Geralt Mellema for useful discussions. We gratefully acknowledge our referee, Richard McCray, for his critical reading and insightful feedback on all the manuscripts in this series. This research was based in part on observations made with the NASA/ESA Hubble Space Telescope, obtained from the Data Archive at the Space Telescope Science Institute, which is operated by the Association of Universities for Research in Astronomy, Inc., under NASA contract NAS 5-26555. This paper also made use of publically-available data from the SUSPECT supernova spectrum archive. 3-D rendering was accomplished with *pgplot*, maintained by Tim Pearson at the California Institute of Technology. *Synphot* is developed and maintained by the Science Software Group at STScI. This work was generously supported by STScI grants GO 8806, 8872, 9111, 9328, 9428, & 9343; NASA NAG5-13081; NSF AST 02 06048; and by Margaret Meixner and STScI DDRF grant 82301.

APPENDIX

A. THE *DIFIMPHOT* DATA PIPELINE

The difference imaging pipeline requires the following steps: (1) geometric registration, (2) creating the reference image, (3) building the PSF, and (4) PSF-matching and differencing. Step (1) is discussed in §4.3.1; the rest are described below.

A.1. *The Reference Image*

A successful implementation of PSF-matched difference imaging will remove all constant sources of flux, leaving the desired signal from time-variable sources, and unavoidable contributions from statistical noise, residuals from bright stars, and cosmetic defects. Images within a dataset may be differenced against each other, to test for relative changes. Preferably a “reference” (or master) image, which represents the median flux of all stars, may be subtracted from all input images. In this implementation, we combine all images in a given filter to create an “echo-free” reference image, as described in §4.3.2.

A.2. *PSF Building*

PSF-matching two images requires high signal-to-noise empirical PSFs with clean profiles well into the wings. Building such PSFs can be difficult in sparse and crowded fields. In sparse fields, finding a sufficient number of bright stars to build a PSF representing the average stellar profile can be problematic. In crowded fields, isolating bright stars from many nearby, faint sources is the dominant challenge. We address both problems by using the PSF-building software from *daophot* in an iterative technique, as follows.

A candidate list of PSF stars is generated from the reference-star list (§4.3.2), using only those members that do not have any bright neighbors within $\gtrsim 3 \times \text{FWHM}$ pixels. Saturated stars are rejected, but stars with non-linear profiles are kept. The test PSF is built from the N brightest linear-profile stars, with non-linear stars used only to supplement the wings. The *psf* algorithm fits an analytic function to each profile and computes the residuals of the star from that function. A weighted average of all profiles, normalized to that of the brightest star, is the temporary PSF. This is compared to each input star, and those with residuals that deviate from the model are down-weighted in successive iterations.

The output model PSF is fit to each candidate star in the original list, and up to N of the best fit stars are used as a second input list to the PSF-building algorithm. Applying a cut-off to the fit quality is highly effective at removing stars with faint neighbors that would otherwise contaminate the wings of the PSF, as well as removing non-linear and blended stars.

A.3. *PSF Matching and Differencing*

Both the input and reference images are evaluated for seeing, and the better-seeing (i.e. lower FWHM) of the two is chosen as image r . PSF-matching proceeds by first using equation (8) to build the convolution kernel from the input and reference PSFs.

Although we take great care to build high-quality PSFs, the noise in the wings can be quite high, since these are the lowest-flux components of the radial profile and are therefore the most-poorly determined. As the PSF of a star is roughly gaussian, a fixed percentage of the PSF wings is modeled and replaced by the FT of an elliptical gaussian. The particular percentage to replace depends on the number and flux of stars used to build the PSF. In most applications, we find no more than 10% of a PSF need be replaced, with a well-sampled (~ 20 stars) PSF needing only a 3% replacement.

Image r is convolved with the kernel k to PSF-match it to the poorer-seeing image i . The photometric scaling c between i and r is evaluated from the reference stars (§4.3.2) present in both images. The difference image is then given by $i - c(r * k)$. It has been found that images that are already close in seeing often need to be PSF-matched twice, with the first set of matched images as input for a second matching iteration.

B. NUMERIC MODELING OF DATA

The generalized problem of finding the parameters $\mathbf{a} = a_j$, $j = 1, M$ that best-fit the function $y(x) = y(x, \mathbf{a})$ to the N data points (y_i, x_i) is solved by minimizing the chi-squared merit function

$$\chi^2 \equiv \sum_{i=1}^N \left(\frac{y_i - y(x_i, \mathbf{a})}{\sigma_i} \right)^2, \quad (\text{B1})$$

where σ_i is the weight of y_i . In cases in which the function is not linear in x_i , chi-squared minimization requires an iterative procedure that relaxes χ^2 by variation of parameters \mathbf{a} . Our preferred technique is the use of Levenburg-Marquardt (LM) minimization (Press et al. 1992). Briefly, one varies a trial set of parameters \mathbf{a} using the method of steepest descent, by computing the gradient and Hessian of $\chi^2(\mathbf{a})$.

Although very powerful, LM minimization has numerous (yet unavoidable) pitfalls. First, the topography defined by $\nabla \chi^2$ can have many local minima into which the fit can relax, missing the absolute minimum. The minimization algorithm is known to wander near a minimum if the topography is flat. Complicated functions with many parameters often require that the user hold certain ones fixed while varying others, lest the fit reside permanently in local minima. Occasionally, the function can realize a minimized χ^2 through an entirely unreasonable set of parameters. Despite these difficulties, the technique is robust and the standard of nonlinear fitting.

Since the datapoints may not have normally-distributed errors, and many fits are to functions of more than one dimension, we adopt the bootstrap technique (see Press et al. 1992) to estimate the uncertainties in the fitted parameters. Below, we describe explicitly a number of non-trivial minimizations used in this work.

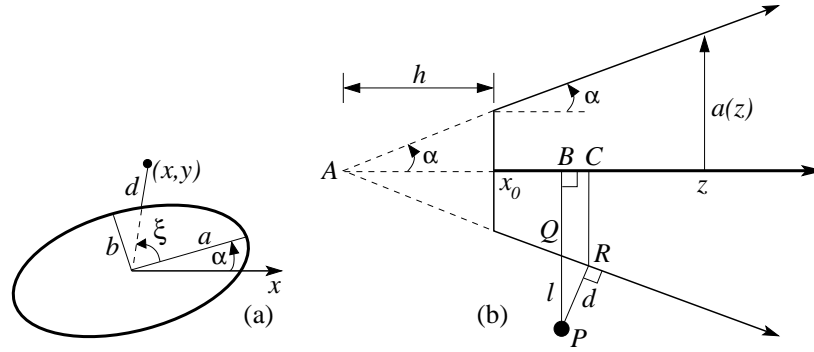


FIG. B48.— Schematic geometries for Levenburg-Marquardt fitting, for (a) an ellipse, and (b) a cone or frustum.

B.1. Gaussians and Moffats

A moffat is a modified Gaussian, and can be expressed in terms of its peak A , center x_0 , and FWHM σ as

$$y = A \left[1 + \frac{4(2^{1/\beta} - 1)}{\sigma^2} (x - x_0)^2 \right]^{-\beta} \quad (\text{B2})$$

where $\beta \rightarrow \infty$ yields a Gaussian. Any number of moffats can be fit simultaneously, with four parameters per function.

B.2. Ellipses

The cartesian expression for an ellipse with center (x_0, y_0) and semi-major and minor axes (a, b) is not a form conducive to LM fitting for many reasons, not least of which is that it is particularly complicated to account for rotations by some angle α (see Figure B48a). Rather, the ellipse can be expressed in parametric form as $(x = a \cos \xi, y = b \sin \xi)$ with parameter ξ . To fit an ellipse to a locus of points, we minimize the geometric distance between the ellipse and the data as follows. Data are shifted by $(-x_0, -y_0)$ and rotated by $-\alpha$, then for each datum, the value of ξ is found that minimizes the point's distance from the ellipse defined by (a, b) . This specific minimization can be accomplished by simple numeric bracketing, and as ξ is only used to find points on the ellipse, not to define it, it is not fit by the LM algorithm. The χ^2 merit function is the sum of the distance of all transformed data from the ellipse, and is minimized by varying the five parameters $\{(x_0, y_0), (a, b), \alpha\}$.

Explicitly, this is a two-dimensional fit for the distance function $d = d(\mathbf{x}_i, \mathbf{a}) \equiv \sqrt{X_i^2 + Y_i^2}$, where

$$\begin{aligned} X_i &= x_i - (x_0 + a \cos \alpha \cos \xi_i + b \sin \alpha \sin \xi_i) \\ Y_i &= y_i - (y_0 - a \sin \alpha \cos \xi_i + b \cos \alpha \sin \xi_i). \end{aligned}$$

The absolute minimum distance of all data to the ellipse is zero, thus we wish to find the parameters such that $d(\mathbf{x}_i, \mathbf{a}) \approx 0$. In the relevant analog to equation B1, $\chi^2 = \sum_i d(\mathbf{x}_i, \mathbf{a})^2$. N.B. Here, χ^2 is a measure of the total distance of all points from the ellipse, and does not carry statistical interpretations such as absolute goodness-of-fit. Rather, $\sqrt{\chi^2/(N-1)}$, where N is the number of points to be fit, is the root-mean-squared (RMS) scatter of the fit.

B.3. Three-Dimensional Lines

Finding the orientation and position of a 3-D line that fits data is equivalent to finding the transformation that aligns the data with a fixed line. Define that transformation as the vector offset (x_0, y_0, z_0) and pitch-yaw-roll (PYR) rotation through angles (θ, ϕ, ψ) . As for the ellipse, we seek to find the six parameters that minimize the total distance from all transformed points to the z axis. The same caveat discussed above, regarding the statistical interpretation of χ^2 , applies.

B.4. Cones and Frusta

As with the ellipse, the traditional cartesian definition of a cone is not conducive to LM minimization. Rather, we implement a novel combination of the previous two subsections. A cone can be considered as a series of nested ellipses aligned along a given vector \hat{n} , where the axes of each ellipse are functions of the distance of its center from some point \mathbf{x}_0 . If the ellipses have non-zero major and minor axes at \mathbf{x}_0 , the figure is a truncated cone or frustum. The distance from the apex to the truncated top edge is defined as h (see Figure B48b).

Proceeding as before, the data are rotated and translated to fit them to a cone aligned along the z axis. The major and minor axes are defined to be $a(z) = a_0(|z| + h)$, $b(z) = b_0(|z| + h)$, where h is defined above. Defined in terms of $|z|$, an hourglass (two cones reflected about the $x-y$ plane) can also be fit.

Consider the point P as shown in Figure B48b. In truth, it is a distance d from the cone, however calculation of the point R , or its projection C on the z axis, is a complicated function with extremely complicated partial derivatives. Rather, note that the triangles $\triangle AQB$ and $\triangle PRQ$ are similar, and if the cone has a fixed half-opening angle ($\angle BAQ = \alpha$), $d/l = \cos(\angle QPR)$ is a fixed ratio, thus minimizing l is equivalent to minimizing d . The application of this is simple, since the distance l can be measured using the technique from §B.2. Note however that the half-opening angle α is fixed only for a cone with circular cross section

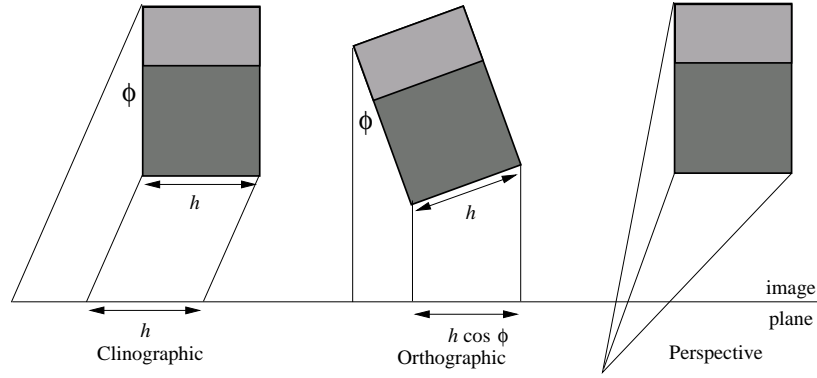


FIG. C49.— Schematic showing the principles of clinographic, orthographic, and perspective projections onto an image plane. In each case the figure is a cube, rotated such that two opaque faces can be seen (dark and light grey) from above. After Fig. 1 of Angell & Moore (1984).

($a_0 = b_0$). For the general case of an elliptic cross section, d/l is not constant with angle about the z axis. However, restricting this technique to small eccentricities ($a \lesssim b$), d/l is approximately constant, and this technique is still valid.

Requiring that the axis of the cone pass through the origin, the center $\mathbf{x}_0 = k\hat{n}$, where \hat{n} is the unit vector \hat{k} rotated by the PYR angles (ψ_z, θ_x, ϕ_y). This cone (or frustum) can be fit by seven parameters: three rotation angles, two ellipse axes, h and k . For a general center \mathbf{x}_0 , the fit requires nine parameters. However, in the adopted PYR rotation convention, ψ_z has no effect for a circular cross section, for which case the above fits are reduced to five and seven parameters, respectively.

C. VISUALIZATION TRANSFORMATIONS

A very large number of projections exist to represent a 3-D object on the two-dimensional image plane of a piece of paper. Three of these are shown in Figure C49. A clinographic projection views an object from an angle ϕ with each point on the cube projected onto the image plane by a parallel line. The cube is now seen including the top face, and the size h of the cube is preserved. An orthographic projection first rotates the cube by the angle ϕ and then projects the image onto the plane with orthogonal lines, such that the side h now has a length $h \cos \phi$. Such “parallel projections” are difficult to interpret visually since we do not observe 3-D structures this way. Rather, our eyes apply conical or perspective projections, by which the relative sizes of points diminish with increasing distance from the observer. Since parallel lines project to an imaginary apex, zonal relationships appear slightly distorted, but are also easier to understand.

To view a 3-D object, one first applies orthogonal transformations (positional shifts, rotations, scalings), then the resulting object is projected onto the image plane using either a parallel or perspective transformation. The general case provides for: a linear shift in three dimensions, rotations about three axes, a uniform scaling, followed by a dimetric and perspective projection. Consider the image plane as a vertical pane of glass, with the object held in front of the pane by a metal rod, connected orthogonally to the glass. The dimetric projection is an orthographic projection applied in two dimensions, and establishes where along the glass the observer is located with respect to that rod. The perspective projection corrects for the distance of the observer behind the glass.

All of these can be easily specified as 4×4 matrices. A rotation R , shift S , and translation T are given by

$$R = \begin{pmatrix} a & b & c & 0 \\ d & e & f & 0 \\ g & h & i & 0 \\ 0 & 0 & 0 & 1 \end{pmatrix} \quad S = \begin{pmatrix} s & 0 & 0 & 0 \\ 0 & s & 0 & 0 \\ 0 & 0 & s & 0 \\ 0 & 0 & 0 & 1 \end{pmatrix} \quad T = \begin{pmatrix} 1 & 0 & 0 & 0 \\ 0 & 1 & 0 & 0 \\ 0 & 0 & 1 & 0 \\ \Delta x & \Delta y & \Delta z & 1 \end{pmatrix}$$

where for R we have left the sin and cos coefficients out since they vary with the particular convention used (i.e. Euler angles versus pitch-yaw-roll). A dimetric projection P_d extrudes projected surfaces in the direction of a viewing vector \vec{v} . A perspective projection P_p is defined by the parameter α , where $\alpha \rightarrow \infty$ reduces to an orthographic projection with $\phi = 0$. They are given by

$$P_d = \begin{pmatrix} 1 & 0 & 0 & 0 \\ 0 & 1 & 0 & 0 \\ -v_x/v_z & -v_y/v_z & 0 & 0 \\ 0 & 0 & 0 & 1 \end{pmatrix} \quad P_p = \begin{pmatrix} 1 & 0 & 0 & 0 \\ 0 & 1 & 0 & 0 \\ 0 & 0 & \alpha^{-1} & \alpha^{-1} \\ 0 & 0 & 0 & 1 \end{pmatrix}$$

To apply a perspective projection, the position vector $(x, y, z, 1)$ is multiplied by P_d and then normalized by the fourth component, i.e. a perspective-transformed point is given by

$$\left(\frac{\alpha x}{z + \alpha}, \frac{\alpha y}{z + \alpha}, \frac{z}{z + \alpha} \right).$$

Any combination of orthogonal and perspective transformations can be applied by finding the matrix product of all relative transformations, and then applying that new matrix to each 3-D datum, loaded into a 4-vector as above. The projected position onto the image plane is given by the first two components of the final vector, the third component fills the z -buffer to store depth information, and the fourth component returns to 1.

In our implementation of the 3-D rendering described in §5.3.2, we find the dimetric projection is never needed. Most renderings in this work have been generated with $\alpha = 10$, which creates a shallow perspective that aids the eye in understanding the correct orientation of the coordinate box, but has a small effect on zonal relationships.

REFERENCES

- Alard, C. 2000, *A&AS*, 144, 363
 Alcock, C. et al. 1995, *AJ*, 109, 1653
 Angell, I. O. & Moore, M., 1984. Teaching Pamphlets 12: Projections of Cubic Crystals, International Union of Crystallography, (Cardiff: University College Cardiff Press)
 Arnett, W. D. 1987, *ApJ*, 319, 136
 Arnett, W. D. 1988, *ApJ*, 331, 377
 Arnett, W.D., Bahcall, J.N., Kirshner, R.P., Woosley, S.E. 1989, *ARA&A*, 27, 629
 Balick, B., Preston, H.L., Icke, V. 1987, *AJ*, 94, 164
 Bjorkman, J. E., Cassinelli, J. P. 1993, *ApJ*, 409, 429
 Blondin, J. M., Lundqvist, P. 1993, *ApJ*, 405, 337
 Bond, H. E., Gilmozzi, R., Meakes, M. G., Panagia, N. 1989 *IAU Circ.*, 4733
 Bond, H. E., Gilmozzi, R., Meakes, M. G., & Panagia, N. 1990, *ApJ*, 354, L49
 Bond, H. E., et al. 2003, *Nature*, 422, 405
 Burrows, C.J., et al. 1995, *ApJ*, 452, 680
 Cardelli, J. A., Clayton, G. C. & Mathis, J. S. 1989, *ApJ*, 345, 245
 Castor, J., McCray, R., & Weaver, R. 1975, *ApJ*, 200, L107
 Chevalier, R. A. 1986, *ApJ*, 308, 225
 Chevalier, R. A. & Emmering, R. T. 1989, *ApJ*, 342, L75
 Collins, T. J. B., Frank, A., Bjorkman, J. E., Livio, M. 1999, *ApJ*, 512, 322
 Couch, W. J., Malin, D. F. 1989, *IAU Circ.* 4739
 Couderc, P. 1939, *Ann d'Ap*, 2, 271
 Crotts, A. P. S. 1992, *ApJ*, 399, L43
 Crotts, A.P.S., & Heathcote, S.R. 1991, *Nature*, 350, 683
 Crotts, A. P. S. & Heathcote, S. R. 2000, *ApJ*, 528, 426
 Crotts, A. P. S., Kunkel, W. E. 1989, *IAU Circ.* 4741
 Crotts, A. P. S. & Kunkel, W. E. 1991, *ApJ*, 366, L73
 Crotts, A. P. S., Kunkel, W. E. & Heathcote, S. R. 1995, *ApJ*, 438, 724
 Crotts, A.P.S., Kunkel, W.E., & McCarthy, P.J. 1989, *ApJ*, 347, L61
 Draine, B. T. & Lee, H. M. 1984, *ApJ*, 285, 89 (Erratum: 318, 485)
 Feast, M. 1999, *PASP*, 111, 775
 Fischera, J., Tuffs, R. J., & Völk, H. J. 2002, *A&A*, 395, 189
 Fransson, C., et al. 1989, *ApJ*, 336, 429
 Fruchter, A. S. & Hook, R. N. 2002, *PASP*, 114, 144
 Gould, A., & Uza, O. 1998, *ApJ*, 494, 118
 Groth, E. J. 1986, *AJ*, 91, 1244
 Hamuy, M., Suntzeff, N. B., Gonzalez, R., & Martin, G. 1988, *AJ*, 95, 63
 Henyey, L. C. & Greenstein, J. L. 1941, *ApJ*, 93, 70
 Jakobsen, P., et al. 1991, *ApJ*, 369, L63
 Meixner, M., Kastner, J. H., Balick, B., & Soker, N. 2004, *Asymmetrical Planetary Nebulae III: Winds, Structure and the Thunderbird*, ASP Conference Proceedings, Vol. 313 (San Francisco, PASP) 2004
 Kwok, S.O. 1982, *ApJ*, 258, 280
 Li, A. & Draine, B. T. 2001, *ApJ*, 554, 778
 Livio, M., Soker, N. 1988, *ApJ*, 329, 764
 Lloyd, H. M., O'Brien, T. J., & Kahn, F. D. 1995, *MNRAS*, 273, L19
 Luo, D., & McCray, R. 1991b, 379, 659
 Luo, D., McCray, R., & Slavin, J. 1994, *ApJ*, 430, 264
 Martin, C. L., Arnett D. 1995, *ApJ*, 447, 378
 Mathis, J. S., Rumpl, W., & Nordsieck, K. H. 1977, *ApJ*, 217, 425 (MRN)
 Michael, E., et al. 2002, *ApJ*, 574, 166
 Misselt, K. A., Clayton, G. C., & Gordon, K. D. 1999, *PASP*, 111, 1398
 Panagia, N., et al. 1996, *ApJ*, 459, L17
 Plait, P., Lundqvist, P., Chevalier, R., Kirshner, R. 1995, *ApJ*, 439, 730
 Podsiadlowski, P., Fabian, A. C., & Stevens, I. R. 1991, *Nature*, 354, 43
 Press, W.H., et al. 1992, *Numerical Recipes in Fortran*, 2nd ed. (Cambridge: University Press)
 Romaniello, M., Salaris, M., Cassisi, S., & Panagia, N. 2000, *ApJ*, 530, 738
 Sanduleak, N. 1969, *Contr. CTIO*, 89, 1
 Scuderi, S., Panagia, N., Gilmozzi, R., Challis, P. M., & Kirshner, R. P. 1996, *ApJ*, 465, 956
 Shigeyama, T., Nomoto, K., Hashimoto, M., & Sugimoto, D. 1987, *Nature*, 328, 320
 Sonneborn, G., Fransson, C., Lundqvist, P., Cassatella, A., Gilmozzi, R., Kirshner, R. P., Panagia, N., & Wamsteker, W. 1997, *ApJ*, 477, 848
 Sonneborn, G., et al. 1998, *ApJ*, 492, L139
 Stetson, P.B. 1987, *PASP*, 99, 191
 Sugerman, B. E. K., 2003, *AJ*, 126, 1939
 Sugerman, B. E. K., Crotts, A. P. S., Kunkel, W. E., Heathcote, S. R., & Lawrence, S. S. 2005, *ApJ*, in press; astro-ph/0502268
 Sugerman, B. E. K., Lawrence, S. S., Crotts, A. P. S., Bouchet, P., Heathcote, S. R., 2002, *ApJ*, 572, 209
 Tomaney, A., & Crotts, A. P. S. 1996, *AJ*, 112, 2872
 Walborn, N. R., Prevot, M. L., Prevot, L., Wamsteker, W., Gonzalez, R., Gilmozzi, R., & Fitzpatrick, E. L. 1989, *A&A*, 219, 229
 Walker, A. R. & Suntzeff, N. B. 1990, *PASP*, 102, 131
 Wampler, J., D'Odorico, S., Gouiffes, C., Tarengi, M., & Wang, L.-F. 1990, *IAU Circ.*, 4943, 1
 Wampler, E. J., Wang, L., Baade, D., Banse, K., D'Odorico, S., Gouiffes, C., & Tarengi, M. 1990, *ApJ*, 362, L13
 Wang, L., Dyson, J. E., & Kahn, F. D. 1993, *MNRAS*, 261, 391
 Wang, L., Mazzali, P.A. 1992, *Nature*, 355, 58
 Wang, L. & Wampler, E. J. 1992, *A&A*, 262, L9
 Weingartner, J. C. & Draine, B. T. 2001, *ApJ*, 548, 296 (WD01)
 Woosley, S.E. 1988, *ApJ*, 330, 218
 Woosley, S. E., Pinto, P. A., Martin, P. G., Weaver, T. A. 1987, *ApJ*, 318, 664
 Woosley, S. E., Pinto, P. A., Weaver, T. A. 1988, *Pub. ASAu*, 7, 355
 Xu, J., Crotts, A. P. S. & Kunkel, W. E. 1994, *ApJ*, 435, 274
 Xu, J., Crotts, A. P. S. & Kunkel, W. E. 1995, *ApJ*, 451, 806 (Erratum: 463, 391)
 Xu, J. & Crotts, A.P.S. 1999, *ApJ*, 511, 262
 Zacharias, N., Urban, S. E., Zacharias, M. I., Wycoff, G. L., Hall, D. M., Monet, D. G., & Rafferty, T. J. 2004, *AJ*, 127, 3043
 Zacharias, N., et al. 2000, *AJ*, 120, 2131